Planar hybrid plasmonic-photonic resonators: an interferometric investigation

Ph.D. Thesis, University of Amsterdam, November 2020
Planar hybrid plasmonic-photonic resonators:
an interferometric investigation
Annemarie Berkhout

ISBN: 978-94-92323-40-8

The work described in this thesis was performed at
AMOLF, Science Park 104, 1098 XG Amsterdam, The Netherlands.

This work is part of the Netherlands Organisation for Scientific Research (NWO).

A digital version of this thesis can be downloaded from
http://www.amolf.nl

Planar hybrid plasmonic-photonic resonators: an interferometric investigation

ACADEMISCH PROEFSCHRIFT

ter verkrijging van de graad van doctor
aan de Universiteit van Amsterdam
op gezag van de Rector Magnificus
prof. dr. ir. K.I.J. Maex
ten overstaan van een door het College voor Promoties ingestelde commissie,
in het openbaar te verdedigen in de Agnietenkapel
op vrijdag 13 november 2020, te 10:00 uur

door

Annemarie Berkhout

geboren te Amsterdam

Promotiecommissie

Promotor:	prof. dr. A. F. Koenderink	Universiteit van Amsterdam
Copromotor:	dr. S. R. K. Rodriguez	Universiteit van Amsterdam
Overige leden:	prof. dr. S. Linden	Universität Bonn
	prof. dr. J. Gómez Rivas	Technische Universiteit Eindhoven
	dr. J. van de Groep	Universiteit van Amsterdam
	prof. dr. H. B. van Linden van den Heuvell	Universiteit van Amsterdam
	prof. dr. H. J. Bakker	Universiteit van Amsterdam

Faculteit der Natuurwetenschappen, Wiskunde en Informatica.

Contents

1

Introduction

1.1 Light and the nanoscale

Light is at the heart of all life. We perceive the world through the touch of sunlight on our skin. After scattering by objects in our surrounding light enters our eyes and adds a mesmerizing spectrum of colors to our perception. Using optical microscopes we can image the geometry and dynamics of the smallest building blocks of life [1]. In our communication, signalling by light has evolved from the rudiments of navigation and messaging at sea, to current optical transfer of web traffic at hundreds of terabits per second bandwidth across transatlantic fiber optic cable technology [2]. We also use light to fulfil our needs more directly, for example to grow vegetables by photosynthesis, to print without ink [3], to harvest energy using solar panels [4], to laser cut, to tan, to perform medical diagnostics [5] and potentially even for cancer therapy [6].

Beyond the numerous applications that one can encounter in daily life, light is scientifically especially fascinating at length scales matching optical wavelengths. This is due to the fact that light is a wave phenomenon, and therefore interference, resonances and confinement can occur for light analogous to the macroscale resonances for sound and motion in e.g., vibrating pianostrings and oscillating playground swings. Since light is an electromagnetic oscillation with a wavelength on the order of just 500 nm (visible, blue), which is orders of magnitude smaller than the typical wavelengths of sound, resonators for light can be scaled down to micrometer or nanometer dimensions to confine light on this length scale. Indeed geometries on such ultrasmall length scales have been demonstrated, in which confined light

bounces back and forth millions or even up to billions of round trips before leaking out [7].

Confining light in a very small volume for a very long duration around a controlled point in space and time is deemed scientifically very important since it permits to greatly enhance the probability that an atom or a molecule absorbs or emits a photon, in other words to enhance light-matter interaction [8, 9]. This interaction is intrinsically weak in the sense that the (room-temperature) extinction cross section of atoms and molecules is generally much smaller than the diffraction limited spot that light can be focused to [10, 11], typically by a factor 10^5. Increasing the interaction probability to unity, is essential for cavity quantum electrodynamics [12, 13] and quantum information technologies [14, 15], as well as applications in single photon detectors [16, 17], nano lasers [18], solar cells [4, 19, 20], and sensing and spectroscopy of single nano-objects [21–23]. In addition, a holy grail in information processing is that optical non-linearities can be used to switch light-by-light at very low powers [24, 25]. This would obviate the current separation between information transport with light, yet processing with electronics. Since this thesis deals with nanoscale structures that leverage distinct resonance mechanisms for light, in this introduction we briefly treat a few nanophotonic principles for light trapping. This introduction closes by phrasing central questions that motivate this thesis, and an outline of the subsequent scientific contributions included as chapters in this thesis.

1.2 Microresonators

Similar to sound waves trapped between walls, light can resonantly circulate in optical cavities. The textbook example [26] of this is that of a 1D Fabry-Pérot resonator. Figure 1.1a illustrates the basic principle of an optical cavity. Two partially reflective surfaces allow light to couple into the cavity, following which the light oscillates back and forth until it is absorbed or leaks out. In a hypothetical perfect 1D cavity, i.e., with perfect reflectors, light would be trapped indefinitely for resonant frequencies that occur at precisely defined values corresponding to a halfinteger number of optical wavelengths fitting in between the mirrors. In reality, mirrors are lossy either due to partial transmission or optical absorption. This causes a broadening of the resonances, which are now quantified by a dimensionless number known as quality factor Q. The quality factor is the number of oscillations before energy in the cavity has decayed to a factor 1/e of its initial value, or alternatively can be read off as the full width half maximum of the reflection and transmission resonances observable in the far field, well outside the cavity. These features are evident in the well known etalon formula for the total reflected field as a function of mirror spacing d and incoming wavevector k, incorporating multiple reflec-

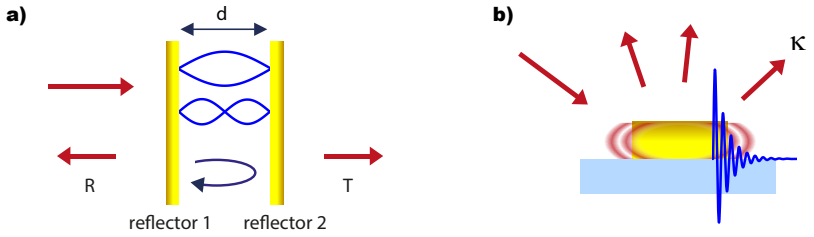

Figure 1.1: Example cavities for light trapping. a) Optical cavity: two reflectors spaced at a distance d support resonances at wavelengths λ for which $d = n\lambda/2$ with n an integer number. The linewidth of a resonance at fixed size is a measure for the quality factor of the resonator, and can reach values up to 10^8. b) Plasmonic cavity: sketch of a metal nanoparticle on a substrate. Light is concentrated in so-called local surface plasmon resonances, collective oscillations of conduction electrons at metal-insulator interfaces. Such plasmonic resonances are ordinarily short lived, i.e. on the order of fs, corresponding to quality factors of order 10-50. Mode volume are significantly smaller than in optical cavities.

tions inside the cavity, as [27]

$$R = \frac{r_1 + r_2(1 + 2r_1)e^{2inkd}}{1 - r_1 r_2 e^{2inkd}} \tag{1.1}$$

in which r_1 and r_2 are the amplitude reflectivity of reflector 1 and reflector 2 respectively (see Fig. 1.1a), and n is the refractive index of the medium inside the resonator. Etalons have many applications in optics and spectroscopy, particularly as filters and for precision spectroscopy [28].

Alongside the quality factor Q, a second important parameter in the context of optical light trapping is the mode volume V, with dimensions of physical volume $[\mathrm{m}^3]$. There are several reasons for which tight confinement of light is desirable. First, if the goal is to ensure enhanced interaction between matter, i.e., an atom or a molecule, it is desirable to confine light as close to the matter as possible (small V) for as many optical cycles as possible (large Q). This notion is the essence of the celebrated Purcell effect [29]. According to the Purcell effect, the coupling of an emitter to a confined light field can be gauged by the acceleration of its spontaneous emission rate, which is proportional to Q/V. A large Q/V means that the particle's decay rate is increased, and conversely also absorption of an incident photon becomes more likely. A second reason to design microcavities with 3D confinement of light, is that it benefits integration of many cavities with other optical components and routing on tiny chips, in the context of information processing with light [30].

Etalons do not provide the ultimate in light confinement, owing to their planar geometry that has no transverse confinement. Indeed, without transverse confinement, no V can be defined for them. However, in more elaborate designs, V can be reduced down to $(\lambda/2n)^3$ with λ/n the wavelength in the

medium of refractive index n that comprises the resonator [8]. While the Fabry-Pérot cavity, but with mirrors of micrometer radius of curvature, still plays an eminent role [31, 32] in the field of 3D optical microcavities, there is a large variety of other designs that realize the tightest confinement. Generally, these are optical cavities that avoid metallic mirrors to avoid losses, and instead confine light in a high refractive index medium, surrounded by lower index media [33]. A main family of examples comprises the optical microsphere, microdisk, and microtoroid [8, 34, 35], in which light is contained by total internal reflection, similar to the guiding of light in glass fiber. Other prominent examples are micropillars [36, 37], nanobeam cavities [38, 39], and photonic crystals [40] that use Bragg diffraction in 1D, 2D or 3D periodic dielectric structures [41]. Particularly photonic crystal cavities and nanobeam designs reach the ultimate limit in light confinement with dielectric systems, i.e. $(\lambda/2n)^3$.

1.3 Plasmonics

A very different approach for light confinement is based in the field of plasmonics, and has been pursued actively since circa 2000 [42]. The electromagnetic properties of metals are dominated by their conduction electrons in the metal [43]. At a metal-insulator boundary, light can strongly interact with the conduction electrons in the metal, forming a surface wave that is in part 'electron-like', i.e., a charge density wave travelling over the surface, and in part 'light-like', with energy stored in the electromagnetic field. These waves are known as surface plasmon polaritons [42]. In metal nanoparticles of subwavelength dimensions, these oscillations are confined to form localized surface plasmon resonances, that spectrally depend on nanoparticle size, shape and material composition [44, 45].

A qualitative picture to understand localized surface plasmon resonances is shown in Figure 1.1b. Upon incoming excitation (with continuous fields or pulsed laser field), a localized surface plasmon resonance is excited by the force that the electric field of the incident wave exerts on the conduction electrons. This force causes them to spatially displace relative to the particle ionic backbone. As the electrons are pulled back by the positively charged ionic backbone, they are subject to a linear restoring force. This results in a resonant behavior, with resonance frequency generally lying in the UV, visible or near infrared depending on the particle shape, and metal used [44]. Subsequently, the electron oscillation loses energy by Ohmic dissipation, and by radiative decay (rate denoted by κ). Radiation damping occurs since the induced charge separation is tantamount to an oscillating dipole moment, and is visible as very strong far field scattering. The dipole moment and local field present at the particle oscillates, and rings down as a function of time as schematically represented in blue. The sum of the Ohmic and radiative decay

rate determines the total decay rate of the plasmon, i.e., the characteristic plasmon life time (inverse rate).

Depending on the precise geometry Ag and Au nanoparticles are reported to create field enhancements with values up to 10^3 [46, 47], and mode volumes reportedly as small as $\lambda^3/10^3$ [48] and smaller [49, 50]. The field of localized surface plasmons is very lively in the context of single molecule spectroscopy and sensing [23, 51], due to the strength of electromagnetic enhancement, the ease of fabricating structures [52, 53], and the possibility of chemical functionalization. Single crystal metal nanoparticles can be synthesized colloidally by seeded growth in a solution of metal ions [54]. Conversely, complex arrays of particles can be fabricated lithographically by the evaporation of metal in predefined nanoscale patterns [55]. For the integration in photonic platforms lithography is the most straightforward practice. While the quoted exceptionally tight confinement offered by plasmonics is advantageous for large Purcell factors, a downside is the poor Q. Ohmic damping alone in Ag and Au limit the Q of conduction electron oscillations to about Q = 40. For far-field addressing of plasmonic structures, it is preferable that radiative damping dominates over Ohmic damping, leading to even lower Q's down to Q = 5. In this sense, plasmonic particles complement the merit of optical cavities, offering low Q and very tight confinement, instead of vice versa.

1.3.1 A simple model for the response of metal nanoparticles

Since this thesis concerns the interaction between plasmonic nanoparticles and light it is instructive to briefly review the principles of the response of

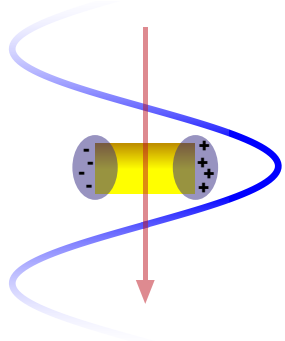

Figure 1.2: Schematic of a metal nanoparticle response to an incoming light field. The oscillating electric field (propagation direction indicated with the red arrow, electric field amplitude indicated in blue) interacts with the particle, causing charge density oscillations of the conduction electrons in the metal (so-called localized surface plasmon polaritons) which form an effective dipole moment. This dipole is in turn a source of radiation. Note that in reality the scatterer size generally is much smaller than the optical wavelength.

metal nanoparticles to electric fields, and to introduce concomitant observables (Figure 1.2). If one makes the assumption of a deeply subwavelength scatterer, the dipole approximation holds [56, 57]. In this approximation the response of the scatterer to incident light is an induced dipole moment $\mathbf{p}$ determined by the amplitude of the incoming field $\mathbf{E}$ and the polarizability α via

$$\mathbf{p} = \alpha \mathbf{E}. \tag{1.2}$$

The polarizability α is a property of the scatterer, set by its material, size, and shape [58]. For the polarizability of a small spherical scatterer a seminal result is due to Lord Rayleigh [57, 59], given in SI units by

$$\alpha = 4\pi\epsilon_0 V \frac{\epsilon(\omega) - 1}{\epsilon(\omega) + 2} \tag{1.3}$$

with $V = r^3$ proportional to the volume of the spherical particle (r the radius, note the factor $4\pi/3$ difference) and $\epsilon(\omega)$ the frequency dependent permittivity. This result is in actual fact the *electrostatic* response of a sphere to a homogeneous field and in the limit $c \to \infty$. Inserting the frequency dependent permittivity but without revising the polarizability to include 'electrodynamic corrections' (terms containing c) is known as the quasistatic limit. The frequency dependent dielectric function of free electrons in a metal can to first approximation be expressed using a Drude model as [43]

$$\epsilon_{\mathrm{Drude}}(\omega) = 1 - \frac{\omega_\mathrm{p}^2}{\omega^2 + i\omega\gamma} \tag{1.4}$$

with ω_p the plasma frequency, a material constant that depends on electron density and effective mass, and with γ the Ohmic damping rate. Inserting this result in Eq. (1.3) results in a polarizability of a spherical metal nanoparticle

$$\alpha_0 = 4\pi\epsilon_0 V \frac{\omega_0^2}{\omega_0^2 - \omega^2 - i\omega\gamma}. \tag{1.5}$$

This result is also known as Fröhlich's model for a metallic sphere [59], and has exactly the form of a Lorentzian resonator with resonance frequency $\omega_0 = \omega_p/\sqrt{3}$, and loss set by the bulk Ohmic damping rate. For other particle shapes, similar electrostatic calculations can be (numerically) performed, generally resulting in different, shape-dependent resonance frequencies. While actual plasmonic particles do not provide exactly Lorentzian resonances, for instance due to the non-Drude response of real metals and higher order multipole resonances, the Fröhlich model is nonetheless a useful picture for qualitative understanding. We note that its physics is exactly equivalent to the Lorentz oscillator model for the classical description of the optical response of a single atom, where an external electric driving force $E = E_0 e^{-i\omega t}$ of

magnitude E_0 drives the electron (charge q, mass m) displacement x according to the equation of motion [56]

$$\frac{\mathrm{d}^2x}{\mathrm{d}t^2}(t) + \gamma\frac{\mathrm{d}x}{\mathrm{d}t}(t) + \omega_0^2 x(t) = \frac{q}{m}E_0 e^{-i\omega t}. \tag{1.6}$$

Indeed, the qualitative picture is similar, with the distinction that in a plasmon particle the electric field pulls on a collection of of order 10^4 conduction electrons, effectively causing charge separation across the particle, depicted as blue clouds in Figure 1.2. A physical interpretation of the strength of scattering is attached to the *polarizability volume* $\alpha_0' = \alpha_0/(4\pi\epsilon_0)$. For plasmonic particles on resonance, the polarizability volume can far exceed the physical particle volume.

1.3.2 Radiation damping

Accellerating charges are a source of optical radiation. Therefore, the driven conduction electron cloud oscillating around the particle ionic backbone must be equivalent to a strong source of far field radiation, producing dipole radiation according to Larmor's formula. In the far field this is visible as scattered light, and as a damping rate *in addition* to the Ohmic damping rate γ. Radiation damping is not consistently contained in Rayleigh's polarizability (Eq. (1.5)). This is a consequence of the the quasistatic approximation. The fact that radiation damping is not accounted for, furthermore means that Rayleigh's model for polarizability leads to a scatterer that violates energy conservation, i.e., the optical theorem for scattering. The optical theorem states that the total power that an induced dipole takes out of an incident beam, known as extinction, must equal the sum of the power that it absorbs, and the power that it scatters. Expressed in cross sections for extinction, scattering and absorption

$$\sigma_{\mathrm{scatt}} \leq \sigma_{\mathrm{scatt}} + \sigma_{\mathrm{abs}} = \sigma_{\mathrm{ext}}. \tag{1.7}$$

The scattering cross section [units of area m^2] is the ratio of the total radiated power [W] of the dipole divided by the intensity of the incident field [$\mathrm{W/m}^2$], and is given through Larmor's formula by [56]

$$\sigma_{\mathrm{scatt}} = \frac{k^4}{6\pi\epsilon_0^2}|\alpha(\omega)|^2 \tag{1.8}$$

with k the wave vector in the surrounding medium. The extinction cross section can be calculated from the work that the field E needs to do to drive the induced dipole moment p, again normalized to incident intensity, and reads [56]

$$\sigma_{\mathrm{ext}} = \frac{k}{\epsilon_0}\mathrm{Im}(\alpha(\omega)). \tag{1.9}$$

From Eq. (1.8,1.9) and the fact that α_0 depends on volume, one derives the commonly quoted conclusion that the scattering cross section and extinction cross section scale differently with the scatterer size, as r^6 and r^3 respectively. In other words, while bigger particles are more efficient scatterers, in the smaller ones the losses are dominated by absorption. Generally, for plasmonic particles the cross sections for extinction exceed the geometrical cross sectional area by a factor up to 10 (signifying strong scattering), with scattering exceeding absorption for particle radii above 20 nm. As a note on nomenclature, we briefly remark on the terminology used throughout this thesis regarding 'nano-antennas'. In literature, plasmonic nanoparticles are often indicated as 'nano-antennas', with various definitions for the word 'nano-antenna' being used. For instance, a common use of the term 'nano-antenna' is to indicate the intent to transduce from near-field (e.g., fluorophores at an antenna) to far-field [60]. An alternative use is to indicate very strong, resonant scatterering, with cross sections and polarizabilities far exceeding particle area, resp. volume. In this work we apply the term 'nano-antenna' interchangeably with the term 'plasmonic nanoparticle' if we indicate metallic subwavelength scatterers to emphasize that we focus on particles with extinction cross section far exceeding geometrical areas, and approaching $\lambda^2/2$.

It is evident that the optical theorem Eq. (1.7) is not satisfied by Rayleigh's expression for polarizability, as it is tantamount to a constraint on α

$$\frac{k}{\epsilon_0}\mathrm{Im}(\alpha(\omega)) > \frac{k^4}{6\pi\epsilon_0^2}|\alpha(\omega)|^2.$$

that is not generally satisfied (e.g., assume a lossless particle). To be consistent with the optical theorem, the electrostatic polarizability can be amended with a correction term according to

$$\alpha'_{\mathrm{dyn}} = \frac{1}{1/\alpha'_0(\omega) - i\frac{2k^3}{3}}, \tag{1.10}$$

written in terms of polarizability volumes $\alpha' = \alpha/(4\pi\epsilon_0)$. This directly brings out that the polarizability volume is due to radiation damping intrinsically limited to $\frac{3}{2}\left(\frac{\lambda}{2\pi}\right)^3$, i.e. (a fraction of) the free-space wavelength cubed, entirely independent of the actual scatterer volume.

This amendment is often called 'addition of radiation damping', as in the Fröhlich model of Eq. (1.5), the amendment is equivalent to introducing a higher damping rate. This damping is due to radiative damping, and appears in the equation of motion Eq. (1.6) by proper inclusion of the Abraham-Lorentz radiation reaction force. The polarizability α_{dyn} is known as 'dynamic' polarizability in scattering literature [59, 61].

1.3.3 Dipole-dipole interactions and periodic plasmon nanoparticle arrays

When multiple nanoparticles are placed in close vicinity they can interact with one another via both near-field and far-field effects. Near-field effects occur when the particle separation is less than the wavelength of light ($1/r^3$ dipolar near field), while far fields have a $1/r$ range. As this thesis deals with plasmon nanoparticles in periodic arrays, we introduce briefly the physics of interacting dipoles in a lattice with a pitch smaller than the wavelength of the incident light.

We suppose a lattice of identical antennas located at a periodic lattice of positions labelled $\mathbf{R}_n$ (2D lattices in this work). Upon irradiation with a plane wave incident at parallel momentum $\mathbf{k}_{||}$, the induced dipole moment in particle n of the lattice will read

$$\mathbf{p}_n = \alpha_{\text{dyn}}[\mathbf{E}(\mathbf{R}_n) + \sum_{n \neq n'} \mathbf{G}(\mathbf{R}_n - \mathbf{R}_{n'})\mathbf{p}_{n'}]. \tag{1.11}$$

Here $\mathbf{E}(\mathbf{R}_n) = \mathbf{E}_0 e^{i\mathbf{k}_{||}\cdot\mathbf{R}_n}$ is the incident driving field at particle n. The dipole moment induced in particle n is now given by the sum of two contributions: that directly induced by the driving field, plus corrections due to the scattered fields (near-field and far-field) exerted by all the other dipoles in the lattice. These fields are expressed through the terms $\mathbf{G}(\mathbf{R}_n - \mathbf{R}_{n'})\mathbf{p}_{n'}$, where $\mathbf{G}$ is a so-called Green tensor, expressing the free-space electric field at location $\mathbf{R}_n$ due to a dipole at $\mathbf{R}_{n'}$.

By virtue of Bloch's theorem for periodic systems, the electric dipole moment induced in particle n at position $\mathbf{R}_n$ is simply related to that in the particle at the origin as $\mathbf{p}_n = \mathbf{p}_0 e^{i\mathbf{k}_{||}\cdot\mathbf{R}_n}$, whereby

$$\mathbf{p}_0 = \alpha_{\text{dyn}}[\mathbf{E}_0 + \sum_{n \neq 0} \mathbf{G}(\mathbf{R}_n - \mathbf{R}_0) e^{i\mathbf{k}_{||}\cdot(\mathbf{R}_n - \mathbf{R}_0)}\mathbf{p}_0]. \tag{1.12}$$

This means that the dipole moment induced in the lattice can itself be expressed through a polarizability

$$\mathbf{p}_0 = \alpha_{\text{latt}}\mathbf{E}_0 \quad \text{with} \quad \alpha'_{\text{latt}} = \frac{1}{1/\alpha'_{\text{dyn}} - \mathcal{G}_{\mathbf{k}_{||}}} \tag{1.13}$$

(last expression again using polarizability volumes). The *effective* dipole polarizability α_{latt} of a particle in a lattice takes into account the contributions of all the other scatterers in the lattice through the so-called 'lattice sum' $\mathcal{G}_{\mathbf{k}_{||}}$. Techniques to calculate the lattice sum are outside the scope of this thesis, and borrow so-called Ewald summation techniques from solid-state physics [62–64]. For a detailed review, we refer the reader to Ref. [61].

In the field of plasmonics two distinct limits are relevant. First, dense periodic arrays of plasmonic nanoscatterers are of interest, with periodicities

so small that no grating diffraction occurs. A remarkable result is that for such dense, 2D, lattices, and under normal incidence, it generally holds that [61]

$$\mathrm{Im}\mathcal{G}_{\mathbf{k}_{||}=0} = 2\pi k/\mathcal{A} - 2k^3/3,$$

with $\mathcal{A}$ the unit cell area. This leads to the very peculiar result that when placed in a lattice, metal nanoparticles are subject to a radiation damping that is very different from their isolated radiation damping. The free-space radiation damping term $2k^3/3$ is completely cancelled, and replaced by a lattice specific radiation damping, that increases markedly with scatterer density. This signifies collective, i.e., superradiant damping [65] and implies that the extinction cross section per nanoparticle in a lattice is bounded to remain smaller than the unit cell area. The second limit in which Eq. (1.13) is relevant is in diffractive systems, when periodicities are large. The lattice sum $\mathcal{G}_{\mathbf{k}_{||}}$ tends to have very sharp variations at specific incidence angles (values of $\mathbf{k}_{||}$), corresponding to geometric conditions for the appearance of grating diffraction orders. The sharp variations can cause cancellations in the denominator of Eq. (1.13), which give rise to very sharp resonances in optical response [66]. These are known as 'surface lattice resonances' [67–69]. Surface lattice resonances have been widely used, e.g. for biosensing [70], nanolasing [71, 72] and strong coupling to excitons [73].

In this work we will mostly use periodic arrays of plasmon nanoparticles that are so dense that the lattices are not diffractive. In descriptions where we consider these arrays as effectively a homogeneous thin sheet with a peculiar effective reflection/transmission constant, we sometimes refer to these arrays as metasurfaces. This assignment uses 'meta' in the original spirit of 'metamaterials', which are nanostructured bulk materials built to have assigned effective optical constants as if they were homogeneous in an effective medium approach. The term 'metasurface' as opposed to 'nanoparticle array' emphasizes the 'homogenized' nature of the description that we will use. This use of the term metasurface indicates a very limited scope compared to the breadth of structures pursued in the metasurface community [74]. The field of metasurfaces strives to perform complex wavefront transformations by transmitting or reflecting incident light off of surfaces that are densely populated with individually tuned nano-antennas, mimicking locally varying effective reflection and transmission constants [75–77]. Some of the structures that we propose in chapters 2, 3, and 4 of this thesis could be used as 'pixels' in such spatially varying metasurfaces.

1.4 High Q plasmonic systems and hybrid resonators

As outlined above, microcavities and plasmonic systems have complementary merits. Microcavities provide very high quality factors, and thereby spectrally

narrow features, but suffer from comparatively poor confinement with intrinsic limitation by interference to $(\lambda/2)^3$. Conversely, plasmonic systems excel at spatial confinement, but intrinsically provide almost no control over Q. It would be highly interesting to retain the benefits of large field enhancements offered by plasmonics, but without the penalty of broad linewidth of plasmonic scatterers. Hybrid plasmonic-photonic resonators are highly promising candidates in the strive for large emission enhancement and the control over emission bandwidth [78, 79]. In addition, the tunable coupling between photonic and plasmonic modes provides handles to adjust Q which is essential for linewidth matching to integrate multiple hybrids into one device. For instance, applications in quantum optics generally require *independent* control over Purcell factor and Q, as is the case for lineshift-based sensing, SERS substrates, and many other examples of envisioned applications.

The pursuit of 'high(er)-Q' plasmonics has a long history, with two main and complementary approaches. A first route has been to use surface lattice resonances (SLRs) [66–69, 80]. Surface lattice resonances use the divergent response noted at grating conditions in Eq. (1.13), which in practice leads to resonances with Q's up to 300 [81]. The physics of the underlying resonance is that it is no longer confined to individual nano-antennas, but that instead a large fraction of the field is delocalized above and below the antennas. Due to the delocalization away from the absorbing metal, the resultant SLRs are longer lived than the bare particle plasmons scatterers [80]. Applications of SLRs include biosensing techniques [70], enhancement of spontaneous emission by layers of already efficient fluorophores in solid-state lighting [82–84], and plasmonic distributed feedback lasing [71, 72]. Surface lattice resonances can be strongly coupled to molecular excitons, as demonstrated by Rodriguez et al. using fluorescent rhodamine 6G [73]. Aside from SLRs, diffractive coupling can also be arranged with planar waveguides, leading to waveguide-plasmon polaritons, with merits for applications in very similar domains [83–85].

A second route to high Q plasmonics is the hybridization of plasmonic and microcavity resonators. Hybrid plasmonic-photonic resonators have recently emerged as promising candidates in the quest for systems that allow to increase and tailor Purcell factors, a property that surface lattice resonant systems do not excel in due to the delocalization of the electromagnetic field. Since 2015 several groups have pursued hybrids of single antennas, 3D confined microcavities, and their interaction with single emitters. Doeleman et al. have demonstrated that the combination of a cavity and a dipolar antenna can be used to achieve stronger emission enhancement in an emitter placed in the right position (i.e. at high field enhancement), compared to the bare constituents [78]. Such system would additionally allow to tune the emission bandwidth. Experimental demonstrations of dielectric-plasmonic resonators that confine in three dimensions include photonic crystal geometries [86], silicon nitride microdisks coupled to metal antennas [87], microtoroids [88], and

whispering-gallery mode (WGM) microsphere cavities that are tunably coupled to metallic nanorods [89–91]. The same WGM cavities are even used to perform spectroscopy on single particles [92]. Other work towards very high Purcell factors and even strong coupling includes the theoretical work of Gurlek et al. [93], studying a quantum emitter coupled to a cone-shaped plasmon antenna inside a curved-mirror Fabry-Pérot cavity.

Plasmonic-photonic coupling in planar structures in which the cavity mode is confined in only one dimension has been studied in a set of important works by Ameling et al. [94–97]. Central in this work is a design of two reflective surfaces with a plasmonic particle array in the center. Their work showed a mode splitting in the parameter space spanned by frequency and cavity thickness, at points where the bare cavity resonances and the plasmonic resonance would have intersected. This signature of strong coupling between the plasmonic and photonics modes was explored for refractive index sensing purposes. Since 2013 this line of research saw no further activity, until Bisht et al. [98] explored the possibility of strong coupling between light in such planar plasmonic-photonic etalons and excitons in two-dimensional transition metal dichalcogenide (TMDC) flakes. Very recently the same group demonstrated ultrastrong coupling between plasmons and cavity photons at room temperature [99, 100])

In this thesis we consider hybrids of plasmonic and photonic resonators, as part of an effort to understand the merits of high-Q plasmonic structures. In particular, this thesis is an endeavor to develop the basic experimental techniques and theoretical tools relevant to understanding the near-field and far-field response in simple 'etalon-like' hybrid resonators, combining plasmon array resonances and etalon resonances.

1.5 Outline of this thesis

In this thesis we systematically study the response of high-Q plasmonic systems that are extended and planar, yet non-diffractive, as distinct from the large body of work in plasmonics on SLRs on one hand, and the emerging efforts on single-antenna plasmonic photonic hybrids on the other hand. Planar cavities are a very simple model system in which to fully analyze input-output relations, i.e., the complex-valued reflection and transmission coefficients, as well as to address local properties inside the system, i.e. near-field enhancement and plasmonic absorption. Planar cavities are experimentally easy to fabricate and interrogate, and planar plasmonic-photonic resonators can be easily combined with, e.g., 2D TMDC materials and other excitonic species to form multilayer systems which can show ensemble strong coupling. The work thus deepens the insight in earlier results by Ameling and Bisht, and serves as a stepping stone to understand the optical response of 'localized' hybrids single-antenna plasmonic-photonic hybrids, but without

the difficulty of fabrication and optical interrogation involved in combining microdisks, nanobeams, or photonic crystals, with single antennas.

Figure 1.3 illustrates the main geometries and questions addressed in this thesis. Generally, the geometries fall in the class of 'multilayer' structures in which layers of dielectrics, metals, and non-diffractive 2D plasmon arrays can occur in various orderings. This class of systems for instance encompasses etalons in which one reflector is a metasurface, microcavities inside which a metasurface is placed, and metasurface etalons that furthermore contain excitonic material for strong coupling (indicated in purple). As for any photonic system, central questions to ask are what the optical properties of such hybrid multilayer systems are, in terms of far-field (reflection, transmission, absorption) and near-field. This thesis deals with both theoretical and experimental aspects of this question. It first presents a simple theoretical framework to describe such systems that allows to predict far field observables of hybrids from the properties of the separate constituent layers. Next, we present interferometric and polarimetric schemes for testing the far field properties. Finally we explore pulsed excitation and localized nonlinear response at the plasmon layer as a means to access near-field properties. In more detail, this thesis contains the following chapters:

- **Chapter 2** presents a simple modelling approach for such arbitrary stacks interspersing traditional optical multilayers and resonant 2D nondiffracting plasmonic arrays (Figure 1.3a). We implement the reflection and transmission coefficients of metal and dielectric layers through a simple transfer matrix model, while for scattering arrays we construct transfer matrices from their reflection and transmission

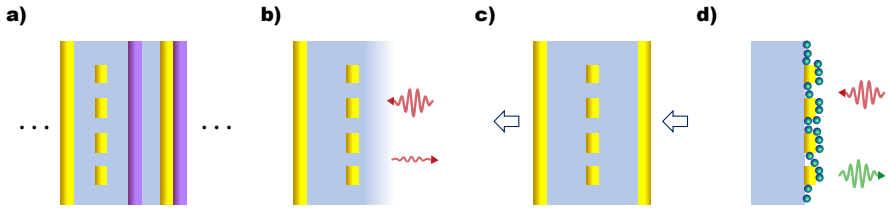

Figure 1.3: Illustrations of the planar plasmonic-photonic hybrids studied in this thesis. a) Arbitrary stack (infinitely extending in two dimensions) of plasmonic scatterer sheets and metal and dielectric layers. Chapter 2 presents a model for input-output relations. b) Plasmonic scatterer array facing a metal mirror, separated by a variable thickness of SiO_x. In chapter 3 we present amplitude and phase resolved reflection results. c) Metal scatterer layers sandwiched, separated by SiO_x, between two gold mirrors. Chapter 4 demonstrates the strong coupling signatures in transmission, accompanied by strong polarization conversion effects. d) Sketch of gold nanorod arrays on glass, covered in quantum dots. Chapter 5 explores the nonlinear two-photon excited luminescence signal interferometrically, paving the way towards probing the local field dynamics.

constants in isolation. We apply this model to three cases. First, we study the phase and amplitude response of etalons in which one reflector is a regular mirror and one mirror is a plasmonic metasurface. While this problem revisits perfect absorption in plasmonic Salisbury screens, we shed new light on the phase response. As a second problem we provide a new understanding on strong coupling in the system proposed by Ameling et al. [96] of plasmonic arrays inside a traditional etalon. Thirdly we consider the potential hybridization between plasmonics, photonics and excitons.

- **Chapter 3** demonstrates experimentally the reponse of Fabry-Pérot cavities in which one of the metal mirrors is patterned to form an array of plasmonic nanorods of various pitch (Figure 1.3b), and the other reflector is a regular mirror, which is the first scenario theoretically treated in chapter 2. We present a common path linear interferometry setup based on pulsed excitation. It combines the sample in the Mach-Zehnder arm to obtain sample and references pulses, with a Michelson interferometer in the detection arm, which collects the cross correlation between reference and sample signals as a function of delay. The resulting amplitude and phase maps of the reflection as function of etalon spacing d and frequency ω show that points of perfect absorption surprisingly always come in pairs, and are accompanied by phase singularities. We explain the topological origin of these hitherto unobserved properties of Salisbury screens.

- **Chapter 4** presents experiments on the strong coupling between plasmon particle array resonances and etalon resonances in the geometry first proposed by Ameling et al. [96]. We have realized structures with excellent control over cavity width and array scattering strength, allowing for a very precise mapping of hybridization in white light transmission. Since Ameling et al. [96] already numerically predicted strong coupling it is no surprise that in transmission the empty-cavity modes anti cross with the nanoparticle resonance frequency, which we for the first time map experimentally as a function of frequency, cavity width and array scattering strength. However, our data provide new insight in the *magnitude* of the anticrossing. Moreover we show that strong coupling in such systems can be leveraged for very strong polarization conversion effects.

- **Chapter 5** presents an exploration into new methods to study the near-field in (high-Q) plasmonic systems, using ultrafast nonlinear effects. Far-field observables, like reflection and transmission studied in chapters 2, 3 and 4 do not report on the strength, or dynamics of the near field. One method to obtain near-field information is to use a local nonlinearity as a probe of local field. Chapter 5 presents the design, realization

and calibration of a common path interferometric autocorrelation (IAC) microscope setup that we have implemented, in order to lay the foundations for a study on the local time dynamics of high-Q plasmonics. We demonstrate, through IAC measurements, the characterization of our laser pulses in the focal plane, and we present preliminary results on the two-photon excited luminescence response of quantum dots in the near fields of plasmonic Ag nanorod arrays (Figure 1.3d). This experimental technique could extend the rich field of nonlinear plasmonics [101–111].

2

A simple transfer-matrix model for metasurface multilayer systems

In this chapter we present a simple transfer-matrix based modelling tool for arbitrarily layered stacks of resonant plasmonic metasurfaces interspersed with dielectric and metallic multilayers. We present the application of this model by analyzing three seminal problems in nanophotonics. These are the scenario of perfect absorption in plasmonic Salisbury screens, strong coupling of microcavity resonances with the resonance of plasmon nano-antenna metasurfaces, and the hybridization of cavities, excitons and metasurface resonances.

2.1 Introduction

Since almost a decade metasurfaces have emerged as a very fast growing field of research in nanophotonics [112–114]. In contrast to the notion of metamaterials that were designed to realize 3D bulk materials with peculiar designer permittivity and permeability, the notion of metasurfaces is that they shape waves by scattering off of an abrupt designer boundary condition with a completely controlled and locally varying amplitude and phase. This boundary condition is realized by engineering subdiffractive arrays of building blocks that are arrayed in a 2D sheet. This notion revitalized a venerable history in grating science, particularly the notion of echelette gratings to shape diffraction [115]. Recent demonstrations of metasurfaces include a large variety of flat optics components, such as lenses [77, 116–118], waveplates and polarization optics [119–121], as well as holograms [119–121], diffusers [122], and even computational metasurfaces that are designed to perform simple linear mathematical operations on incident wavefronts [123–125]. In this thesis we focus on 2D arrays where the constituents are strong, resonant scatterers with a dipolar plasmonic resonance, as opposed to dielectric metasurfaces [114, 126].

Understanding the physics of layered systems in which metasurfaces are stacked in succession, or interspersed with normal metal and dielectric layers, is of large relevance from several viewpoints. First, if one considers metasurfaces as objects that transform incident wavefronts according to designed mathematical functions in the context of signal processing and computation [123–125], an important question is how you can concatenate

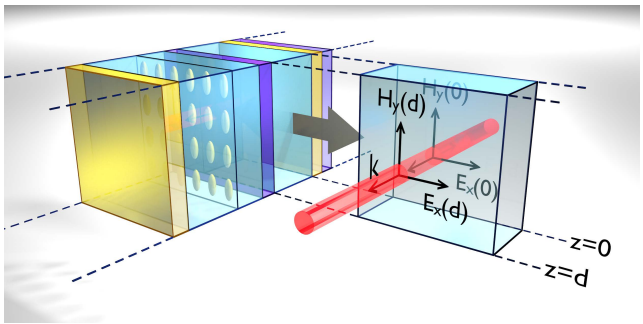

Figure 2.1: Schematic of an arbitrary 1D stack of materials, infinitely extending in x and y, including nonresonant metal and dielectric layers as well as resonant metasurfaces. Stack properties may be specified either by refractive index n and thickness d for normal material layers, or by metasurface reflection and transmission coefficients r and t. The highlighted slab shows right at its interfaces the electric and magnetic field orientations and k-vectors of an incoming and outgoing wave (beam path indicated in red) at $z = 0$ and $z = d$, which are related via the transfer matrix in Eq. (2.1).

optical functions stacking metasurfaces. Second, seminal early examples of metasurfaces use stacking to design function. An important family of examples is that of perfect absorbers like Salisbury screens, and patch-antenna reflective metasurfaces, in which arrays of resonant antennas are placed in front of a reflector [114, 127–136]. Such structures control reflected waves in amplitude, phase and polarization through constructive and destructive interference of scattering contributions from a ground plane and a scatterer array [114, 137]. These structures, of which we will present an example in the next chapter, essentially constitute a metasurface etalon, where both the round trip phase, controlled by separation, and the reflection phase of the metasurface reflector, control response [64, 131, 133, 136]. Beyond applications as antireflection devices, absorption enhancers in photodetection scenarios, and as metasurface pixels from which to build metasurface devices, these metasurface etalons also have been proposed for plasmonic colour printing and polarization multiplexing therein [138–142]. Expanding on this idea of metasurface etalons in which one reflector is a metasurface with engineered reflectivity, one can also envision more complex resonant structures, such as Fabry-Pérot resonators in which metasurfaces are inserted inside the cavity mode. These were proposed by Ameling et al. [94–97, 143] as high-Q plasmonic structures for sensing, in which classical analogues of vacuum Rabi splitting occurs [144], a hallmark of strong coupling. These types of structures are currently under intense scrutiny in the field of plasmon strong coupling and polaritonic chemistry [73, 98, 145–150], wherein researchers construct plasmonic-photonic resonators that are in their turn coupled to excitonic media. The relevance of that field lies in the pursuit of collective light-matter interaction phenomena at room temperature, such as exciton-polariton physics, condensation and lasing, and in the pursuit of controlling chemical reaction pathways and transport properties by shifting of energy levels through vacuum Rabi splitting [145, 146, 151].

Full-wave simulation of stratified systems that include metasurfaces quickly becomes infeasible with increasing complexity, owing both to the large overall structural dimensions of stacks, and to the nanoscale detail needed to resolve metasurface building blocks. Also, it would be inefficient to do full-wave calculations for each envisioned stack if instead there would be a simple modelling strategy in which a library of simulations for a basic set of metasurfaces could be re-used when layers are rearranged and reordered, without having to start numerical analysis from scratch. Here we present a simple modelling approach based in the standard transfer matrix method for stratified systems [152, 153], yet capable to include also metasurfaces. To this end we rearrange the scattering S-matrices of metasurfaces, i.e., the input-output relations that can be extracted from any other suited and dedicated simulation tool, into transfer matrix method form. This approach is similar to the work of Menzel et al. and Sperrhake et al., who developed S-matrix based models to analyze the polarimetric behavior of metasurface stacks [154, 155].

This chapter is structured as follows. We first present an overview of how to extend the simple transfer matrix method to include metasurfaces, and indicate how one should extract relevant observables from it. Next we show that this simple model gives surprising new insights in Salisbury screens for perfect absorption [114, 127–136], as well as in the problem of strong coupling of microcavity modes with metasurface resonances [94–97, 143]. Finally, we discuss the application of our modelling approach to strong coupling of metasurface etalons with excitonic media [98, 156].

2.2 Transfer matrix model for multilayer stack with interspersed metasurfaces

Figure 2.1 shows a sketch of the family of systems that we model in this chapter, which consists of an arbitrary stack of layers with parallel interfaces. The layers can be either standard homogeneous dielectric or metallic materials, or instead metasurfaces embedded inside a dielectric layer. For completeness, we first briefly introduce the standard transfer matrix method for layered systems, as is described at length in the seminal paper by Yeh, Yariv and Hong [152, 153].

2.2.1 Transfer matrix method for a standard homogeneous stack of layers

The optical properties of each layer are specified by its thickness d and refractive index $n = \sqrt{\epsilon}$. While our work is easily generalized to arbitrary incidence angle, here we deal with normal incidence only. At the heart of the transfer matrix method is the notion that one can relate the parallel field components E_x and H_y at the front side ($z = 0$) and the back side ($z = d$) of a slab by matrix multiplication

$$\begin{pmatrix} E_x(d) \\ H_y(d) \end{pmatrix} = M(k_d, d) \begin{pmatrix} E_x(0) \\ H_y(0) \end{pmatrix} \tag{2.1}$$

where $M(k_d, d)$ is the transfer matrix. For a single slab the transfer matrix M is easily derived through the use as auxiliary variables of forward and backward propagating fields in the slab, which are written as $E_x(z) = E_{\mathrm{f}} e^{ikz} + E_{\mathrm{b}} e^{-ikz}$ (suppressing time dependence $e^{-i\omega t}$). The auxiliary field H_y is proportional to the magnetic field, with multiplicative factor $i\omega$ suppressed throughout, since it is common to all H-fields independent of layer. The transfer matrix now follows by calculating H_y from E_x, and evaluating the fields at $z = 0$ and $z = d$. From the resulting equations one eliminates the auxiliary field $E_{\mathrm{f,b}}$, to obtain

$$M(k_d, d) = \begin{pmatrix} \cos(k_d d) & \frac{1}{k}\sin(k_d d) \\ -k\sin(k_d d) & \cos(k_d d) \end{pmatrix} \tag{2.2}$$

in which k_d is the wave vector $n\omega/c$ in the slab with thickness d and refractive index n.

The strength of the transfer matrix method is that the transfer matrix of an arbitrary stack of layers is obtained simply as the matrix product of all the single layer transfer matrices. This fact hinges on the fact that the boundary equations for electric and magnetic fields require both E_x and H_y to be continuous across interfaces, so that the fields at the back of a stack can be simply obtained from the field at the front by multiplying with each of the single layer transfer matrices in turn. The field behind the stack of thickness d_{st} is thus constructed from the product of transfer matrices and the field in front of the stack using

$$\begin{aligned} \begin{pmatrix} E_x(d_{\mathrm{st}}) \\ H_y(d_{\mathrm{st}}) \end{pmatrix} &= M_{\mathrm{st}} \begin{pmatrix} E_x(0) \\ H_y(0) \end{pmatrix} \\ &= M_N \cdot M_{N-1} \ldots M_2 \cdot M_1 \begin{pmatrix} E_x(0) \\ H_y(0) \end{pmatrix} \end{aligned} \tag{2.3}$$

From here on, we will denote with M_{st} the transfer matrix of a full stack, which we assume to be composed of layers $m = 1, 2, \ldots N$, with transfer matrix M_m.

Once the transfer matrix of an arbitrary stack has been constructed, it is straightforward to calculate the complex reflection and transmission coefficients r and t by inserting as field at the front of the stack (subscript L for 'lefthand side of the slab' or $z < 0$)

$$E_L(z) = E(e^{ikz} + re^{-ikz}) \quad z < 0 \tag{2.4}$$

and at the back of the stack (R for righthand side)

$$E_R(z) = E(te^{-ik(z-d_{\mathrm{st}})}) \quad z > d_{\mathrm{st}}. \tag{2.5}$$

This Ansatz specifies that the stack is illuminated only from the left ($z < 0$), and that at the other side, beyond the total thickness d_{st} of the stack, only a single outgoing wave exists. Evaluating these Ansatz fields at $z_{\mathrm{front}} = 0$ and $z_{\mathrm{behind}} = d_{\mathrm{st}}$, and noting that these must be related through the stack transfer matrix, we obtain

$$\begin{pmatrix} t \\ ik\,t \end{pmatrix} = M_{\mathrm{st}} \begin{pmatrix} 1+r \\ ik\,(1-r) \end{pmatrix}. \tag{2.6}$$

This equation results in explicit expressions for the complex reflection and transmission coefficients r and t of the entire stack in terms of the stack transfer matrix M_{st}.

2.2.2 Metasurface transfer matrix

Having revisited the standard transfer matrix for layered optical systems [152, 153], we now introduce the transfer matrix of a metasurface. Metasurfaces

generally provide a very large, resonant, optical response that can not be cast in a combination of a material thickness and refractive index. Instead, a metasurface is more naturally thought of as an infinitely thin sheet with a specified complex reflection and transmission coefficient r_a, t_a. We assume that these reflection and transmission coefficients for the metasurface in a homogeneous dielectric remain valid also when the metasurface is embedded in a thin dielectric slab of the same index, but inserted in a complex stack. The coefficients can thus be calculated by separate means, to serve as input for constructing a transfer matrix. In principle any full-wave method could be used. For our work we use a semi-analytical approach that constructs the response of a metasurface on the basis of scatterer polarizability, and using Ewald lattice summation to account for all the interactions in the lattice [61, 62, 64].

In order to construct a metasurface transfer matrix we specify the fields on both the left and righthand side of a metasurface of thickness 0 placed at $z = 0$ in terms of its complex-valued reflection and transmission coefficients. We suppose that the metasurface is simultaneously illuminated from the left by a field propagating towards the right ($E_{\rightarrow}e^{ikz}$ for $z < 0$) and by a field impinging on it from the right, hence propagating towards the left ($E_{\leftarrow}e^{-ikz}$ for $z > 0$). Accounting for the complex-valued reflection and transmission amplitudes yields the total electric field on the left E_L and right E_R

$$\begin{aligned} E_L(z) &= E_{\rightarrow}(e^{ikz} + r_a e^{-ikz}) + E_{\leftarrow} t_a e^{-ikz} \quad z < 0 \\ E_R(z) &= E_{\rightarrow} t_a e^{ikz} + E_{\leftarrow}(e^{-ikz} + r_a e^{ikz}) \quad z > 0. \end{aligned} \tag{2.7}$$

Here we have employed the constraint that the metasurface is assumed to be embedded inside a layer with the same refractive index on either side of the metasurface, so that both r_a and t_a are independent of the incidence side. To obtain the transfer matrix, one calculates from E_L, E_R also the magnetic counterparts, and relates the fields at $z = 0$, evaluated on the left and right of the metasurface, by eliminating the auxiliary fields $E_{\rightarrow,\leftarrow}$. In matrix form this yields

$$\begin{pmatrix} E_L \\ H_L \end{pmatrix} = \begin{pmatrix} 1 + r_a & t_a \\ ik(1 - r_a) & -ikt_a \end{pmatrix} \begin{pmatrix} E_{\rightarrow} \\ E_{\leftarrow} \end{pmatrix} \tag{2.8}$$

and

$$\begin{pmatrix} E_R \\ H_R \end{pmatrix} = \begin{pmatrix} t_a & 1 + r_a \\ ikt_a & -ik(1 - r_a) \end{pmatrix} \begin{pmatrix} E_{\rightarrow} \\ E_{\leftarrow} \end{pmatrix} \tag{2.9}$$

so that the metasurface transfer matrix that satisfies $(E_R, H_R)^T = M_{\mathrm{meta}}(r_a, t_a)(E_L, H_L)^T$ reads

$$M_{\mathrm{meta}}(r_a, t_a) = \begin{pmatrix} t_a & 1 + r_a \\ ikt_a & ik(-1 + r_a) \end{pmatrix} \begin{pmatrix} 1 + r_a & t_a \\ ik(1 - r_a) & -ikt_a \end{pmatrix}^{-1}.$$

For a metasurface in a homogeneous medium that is mirror symmetric in the $z = 0$ plane, it is necessary that $t_a = 1 + r_a$. It is important to note that this does not derive from energy conservation, but only from assumed mirror symmetry in the plane of the 2D lattice [157]. With this requirement, the metasurface transfer matrix becomes

$$M_{\mathrm{meta}}(r_a) = \begin{pmatrix} 1 & 0 \\ \frac{2ikr_a}{1+r_a} & 1 \end{pmatrix} \tag{2.10}$$

In essence this construction can be viewed as casting the S-matrix of a metasurface (relating outgoing to incident fields) into a transfer matrix (relating fields on either side of the interface to each other). This approach is hence strongly related to the metasurface S-matrix formalism of Menzel and Sperrhake et al. [154, 155].

2.2.3 An analytical model for the response of a simple resonant particle array

In principle, the metasurface transfer matrix $M_{\mathrm{meta}}(r_a, t_a)$ allows to insert the reflection and transmission of a metasurface as calculated by any modelling approach. In this chapter we focus for demonstration purposes on behavior of metasurface etalons in which the metasurface is simply a non-diffractive sheet of resonant nanoscale polarizabilities placed in a lattice, as for instance obtained by making sufficiently dense arrays of plasmon antenna particles [61, 62, 64]. To model reflection and transmission of such a layer one must first specify the polarizability of a single scatterer, then include its radiative damping to obtain a self-consistent t-matrix, and finally account for all the near-field and far-field multiple scattering interactions with its neighbors in the lattice. A didactic introduction is provided by de Abajo [61], while implementation details for arbitary lattice symmetries and polarizability tensors are listed in [62, 64]. In this work we assume that the polarizability is scalar, purely electric ($\mathbf{p} = 4\pi\epsilon\alpha_{\mathbf{E}}$) and we use a unit system in which polarizability $\alpha_{\mathbf{E}}$ has units of volume. The electrostatic polarizability α_0 of a single plasmonic particle as a function of frequency can be parametrized as [59]

$$\alpha_0(\omega) = \frac{V\omega_0^2}{\omega_0^2 - \omega^2 - i\omega\gamma} \tag{2.11}$$

with V a measure of scattering strength with units of volume, ω_0 a resonance frequency and γ an Ohmic damping rate. This expression is exact for metallic spheres with a dielectric constant specified by a Drude model, where γ is the Ohmic damping rate and V is proportional to the scatterer physical volume. Radiative losses can be taken self-consistently into account for a single scatterer by implementing a radiation damping term [59, 61]

$$\alpha_{\mathrm{dyn}}(\omega) = \frac{1}{1/\alpha_0 - i\frac{2}{3}k^3}. \tag{2.12}$$

The resulting polarizability is known as *dynamic* polarizability, or alternatively as *t*-matrix of the point scatterer [59, 61]. This *t*-matrix results in self-consistent extinction, scattering and absorption cross sections that for a Drude sphere match the dipolar contribution in its Mie expansion.

Following de Abajo [61], in order to find the effective polarizability of an array of particles one needs to incorporate an Ewald lattice summation technique to account for all the near- and far-field interaction between antenna particles. Accordingly, under normal incidence, the induced dipole moment in each scatterer reads

$$\alpha_{\mathrm{lat}}(\omega) = \frac{1}{1/\alpha_{\mathrm{dyn}} - \mathcal{G}}. \tag{2.13}$$

The term $\mathcal{G}$ represents a lattice Green function, i.e., a summation over the free space Green function that is generally dependent on incidence angle, lattice pitch, lattice symmetry, and polarization. While this expression thus can encode the full band structure and diffraction physics of plasmon antenna arrays [61, 62], here we focus on metasurfaces under normal incidence, that are so dense that there are no propagating grating diffraction orders. In this limit, the real part of the lattice Green function only induces a shift in resonance frequency that we incorporate into ω_0, while the imaginary part adds radiative damping according to

$$\mathrm{Im}\mathcal{G} \approx \frac{2\pi k}{\mathcal{A}} - \frac{2}{3}k^3$$

where $\mathcal{A}$ is the unit cell area [61]. It should be noted that the single-particle radiation damping is exactly cancelled by the lattice sum, and replaced by a term that takes into account the superradiant collective damping that increases with antenna density. Following de Abajo [61], the lattice reflectivity is

$$r_{\mathrm{a}}(\omega) = \frac{2\pi i k}{\mathcal{A}}\alpha_{\mathrm{lat}}(\omega) = \frac{2\pi i k}{\mathcal{A}}\frac{1}{1/\alpha_0(\omega) - \frac{2\pi i k}{\mathcal{A}}}, \tag{2.14}$$

while the lattice transmission is $t_a = 1 + r_a$. Note that the lattice reflectivity converges to a perfect reflector $r_a = -1$ in the limit of very strong and dense scatterers (large V and small $\mathcal{A}$).

2.2.4 Extracting local fields, induced dipole moments and dissipated power in a layer

The framework as described so far allows to calculate the complex-valued reflection and transmission of arbitrary multilayer stacks in which metasurfaces can be interspersed with dielectric and metallic planar layers, with the understanding that the two layers directly adjacent to a metasurface are chosen to have identical refractive index. One can obtain not only far field reflection and transmission but also the field inside any layer in the stack. To this end,

the formalism stipulates that one must first solve for the reflection r_{st} and transmission t_{st} of the stack using the full stack transfer matrix M_{st}. Next, one can calculate the field at the front side of a layer m (normalized to a unit strength incident field offered to the stack as illumination) by multiplying the field on the incident side $(1 + r_{\mathrm{st}}, ik\,(1 - r_{\mathrm{st}}))^T$ with the partial stack matrix $M_{m-1} \cdot M_{m-2} \ldots M_2 \cdot M_1$ that accounts for all layers up to m. Given the fields $(E_x(z_m), H_y(z_m)^T)$ at the front of the m^{th} slab, the electric field inside it simply reads $E(z) = E_{\mathrm{f},m} e^{ik(z-z_m)} + E_{\mathrm{b},m} e^{-ik(z-z_m)}$ (i.e. sum of forward and backward traveling waves, defined at Eq. (2.1,2.2), with

$$\begin{pmatrix} E_{\mathrm{f},m} \\ E_{\mathrm{b},m} \end{pmatrix} = \begin{pmatrix} 1 & 1 \\ ik & -ik \end{pmatrix}^{-1} \begin{pmatrix} E_x(z_m) \\ H_y(z_m) \end{pmatrix}. \tag{2.15}$$

Local absorption directly follows from the field inside a layer. The absorption in layer m [energy per unit of time and unit of area lost in layer m] is given by

$$\begin{aligned} \int_{\text{slab } m} \frac{1}{2}\omega\epsilon_0 \mathrm{Im}[\epsilon]|E(z)|^2 dz = \\ \frac{1}{2}\omega\epsilon_0 \mathrm{Im}[\epsilon]\Bigg\{ \frac{1}{2k''}\Big[|E_{\mathrm{f},m}|^2(1 - e^{-2d_m k''}) + |E_{\mathrm{b},m}|^2(e^{2d_m k''} - 1)\Big] + \\ \frac{1}{k'}|E_{\mathrm{f},m}||E_{\mathrm{b},m}|\Big[\sin(2k' d_m + \delta_m) - \sin\delta_m\Big]\Bigg\} \end{aligned} \tag{2.16}$$

where δ_m is the phase difference between the complex numbers $E_{\mathrm{f},m}$ and $E_{\mathrm{b},m}$ and where k' and k'' are resp. the real and imaginary part of the wavenumber k in layer m. The first two terms can be interpreted as the incoherent sum of contributions of the forward and backward propagating waves, which are exponentially damped due to absorption. The last term arises from interference, i.e., standing wave effects in the slab. For reference, the assumed input intensity is $\frac{1}{2}c\epsilon_0 n_0 |E|^2$ with n_0 the $z < 0$ refractive index, and $|E| = 1$ V/m the incident field strength.

In a similar vein, one can also determine the induced dipole moments in any metasurface inside the complex stack. Supposing that the metasurface is situated immediately after layer m in the stack, one can simply calculate the field at the frontside of the metasurface by multiplying the field on the incident side $(1 + r_{\mathrm{st}}, ik\,(1 - r_{\mathrm{st}}))^T$ (with r_{st} the full stack reflectivity already solved for) with the partial stack matrix $M_m \cdot M_{m-1} \ldots M_2 \cdot M_1$ that accounts for all layers up to the metasurface. Immediately to the left of the metasurface the field reads

$$\begin{pmatrix} E_L \\ H_L \end{pmatrix} = [M_m \cdot M_{m-1} \ldots M_2 \cdot M_1] \cdot \begin{pmatrix} 1 + r_{\mathrm{st}} \\ ik_0(1 - r_{\mathrm{st}}) \end{pmatrix}. \tag{2.17}$$

Inverting Eq. (2.8) immediately yields the impinging fields driving the metasurface, i.e.$(E_{\rightarrow}, E_{\leftarrow})^T$. The induced dipole moment per metasurface scatterer

is simply given by $\mathbf{p} = \alpha_{\text{lat}}(E_{\rightarrow} + E_{\leftarrow})$. The power absorbed by the antenna array per unit of area follows by determining the deficit between the Poynting fluxes immediately to the left and right of the metasurface

$$P = \frac{1}{2} c\epsilon_0 n_m \Big[\left(|E_{\rightarrow}|^2 + |E_{\leftarrow})|^2 \right) (1 - |r_a|^2 - |t_a|^2) - 4\text{Re}(r_a t_a^*)\text{Re}(E_{\rightarrow} E_{\leftarrow}^*) \Big]. \tag{2.18}$$

The first terms in this sum report the absorbed power if the waves driving the metasurface from the left and right would be added incoherently. The last term accounts for interference.

2.3 Salisbury screen as a metasurface etalon

2.3.1 Perfect absorption in metasurface etalons

In the remainder of this chapter we illustrate the power of the simple transfer matrix method to predict and understand the physics of simple metasurface stacks that are of large relevance in current research. The first example that we consider is that of a Salisbury screen, consisting of a simple metal mirror, a dielectric spacer and a resonant metasurface mirror [114, 127–136]. This structure can also be viewed as an etalon [64, 133, 136] in which the back reflector (metal mirror) is thick, while the front reflector is the metasurface which depending on density and frequency can range from semi-transparent to strongly reflective, and furthermore has a peculiar phase response (as we show experimentally in chapter 3). According to literature over the past decade, Salisbury screens can show perfect absorption in the metasurface antennas at particular resonance conditions, even if by themselves the particle arrays are only weakly absorptive. A schematic view is presented in Fig. 2.2 as sketches on the far left. This figure presents both the response of just particle arrays, and of envisioned Salisbury screens, as function of frequency ω (vertical axis on color plots) and etalon spacing d, for different antenna array densities. We choose each scatterer to have the properties $V = 6.9 \cdot 10^{-23}\text{m}^3$, $\omega_0 = 2.4 \cdot 10^{15}$ rad/s, $\gamma = 9.3 \cdot 10^{13}$ Hz. This corresponds with the scattering properties of antennas in the experiment resported in the next chapter, in which we used gold nanorod antennas [136], as verified by matching the resonance frequency, Ohmic damping, and extinction cross section ($\sigma_{\text{ext}} = 4\pi k \text{Im}\alpha_{\text{dyn}} \approx 0.088\ \mu\text{m}^2$) to finite element modelling of Au nanorods in glass (circa $100 \times 50 \times 40$ nm length, width and height). We assume the scatterers to be in a square lattice of pitch a, with a increasing from 100, 200, 350, 433 to 550 nm. The medium on the incoming side and in between mirror and metasurface is glass ($n_{\text{glass}} = 1.45$), while we assume as back reflector 50 nm of gold ($n_{\text{Au}} = 0.25 + 4.5i$, taken frequency independent). The frequency window in our plots corresponds to ca. 650—900 nm vacuum wavelength.

Figures 2.2a-e show that for just a single particle array with no back reflec-

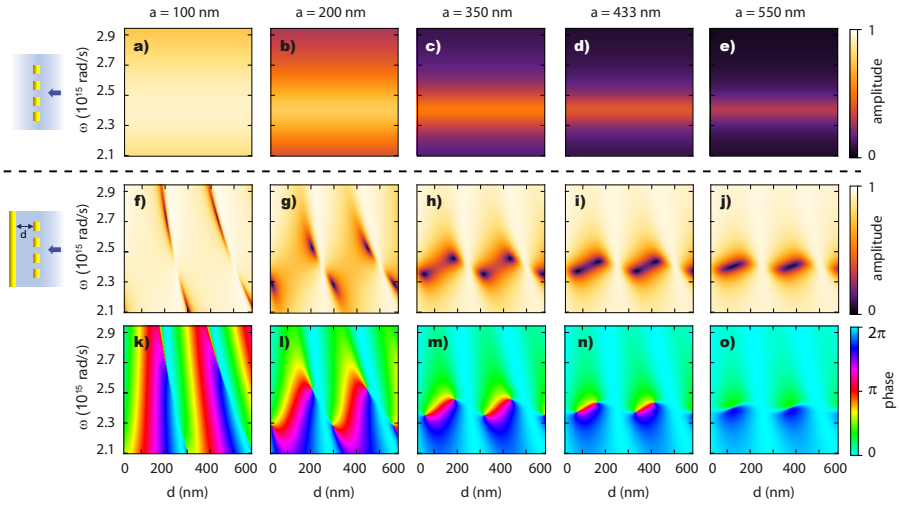

Figure 2.2: Calculated response of Salisbury screens in reflection. From left to right the columns display metasurfaces consisting of scatterers in a square geometry with a pitch increasing from 100 to 550 nm and with fixed antenna parameters $V = 6.9 \cdot 10^{-23}\,\mathrm{m}^3$, $\omega_0 = 2.4 \cdot 10^{15}$ rad/s and $\gamma = 9.3 \cdot 10^{13}$ Hz. Top row (a-e): amplitude response of the particle arrays as a function of frequency in absence of the backing mirror, showing a Lorentzian response around the resonance frequency ω_0. Center (f-j) and bottom (k-o) row show the full etalon response in amplitude and phase respectively, as a function of frequency and metasurface-mirror spacing d, employing a 50 nm Au back reflector. Reflection phase is referenced to that in absence of the array.

tor, the reflectivity not only strengthens, but also significantly broadens with antenna density. This is a signature of collective effects in antenna arrays, whereby superradiant linewidth broadening causes the lattice polarizability α_{lat} to be significantly different from the particle response for dense lattices. For the bare particle arrays, the maximum achievable absorption is fundamentally limited by symmetry to 50%, which is reached on particle resonance near 300 nm pitch [157]. Absorption drops for larger pitch as the metasurface becomes less strongly populated and hence more transparent, and conversely also drops for smaller pitch as the metasurface becomes more reflective. For the etalon-geometry the reflectivity maps as function of frequency ω and mirror-metasurface spacing d are significantly different (Fig. 2.2f-j). At the highest antenna density, the metasurface is practically a mirror across the entire frequency range, giving rise to etalon resonances, evident as pockets of absorption close to hyperbolas (contours of constant kd) in Fig. 2.2f. The main signature indicating that the metasurface is not a regular mirror but a dispersive reflector is that the etalon resonances show as asymmetric spectra, and with signature vanishing right at particle resonance ($2.4 \cdot 10^{15}$ rad/s). This can be traced to the metasurface reflection phase. With decreasing antenna

density the response evolves from a Fabry-Pérot-like response at large antenna density, to that of an isolated mirror with just isolated pockets of reduced reflection near antenna resonance (panel 2.2g). These appear only when the particle array is not in a node of the field reflected from the back mirror, i.e. *in between* the etalon resonances of panel Fig. 2.2f.

Looking more closely at the low reflectivity areas in Fig. 2.2f-i we find that there are points of identically zero reflection and hence perfect absorption. This is the well known phenomenon of *perfect* absorption [114, 127–136], which in literature has been described as a condition of critical coupling between radiative and nonradiative loss channels of a single-port resonance. More surprising is that corresponding phase plots (panels k-n, phase referenced to the back-reflector in absence of the particles) show singular points in the ωd-parameter space, around which the phase circulates and in which the phase is not defined. These points evidence the truly vanishing reflection observed in the corresponding amplitude plots. Moreover, it is evident that these singular points do not come alone but in fact appear as a countably finite numbers of pairs of opposite topological charge, with each pair contained between two perfect-etalon conditions (hyperbolas $kd = m\pi$, m integer). For dense arrays, these singularities are located very close to the resonance condition for a standard etalon, though at frequency detuning that is far from the bare particle resonance. For larger pitch and hence diluted lattices (Fig. 2.2m,n), the singular points move away from the etalon condition, and towards the points in parameter space that are centered on the bare lattice resonance frequency ω_0, and on spacer thicknesses exactly *in between* the etalon condition. Here the lattice is placed not at half-integer wavelengths from the backreflector, but is a quarter-wave offset, so as to be in an antinode of the standing wave generated by the back reflector. At pitches above circa 500 nm, the phase singularities annihilate, and absorption in the particles is no longer perfect (Fig. 2.2j,o). These findings thus reproduce the well-known appearance of conditions of perfect absorption in Salisbury screens in a model that is a simple transfer matrix model. At the same time it provides insights that go beyond the simple coupled mode analysis in literature [127–134] that neither foresees perfect absorption points to come in pairs, nor suggests singular phase response in parameter space. The topological nature of the phase singularities in parameter space might lead one to suspect that there is an underlying anomaly in the etalon eigenmode structure, as it is well known that, for instance, exceptional points and bound states in the continuum have topological properties. Following the general classification by Krasnok et al. [158], we assert that such physics is not at play here. According to Krasnok et al., eigenmodes correspond to complex-frequency poles of the S-matrix, while the zero reflection in the system that we describe is a zero of the S-matrix on the real axis. If one analyzes the S-matrix for this system (see Eq. (2.19) for a simplified model) at the etalon thickness where the antenna is right in the mirror's standing wave antinode, the S-matrix is found to carry a single pole

in the complex frequency plane that is accompanied by a single nearby zero. For low antenna density (no singular response), the zero is in the same half-plane as the S-matrix pole. As the antenna density is tuned, the zero reaches the real frequency axis, at which point perfect absorption appears. For larger antenna strength the zero has crossed the real frequency axis. At this point the structure does not provide its zero in reflection for the exact thickness where the antennas sit in the standing wave antinode, with reflection zeroes instead happening at adjacent spacing, i.e., in the pairs of points evident in Fig. 2.2. It should be noted that throughout, the S-matrix pole has multiplicity one. We refer the reader to chapter 3, Ref. [136], for experimental evidence for the proposed appearance and annihilation of pairs of phase singularities in these structures, as function of density and in the parameter spaced spanned by frequency and etalon spacing.

2.3.2 Metasurface etalons with near transparent mirrors

A particular advantage of the matrix method in which one can intersperse arbitrary homogeneous layers and metasurfaces, is that one can easily explore a variety of scenarios with realistic experimental conditions that are not accessible in even more simplified models, e.g. taking into account realistic refractive indices or layer thicknesses, e.g. ones that correspond to highly 'imperfect' Salisbury screens. Figure 2.2 showed that for a near-perfect back reflector, a Salisbury screen shows phase singularities and points of perfect absorption on the proviso that the metasurface in itself is sufficiently strongly scattering. Figure 2.2, however, also showed that a poor meta-mirror (antenna array oscillator strength below a certain threshold) causes the singularities to disappear. This raises the question whether the use of a similarly poor back mirror could retrieve these points of singular reflectivity. Qualitatively one might argue that if perfect cancellation of reflection is due to matching of the metasurface reflection constant and that of the back reflection, then the singular response should re-appear for dilute metasurfaces, if one concomitantly reduces also the back reflector reflection constant. Fig. 2.3a exemplifies exactly this point, for the least dense array considered in Figure 2.2j. While for the near perfect back reflector there are no singular points, once the mirror is replaced by one of just 5 nm thickness (partial reflectance), the pairs of points of zero reflection return, as shown in Fig. 2.3a. These are again accompanied by phase singularities in parameter space (shown in Fig. 2.3b), and a concomitant 2π phase swing for ω, d combinations boxed in by the singularities. A subtle point is that in this case zero reflection does not imply perfect absorption, as there is also a transmitted channel.

An *a posteriori* understanding of this re-appearance of points of zero reflection and phase singular appearance can be constructed from a simple two-layer Fabry-Pérot model wherein the reflectivity of an etalon reads [136, 157]

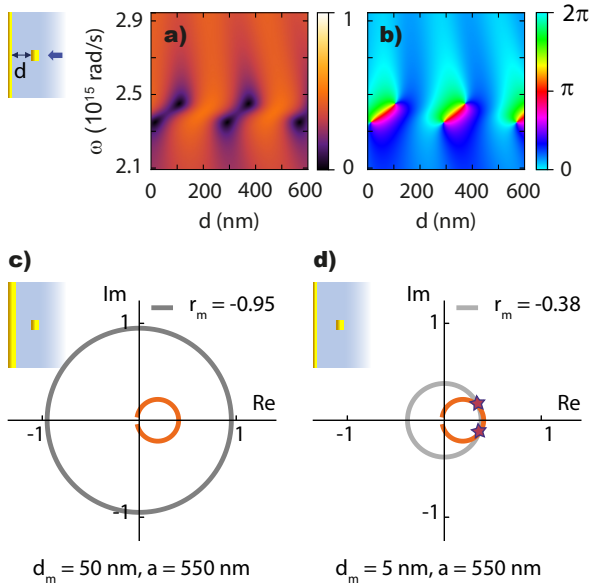

Figure 2.3: Calculated amplitude (a) and phase (b) response for the Salisbury screen in Fig. 2.2j,o, in which the reflectivity r_{m} of the back reflector has been decreased to match the reflectivity of the weakly scattering array, such that singular points in reflection are retrieved. c,d) Graphical construction of Eq. (2.20) in the complex plane, showing the trajectories that the right-hand and left-hand side (gray and orange respectively) of the equation trace out as a function of frequency. c) When a weakly scattering metasurface (pitch 550 nm) is combined with a highly reflective back reflector, the circles traced out by $r_{\mathrm{m}}e^{inkd}$ (gray) and $-r_{\mathrm{a}}(\omega)/(1+2r_{\mathrm{a}}(\omega))$ (orange) do not intersect. d) Reducing the back mirror reflectivity to that of a 5 nm Au layer results in crossing of the circles and retrieval of the singular points shown in a) and b).

$$r_{\mathrm{FPI}} = \frac{r_a + r_m(1+2r_a)e^{2iknd}}{1 - r_a r_m e^{2iknd}} \tag{2.19}$$

with r_a the metasurface reflectivity, r_m the back reflector reflectivity and n the etalon spacer index. This expression implies $r_{\mathrm{FPI}} = 0$ for the condition that

$$r_m e^{2inkd} = \frac{-r_a(\omega)}{1+2r_a(\omega)}. \tag{2.20}$$

This essentially prescribes a matching condition on the metasurface reflectivity $r_a(\omega)$ relative to the backreflector and etalon spacing. At the points of matching, reflection vanishes. The lefthand side $r_m e^{2inkd}$ circumscribes a circle of radius $|r_m|$ centered on the origin in the complex plane as one sweeps frequency. Instead, the right hand side for a metasurface with a Lorentzian resonance circumscribes a circle exactly touching the origin in the complex

plane, displaced along the real axis, and with a diameter that increases with increasing antenna oscillator strength and density. On this circle, frequencies far from resonance are close to the origin, while the resonance frequency corresponds to the point on the circle furthest from the origin. Figure 2.3c illustrates this behavior for a strong back reflector ($|r_m| = 0.95$, as in the case of the 50 nm thick mirror in Figure 2.2) yet a dilute metasurface (550 nm pitch). For these parameters, the metasurface is not sufficiently strongly scattering (i.e., orange circle is small) for crossings between $-r_a/1 + 2r_a$ and $r_m e^{2iknd}$ to occur. One route to obtain crossings is to increase antenna density or oscillator strength, which increases the orange circle ($-r_a/1 + 2r_a$) in size. This explains the emergence of pairs of singularities and perfect absorption above a threshold antenna density in Figure 2.2. Another route instead, is to *reduce* the back reflector reflectivity (radius of the circle $r_m e^{2iknd}$) to match the metasurface response. This is shown in Fig. 2.3d where r_m has been decreased to match the reflectivity of a 5 nm Au mirror. Crossings denoted by stars show that the condition in Eq. (2.20) is met and that, for the dilute metasurface that does not show any singular response when combined with a strong back reflector, zero reflection and phase singularities in reflection now must occur.

2.3.3 Birefringent Salisbury screens

In the analysis of the Salisbury screen we have so far considered polarization exactly along the main axis of the nanorod antennas. For rectangular array metasurfaces with plasmonic resonators that have their principal axis aligned with the array symmetry axis, it is straightforward to also analyze polarimetric responses, as one can separately calculate the polarization dependent responses r_x and r_y for the two principal axes from two scalar calculations. The total response to any incoming polarization can then be constructed by decomposing the input polarization in two orthogonal linear components, and coherent addition of the corresponding reflected fields. By way of example we examine the response of nanorod-array Salisbury screens, for which the strong phase and amplitude response for the polarization channel of the nanorod resonance should induce a strong linear dichroism (differential absorption between linear polarization components) and a strong linear birefringence (differential retardance). The following example highlights the potential of our transfer matrix method for the rapid analysis of metasurface-etalon based polarimetric components [119–121, 138–142, 154, 155].

We choose nanorod antennas to be resonant with x-polarization, such that r_x is the response previously shown (Fig. 2.2). We assume the orthogonal antenna resonance to lie far outside the frequency window of interest so that we can model r_y as the response in absence of the antenna array (i.e. a plain mirror). We report the amplitude and phase response in the co-polarized reflection channel in panels Fig. 2.4a,c,e,g (amplitude) and Fig. 2.4b,d,f,h (phase) for horizontal, vertical, diagonal linear, and circular polarization. When il-

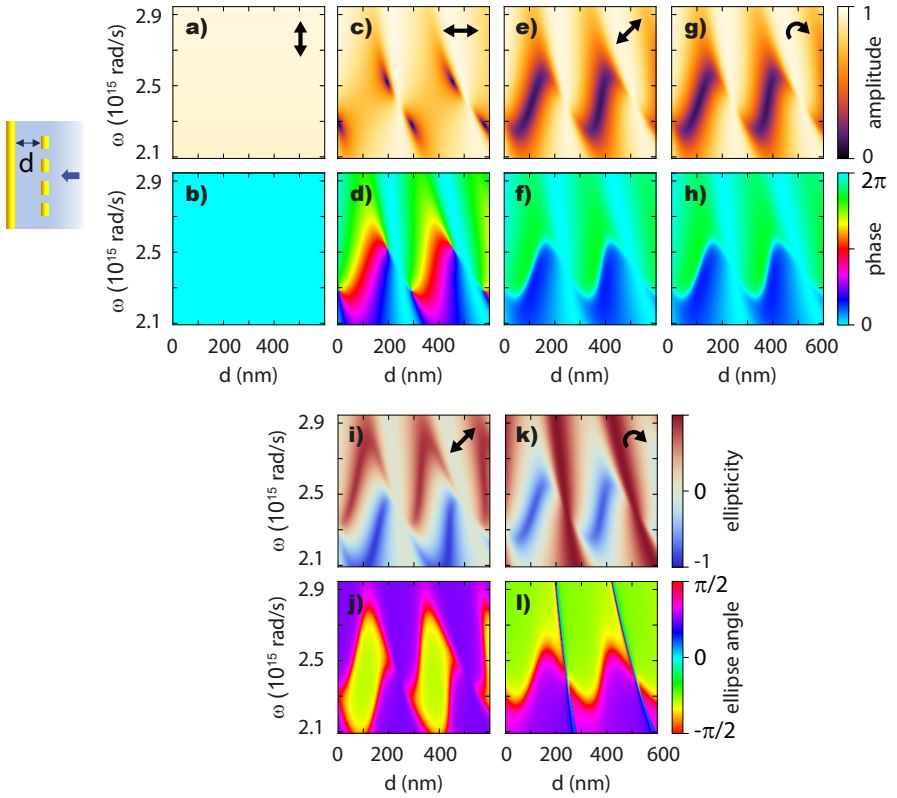

Figure 2.4: a-h) Polarization dependent amplitude and phase response of Salisbury screens in reflection, for a lattice of pitch 200 nm (other antenna parameters taken the same as in Fig. 2.2) and a back reflector of thickness 50 nm. The top right arrows denote the input polarization, and results shown are for the co-polarized detection channel. a,b) polarization orthogonal to the antenna resonance axis, c,d) polarization aligned with antenna resonance axis (i.e. plots identical to Fig. 2.2g,l), e,f) diagonal and g,h) right handed circular (RHC) polarization. i-l) Ellipticity parameters ϵ and α, a measure of circular polarization and orientation respectively, for the cases of diagonal and RHC input polarization. Diagonal and RHC plots are equivalent in amplitude and phase (e-h) for the co-polarized reflected channel, but entirely distinct in ellipticity (i-l).

luminating with polarization along one of the principal axes of the system, one simply obtains a flat response for the vertical y-polarization for which the metasurface is assumed transparent, and instead the resonance with strong phase features for the horizontal x-polarization already reported in Fig. 2.2g,l. With rotation of the polarization from horizontal to diagonal (see Fig. 2.4c,e), the points of zero reflection disappear. This is intuitively expected since the y-polarization component is still fully reflected, irrespective of whether the x-component experiences a strong phase and amplitude effect. At the same

time it is at first sight remarkable that for a band in parameter space *in between* the two x-polarization singular points the reflection is well below that in *both* the x and y channel. This is due to the fact that the x and y reflections are not in phase, leading to destructive interference. It is easy to show that the co- and cross-polarized reflectivity signature is strictly identical for diagonal and circular polarization, equalling $\frac{1}{2}[r_x \pm r_y]$ for co- resp. cross-polarization.

The linear dichroism and birefringence of nanorod-array Salisbury screens become evident when analyzing polarization conversion. We quantify the polarization state of reflected light upon diagonal and RHC polarized illumination through the polarization ellipticity ϵ and polarization ellipse major axis orientation α that fully characterize the ellipse that the electric field vector traces as a function of time. The ellipticity ϵ takes values between -1 and 1, such that ϵ is 0 for a linearly polarized field and $+1$ or -1 for right resp. lefthanded (RHC, LHC) circular polarization. The parameter α represents the orientation angle of the major axis of the polarization ellipse, and takes values from $-\pi/2$ to $\pi/2$, where 0 encodes for horizontal orientation (along x). These parameters can be directly calculated from a field vector (E_x, E_y) as

$$\begin{aligned} \epsilon &= \frac{2\mathrm{Im}[E_x^* E y]}{|E_x|^2 + |E_y|^2 + |E_x^2 + E_y^2|}, \\ \alpha &= \frac{1}{2}\mathrm{arg}[|E_x|^2 - |E_y|^2 + 2i\mathrm{Re}(E_x^* E_y)]. \end{aligned}$$

Fig. 2.4i and k show that the nanorod-based Salisbury screens strongly transform polarization, with ellipticity parameters that strongly depend on frequency and that can strongly differ from the input ellipticity. Fig. 2.4 i) shows that at diagonal, yet linear incoming polarization (zero ellipticity in input), the reflected polarization state is strongly elliptical except at the bands of near-unit reflection of x-polarized etalon resonances (color white for zero helicity). At this feature the reflected polarization is linear and diagonal . The ellipticity is reversed above and below this feature, with ellipticity close to ± 1 (nearing circular polarization, strong red resp. blue color). The feature of zero helicity pinpoints the locus in parameter space where r_x (phase plot in Fig. 2.4d) goes through a π phase shift. Similarly strong polarization conversion effects occur for circular input polarization (Fig. 2.4k,l). For frequencies well above and well below the range of perfect absorption features, the reflected polarization helicity is essentially conserved (red coloring). However, strong helicity conversion occurs at ω, d parameters that are boxed in between pairs of the x-polarization perfect absorption points. In these pockets incoming RHC illumination ($\epsilon = +1$) is reflected into the orthogonal LHC channel ($\epsilon = -1$). The loci of zero helicity ($\epsilon \sim 0$, white color in Fig. 2.4k) correspond to the loci where r_x crosses through $\pm\pi/2$ phase shift. The linear polarization that is reflected at these angles is diagonal, with the orientation angle α ($\pm\pi/4$ (green, purple) for diagonal polarization) changing sign when crossing the

antenna resonance.

To conclude, nanorod-antenna based mirror-metamirror etalons not only show pairs of perfect absorption and phase singularity points in their principal orientation axis, but also show a rich polarization behavior. In particular, they show very strong polarization rotation behavior due to a combination of linear dichroism and linear birefringence. This may have uses for realizing (lossy) quarter-wave and half-wave plate reflectors at specific operation points. Also since the polarimetric signature is directly related to the singular phase behavior for x-polarization, polarimetry could be used instead of interferometry to understand the phase response in x-polarization that accompanies perfect absorption. Our analysis method contributes to diversifying plasmonic color printing strategies to encode information in polarization degrees of freedom [119–121, 138–142, 154, 155].

2.4 Strong coupling in mirror-metamirror-mirror sandwiches

In the remainder of this chapter we analyze the physics of a second highly pertinent example of a stratified metasurface stack problem. This is the physics of strong coupling between the resonances of a microcavity spanned by two mirrors, and a resonant object placed inside its field. This is a seminal problem in quantum optics [144, 159, 160] as strong coupling of a single two-level system and a high Q cavity underlies cavity QED. Also classical, and collective strong coupling is a topic of large past and current interest [73, 144–149, 156, 161–163]. Already Ameling et al. [94–97] suggested that Fabry-Pérot resonators with plasmon antenna arrays inside them should display strong coupling, and should have hybrid plasmonic-photonic resonances that have high Q, yet may have locally enhanced fields. Currently groups are exploring the combination of metasurfaces and excitonic layers inside microcavity resonators [98].

To explore the physics of such systems we examine the response of symmetric stacks where we take the scattering particle arrays from the previous section, yet now sandwiched between thicknesses $d/2$ of glass and 20 nm Au reflectors, effectively forming a Fabry-Pérot cavity with a metasurface in the middle. We chose the mirror thickness to tune the etalon finesse. Figure 2.5 plots the calculated complex reflectivity r and transmission t in amplitude, and plots the induced dipole moment at the particles. We provide both the induced dipole moment normalized to the *peak* dipole moment $p(\omega_0)$ achieved in absence of the mirrors and on antenna resonance, and the induced dipole moment normalized to the dipole moment $p(\omega)$ achieved at the same frequency, in absence of the mirrors. Finally, the left column (panels Figure 2.5a,f) plots the response of the stack in absence of the scatterers, simply displaying the well known Fabry-Pérot modes in reflection and transmission, of which the width is determined by the quality factor of the etalon through the reflec-

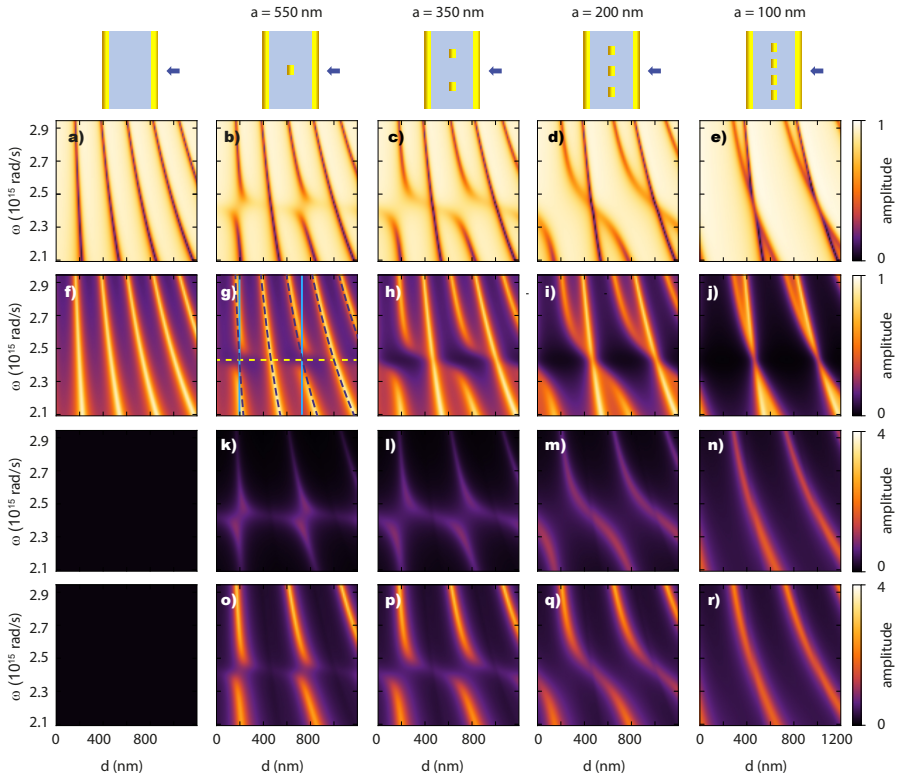

Figure 2.5: Calculated response of scattering nanoparticle arrays sandwiched between 20 nm Au mirrors, as a function of cavity length and frequency. Nanoparticle parameters are taken the same as in Fig. 2.2. Columns from left to right: no array, pitch 550, 350, 200 and 100 nm. The first two rows plot reflection (panels a-e) and transmission amplitude (panels f-j). Panel g) is overplot with Fabry-Pérot resonance lines (dark blue dashed) and a line indicating the scatterer resonance frequency ω_0 (yellow dashed). We take crosscuts (bright blue solid) through their points of intersection for the first and third order mode to estimate the mode splitting due to the presence of the array (see also Fig. 2.6). The third row (panels k-n) plots the dipole moment $|p|$ of the array, referenced by the maximum dipole moment in the bare array. The bottom row (panels o-r) plots $|p|$ referenced by the frequency dependent $|p(\omega)|$ of the bare array. The bottom two rows are both plot between 0 and 4 for comparison.

tivity of the mirrors.

Once one introduces a resonant metasurface, where we vary the pitch to vary the strength of the inserted perturbation, anticrossings appear around the resonance frequency of the scattering array (Figure 2.5b,g). As also observed in full-wave simulations by Ameling [94–97], these anticrossings only appear for the symmetric modes, which have a maximum at $d/2$. The anti-symmetric modes have no field overlap with the particles and hence show no crossing.

Increasing the density from 550 nm pitch further to 350, 200 and 100 nm pitch (Fig. 2.5c-e and h-j), the crossings become increasingly pronounced and it becomes apparent that branches on either side of an unperturbed mode bend towards one another and merge. Qualitatively, these results match the simulations by Ameling [96, 97]. The magnitude of the induced dipole moment in the scattering array, normalised to the dipole moment that would be induced in the same scattering layer for the same incident field, but without the cavity is significantly enhanced only for a large array pitch (very low density) and for large detuning from particle resonance (intrinsically small response per antenna). The enhancement arises as a consequence of the fact that the bare etalon enhances the circulating power in the cavity, but is counteracted by collective scattering effects for dense arrays and small detunings. Indeed for dense arrays, and near resonance, the net dipole moment is comparable to, or even reduced, compared to that achievable with just the array alone. This is a direct indication that collective effects put a limit on the achievable polarization in a sheet on basis of flux arguments: the total flux that the polarized sheet radiates and/or absorbs can never exceed the flux of the input field. This should be contrasted to reports for cavity-antenna hybrids with single antennas [90, 164, 165], and to the notion of Ameling et al. that plasmon array etalons allow to boost the sensitivity of, e.g., refractive index sensors, by combining high Q with enhanced fields [94–97]. It is only true for weakly scattering antennas that plasmon antenna enhancement and microcavity field enhancement effects add. For strongly scattering antennas collective effects, i.e., radiation damping limit the enhancement.

2.4.1 Rabi splitting

The analysis presented sofar in essence reproduces the full-wave simulation results of Ameling for similar structures [94–97]. The advantage of our matrix method is that parameters can be explored with ease, for instance to map the strong coupling as function of metasurface scattering strength quantitatively. A first order approach to quantify the strong coupling strength is to establish the (classical vacuum) Rabi splitting from response function spectra taken at etalon thicknesses d at which the bare etalon has its resonance frequency coincident with the particle resonance ω_0 [166]. An example spectrum is shown in Figure 2.6a. While one could attempt to fit a full model to the transmission line shape, we take the splitting simply as the frequency difference $\Delta\omega$ between the two maxima. This difference is plotted in Fig. 2.6b as a function of scatterer volume V for pitches 200, 350 and 550 nm. A square root dependence on the scattering V is qualitatively apparent, and more clearly exemplified by Fig. 2.6c that shows a linear behavior of $\Delta\omega$ as a function of $\sqrt{V}$. Qualitatively this square root behavior is consistent with common knowledge for cavities filled with polarizable media that state that the Rabi-splitting should scale with the square of the oscillator strength of atoms in the medium [144–146].

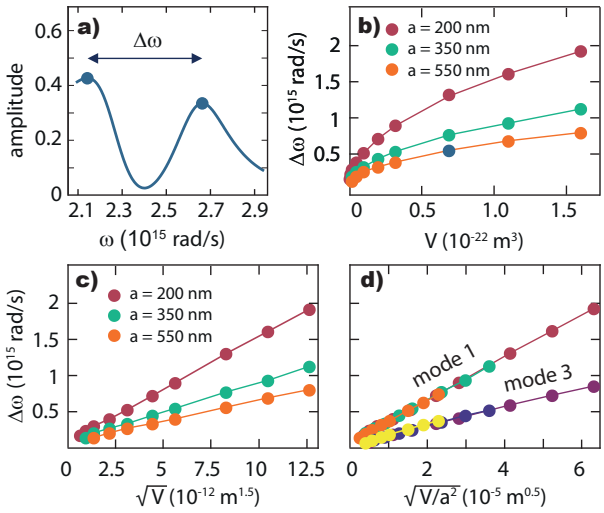

Figure 2.6: a) Spectrum at the first order bare-etalon resonant thickness indicated as a vertical line in Fig. 2.5g (antenna array properties: pitch 550 nm, and $V = 6.9 \cdot 10^{-23}\mathrm{m}^3$, $\omega_0 = 2.4 \cdot 10^{15}$ rad/s, $\gamma = 9.3 \cdot 10^{13}$ Hz as in Fig. 2.2). Maxima denoted by blue dots are used to estimate the Rabi splitting $\Delta\omega$ that measures the coupling strength between lattice and cavity mode. b) Calculated splitting $\Delta\omega$ as a function of scatterer volume V, for pitches 200, 350 and 550 nm. The blue dot corresponds to $\Delta\omega$ from a). c) By plotting $\Delta\omega$ as function of $\sqrt{V}$, the expected scaling with the square root of oscillator strength is evident. d) $\Delta\omega$ as function of $\sqrt{V/a^2}$ shows that a given mode splitting is proportional to the square root of density and oscillator strength, with a proportionality constant dependent on the mode order (shown for first and third mode). In b,c,d) the lines serve as a guide to the eye.

Accordingly, one would also expect the splitting to increase with the square root of particle density, meaning an overall scaling $\Delta\omega \propto V/a^2$ (where a is lattice pitch). This expectation is verified in Fig. 2.6d which shows that for each given mode order, the splittings as function of V/a^2 all collapse on a straight line. For higher order modes, the crossing reduces, as expected due to the more extended spatial mode (wider etalon) yet fixed amount of polarizable matter placed in it. The scaling of Rabi-splitting with the square root of plasmon antenna density was in fact observed in Ref. [98], where Rabi-splitting was observed in etalons with square lattices of disk-like plasmon particles at three different densities.

2.4.2 A metasurface is different from a dispersive medium in a cavity

At first sight, the physics of strong coupling between Fabry-Pérot modes and a particle array resonance may appear to be almost trivially identical to the

signature of classical vacuum Rabi splitting obtained with linear dispersive media inserted in a cavity, as was first discussed in the seminal paper by Zhu et al. [144]. Indeed, the scaling $\Delta\omega \propto \sqrt{\rho f}$ where f is a measure for oscillator strength per scatterer and ρ for number density, is identical to that expected for an atomic gas filling an etalon (Fig. 2.7a). That this analogy is nonetheless not straightforward is obvious firstly from the fact that the physics of a thin metasurface can not be cast in terms of an assigned dispersive refractive index, and second from the fact that for a metasurface it would not be clear which polarizability $[\alpha_0, \alpha_{\mathrm{lat}}, \alpha_{\mathrm{dyn}}]$ should be relevant to determine the anticrossing.

When inserting a linear dispersive medium into a cavity (mirror spacing d, see Fig. 2.7a), a Rabi splitting comes about because the optical roundtrip path length $2n(\omega)d$ allows matching of the resonance condition more than once for the same mode order when $n(\omega)$ is dispersive. Usually this occurs in media in which only a small variation in refractive index occurs due to an atomic or excitonic resonance. A small index variation nonetheless translates to a significant phase increment due to propagation over the full thickness of the excitonic medium. For a regular dispersive medium, one can imagine a number density ρ of atoms with polarizability α filling a slab of width d_a, so that the round trip path length reads $2n(\omega)d \approx 2(d - d_a) + 2d_a\mathrm{Re}[(1 + \frac{1}{2}\rho\alpha)]$. This is an approximate result that uses the fact that $n^2 = \epsilon = 1 + \rho\alpha$ can be approximated to $n = 1 + \frac{1}{2}\rho\alpha$ for excitonic media where $\rho\alpha \ll 1$. The seminal work of Zhu [144] applies this with $d_a = d$. The linear contribution of α to the propagation delay ultimately guarantees the square root scaling of splitting with density and oscillator strength, under the assumption of a Lorentzian polarizability of the same form as chosen in Eq. (2.11). One could attempt to cast the physics of a thin metasurface into that of a linear dispersive medium by assuming the metasurface to also be a slab of thickness d_a

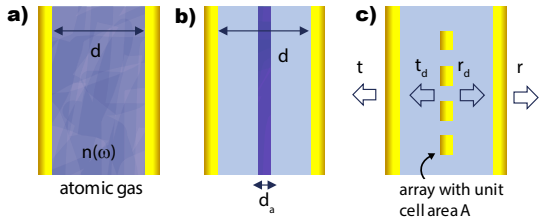

Figure 2.7: a) Sketch of an etalon entirely filled with a dispersive medium with refractive index $n(\omega)$. b) Etalon in which all polarizable material from a) is bunched into a slab of thickness d_a. c) Etalon in which the perturbation is viewed as a strongly dispersive *reflector*, essentially transforming the system into two coupled cavities coupled through a partially transparent membrane in the middle. A metasurface is a strongly dispersive membrane. t_d (r_d) and t (r) are transmission (reflection) coefficients of the center mirror and the outer mirrors respectively. Importantly, both case (b) and (c) show strong coupling, but (c) can not be described as the limit $d_a \to 0$ of panel (b), i.e., a metasurface can not be consistently viewed as the limit of an increasingly thin but polarizable slab.

filled with polarizable medium and inserted into the cavity, and calculating the propagation delay over its thickness. This is the approach suggested by Ameling [96]. Since for a metasurface the behavior is conceptually that of an infinitely thin polarizable sheet, one should then take a limit where d_a is taken to zero yet the integrated polarizability is kept constant (Fig. 2.7b,c). In fact this limiting procedure can not be consistently done. The round trip path length over just the hypothetically inserted slab is $2n(\omega)d_a = 2d_a\mathrm{Re}[\sqrt{1+\rho\alpha}]$. Since for a metasurface the polarizability is bunched in a small thickness with one object per 2D unit cell area $\mathcal{A}$ (see sketch in Fig. 2.7b) one has $2n(\omega)d_a = 2d_a\mathrm{Re}[\sqrt{1+\frac{\alpha}{\mathcal{A}d_a}}] \approx 2\sqrt{\mathrm{Re}[d\alpha/\mathcal{A}]}$ in the limit $d_a \to 0$, since now the polarizable matter term dominates. This immediately leads to an inconsistent scaling of Rabi splitting with polarizability at fixed small d_a, and furthermore is demonstrably inconsistent since in the limit of vanishing d_a, the resultant splitting is not independent of d_a. The root cause of the fact that a metasurface does not map on a dispersive slab is that refractive index alone only accounts for the phase retardation due to propagation through a slab and not for the impedance mismatch that is responsible for strong reflection and transmission at the interfaces of the slab. A metasurface constitutes a large impedance mismatch. This appears to have been overlooked by Ameling et al. [96].

Meta-mirror in the middle model

Instead of treating the particle array layer as a dispersive slab that modifies phase through propagation delay, we argue that it should be viewed as a strongly dispersive reflective boundary condition in the middle of a Fabry-Pérot resonator (Figure 2.7c) which induces no propagation delay but a strong phase pickup upon reflection/transmission. As approximate model, we evaluate the 'membrane in the middle' toy model proposed by Jayich et al. for cavity optomechanics [167]. This model assumes a Fabry-Pérot cavity with outer mirror amplitude transmission and reflection constant r, t and membrane reflection and transmission constant r_a, t_a. Solving in the specific case of a metasurface placed in the middle leads to the transmission

$$t_{\text{stack}} = -\frac{(r_a+1)t^2e^{ikd}}{r^2(2r_a+1)e^{2ikd}+2rr_ae^{ikd}-1} \tag{2.21}$$

where we have already used $t_a = 1+r_a$. In the limit of zero metasurface reflectivity this expression reverts to that for an etalon of thickness d, while for near unity reflection resonances characteristic for etalons of length $d/2$ appear. To analyze the appearance of strong coupling, one can use the method proposed by Zhu [144]. For near-perfect end-reflectors the denominator is of the form $-1+Ae^{i\varphi}$, showing resonances when $\varphi = 0 \bmod 2\pi$. Therefore, one can analyze φ, which for the 'empty' etalon simply traces the roundtrip phase $2nkd$, showing a linear behavior versus frequency crossing zero modulo 2π at each

resonance. If the cavity is filled with a traditional linear dispersive medium one sets $k = \omega n(\omega)/c$, yet $r_d = 0$ (no metasurface), reproducing exactly the model of Ref. [144]. Instead one can treat also the case of a metasurface-in-the-middle (set $k = \omega/c$, yet r_a as in Eq. (2.14)).

Figures 2.8a-f plot reflection, transmission and the phase φ obtained from Eq. (4.1) for both a traditional dispersive medium filling the cavity, and for a metasurface. As parameters we use $(r, t) = (-0.92, 0.34)$ (equivalent to 11.5% transmission and 4% absorption) for the reflectors. For panels a-c we assume a dispersive atomic gas of refractive index $n(\omega) = 1 + \frac{1}{2}\rho\alpha_0(\omega)$ with $\omega_0 = 2.4 \cdot 10^{15}$ rad/s, $\gamma = 4 \cdot 10^{13}$ s^{-1} and $V_{\text{atom}} = 8 \cdot 10^{-27}$ m^3 inserted in α_0 (Eq. (2.11)), at density $\rho = (10\,\text{nm})^{-3}$ so that the maximum change in refractive index $\Delta n \sim 0.12$. For the metasurface we use r_a given by Eq. (2.14) with identical resonance frequency and damping as for the atomic gas, but with $V = 4.8 \cdot 10^{-24}$ m^3 and $A = (200\,\text{nm})^2$ (extinction circa 50%, lattice and gas chosen to result in the same Rabi splitting). In Figure 2.8a-c, the dispersive medium causes strong coupling for etalon modes of all orders. For the metasurface case such splitting is only observed for modes with a central

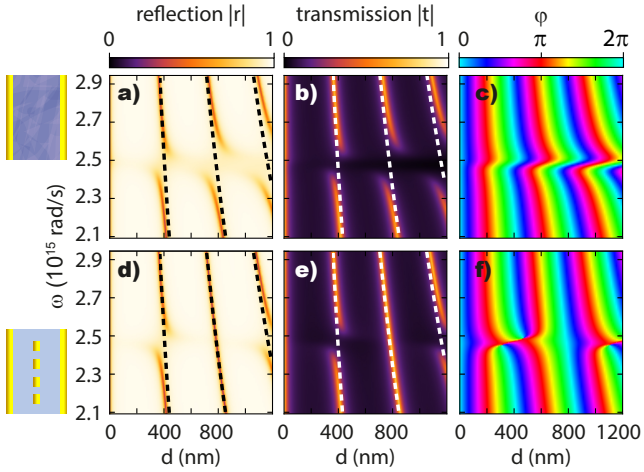

Figure 2.8: Reflection, transmission, and phase analysis of the meta-membrane in the middle model. Top row: the cavity contains a dispersive atomic medium, but no metasurface. The reflection and transmission show strong coupling for all modes. Analyzing the argument φ when identifying the denominator of Eq. (4.1) with $-1 + Ae^{i\varphi}$ shows the dispersive medium determining the propagation phase. According to Ref. [144], etalon resonances occur as zero crossing of φ, when taking vertical cross cuts at bare-etalon resonant thicknesses. Bottom row: same for a metasurface, and no atomic medium. Only every other (symmetric) mode splits. The φ-landscape is markedly different from the top row. We assume a dispersive atomic medium with $\omega_0 = 2.4{\cdot}10^{15}$ rad/s, $\gamma = 4{\cdot}10^{13}$ s^{-1} and $V_{\text{atom}} = 8{\cdot}10^{-27}$ m^3 inserted in α_0, at density $\rho = (10\,\text{nm})^{-3}$. The metasurface has identical resonance frequency and damping as the atomic gas, but with $V = 4.8 \cdot 10^{-24}$ m^3 and $A = (200\,\text{nm})^2$.

anti-node in the cavity, commensurate with Fig. 2.5. This is not a consequence of the metasurface nature but results from the positioning in the cavity. The phase increment φ for a bare etalon simply shows hyperbolic equiphase lines (constant kd). For a dispersive atomic gas filling the cavity, a dispersive feature around the material resonance becomes apparent, which essentially reports the dispersive, real part of refractive index n. For the assumed metasurface, however, the dispersive feature has a markedly different shape, with very sharp variations, and phase singularities.

Following Zhu [144], one finds the Rabi splitting by identifying the zero-crossing of φ in spectra taken at constant thickness taken right at the resonant thickness for zero detuning, i.e. taking vertical crosscuts through Fig. 2.8c,f at $d = m\pi cn/\omega_0$ (m the mode order). Figures 2.9a,b show as example φ for the first symmetric cavity mode for both the case of a linear dispersive homogeneous medium and a metamirror in the cavity. The phase evolves from a straight line in absence of polarizing material ($V = 0$), to a curve with additional zero crossings symmetrically placed around the resonance frequency ω_0, and increasingly moving away from ω_0 when the oscillator strength is increased. For an excitonic medium this exactly reproduces the work in Ref. [144], wherein the dispersive feature causes a modest phase advance and delay, in proportion to the small dispersive real part of the Lorentz line contribution to the refractive index ($\frac{1}{2}\mathrm{Re}\rho\alpha$). Linear increments in oscillator strength and density ρV_{atom} cause the phase variation away from the $V = 0$-line at any given frequency to vary proportionally. The concomitant mode splitting then traces the well-known square root behavior with increasing ρV_{atom}. For the metasurface (Fig. 2.9b) the phase behavior is shown for densities and linearly increasing particle oscillator strengths V that correspond to identical Rabi splittings as for the atomic gas example. The phase profiles are nonetheless quite different since the phase variation near zero detuning is very large already for modest metasurface characteristics, and crosses through π. Thereby the dispersive correction to the bare etalon line is replaced by a monotonic behavior, i.e., an S-curve with a full 2π phase swing. Even if for frequencies *in between* the zero crossings the phase swing is large and no longer linearly proportional to V, the *location* of the zero crossings nonetheless still scales with the square root of V.

2.4.3 Splitting in the limit of weak polarizability

In the limit of a weakly reflective metasurface, for which $r_d = 2\pi ik/A\alpha \ll 1$, and as long as splittings remain small compared to the resonance frequency ω_0, and for electrostatic Lorentzian polarizabilities of the form $\alpha_0 \approx \omega_0^2 V/(\omega_0^2 - \omega^2 - i\omega\gamma)$ one can analytically derive the location of the zero crossings of φ. In

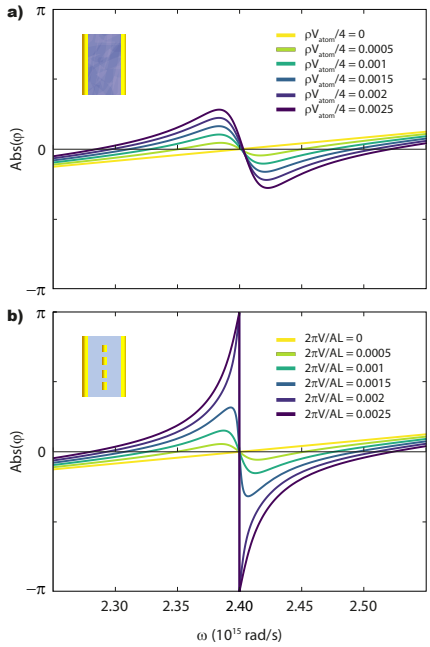

Figure 2.9: The argument φ when viewing the resonant denominator of Eq. (4.1) as $-1 + Ae^{i\varphi}$ as function of frequency, and at the etalon opening where the bare etalon has its resonance frequency at the resonance $\omega_0 = 2.4 \cdot 10^{15}$ s^{-1} of the inserted species. According to Ref. [144] zero-crossings correspond to the Rabi-split normal mode frequencies. Panel a) is for a homogeneous atomic gas, and panel b) for a dispersive metasurface. Different line colors vary oscillator strength and density in linear increments. Note how the zero crossings move away from ω_0 in proportion to the square root of the oscillator strength. Finally, we have taken oscillator strengths that correspond to *identical* location of the zero crossing in a) and b). Nonetheless, the phase variation for frequencies *between* the crossings is strongly different. Parameters as in Fig. 2.8, with oscillator strength V varied as indicated in the legend.

the limit of zero damping, they read for a metasurface

$$\omega_\pm = \omega_0 \left(1 \pm \sqrt{\frac{2\pi V}{\mathcal{A}L}}\right), \tag{2.22}$$

and for a dispersive atomic gas filling the complete cavity

$$\omega_\pm = \omega_0 \left(1 \pm \sqrt{\frac{\rho V_{\text{atom}}}{4}}\right). \tag{2.23}$$

Although the underlying variation of φ is quite different, the splitting follows a very similar scaling at small polarizability, namely a proportionality to the

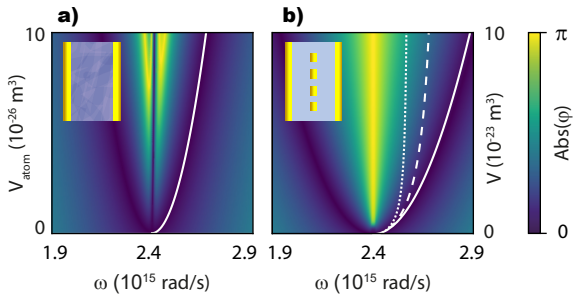

Figure 2.10: Color plots of $|\varphi|$ with φ defined from equating the resonant denominator of Eq. (4.1) to $-1 + Ae^{i\varphi}$, as a function of oscillator strength and frequency, for fixed etalon opening chosen such that the bare etalon has its resonance frequency at the resonance $\omega_0 = 2.4 \cdot 10^{15}$ s^{-1} of the inserted dispersive medium (panel a) resp. metasurface (panel b). The white parabola in a) overplots Eq. (2.23). Also for the resonant metasurface case, the splitting traces a parabola (white continuous line, Eq. (4.3). This is surprising, as this prediction takes the *static* polarizability as input, whereas the dynamic and lattice polarizabilities that determine the single-particle and collective antenna scattering strength respectively are strongly different. Dashed and dotted lines show the Rabi splitting if one would have to correct V in Eq. (4.3) with the on-resonance dynamical resp. lattice radiative correction factor (see Eq. (2.24)). Parameters as in Fig. 2.8.

square root of the oscillator strength parameter V and the number of oscillators placed in the mode. An apparent difference is that for a metasurface the splitting will reduce with etalon length L (i.e., for higher order modes), while for a cavity completely filled with an excitonic medium, the splitting is instead constant. This is due to the fact that in the excitonic case a longer cavity also contains more oscillators, whereas for a metasurface the number of oscillators is fixed with varying L. Figure 2.10 shows color plots of the (full, unapproximated) $|\varphi|$ as function of frequency and oscillator strength. The zero crossings can be traced as the contour of zero $|\varphi|$ (dark blue), and correspond well with the approximate expressions Eq. (4.3,2.23) over a large range of oscillator strengths.

2.4.4 Splitting at strong polarizability

A remarkable finding in Figure 2.10 is that the approximate expressions for the Rabi splitting versus oscillator strength even hold for very large oscillator strength. For the metasurface this is especially surprising, since one can ask *which polarizability* is actually a physical attribute of a scatterer. The polarizability that one would derive from a scattering or extinction measurement on a single scatterer, or instead from numerical full wave simulation [168], is the *dynamic* polarizability α_{dyn}, and not the static polarizability α_0. The polarizability that one would measure for an antenna in a lattice is in fact different from both, as the *lattice* polarizability α_{latt} is modified by superradiant,

i.e., collective, radiative damping. The on-resonance lattice polarizability is smaller than the static polarizability by a factor

$$\left.\frac{\alpha_{\mathrm{latt}}}{\alpha_0}\right|_{\omega=\omega_0} = \frac{1}{1+\frac{2\pi k_0 V}{\mathcal{A}}}. \tag{2.24}$$

As the dashed and dotted curves in Fig. 2.10b show, if one would assume the on-resonance dynamic or lattice polarizability to determine the Rabi splitting instead of just V, Rabi splittings would be up to a factor 2 smaller. Thus Figure 2.10 demonstrates that even though the evaluation of the metasurface-in-the-middle model actually uses the *lattice* polarizability, the Rabi splitting finally traces out Eq. (4.3) which *only* contains the electrostatic oscillator strength parameter V without the dynamic, i.e. k-dependent correction factor for the lattice. This is a remarkable finding, since the electrostatic polarizability is not actually an observable in any optical scattering experiment or full wave calculation. Our remarkable finding can be rationalized by noting that the usual statement that the *on-resonance* polarizability determines the magnitude of the Rabi splitting does not hold. The radiative correction is very large on resonance, but actually it is small far away from particle resonance. This makes the dynamic and lattice polarizability strongly non-Lorentzian. *At the frequencies of the zero-crossings* of φ the lattice polarizability is actually very close to the electrostatic polarizability at the same frequency, even though on resonance the difference is large.

2.5 Excitonic materials combined with resonant metasurfaces in etalons

There is currently a large interest in strong coupling of Fabry-Pérot resonators with excitons in 2D transition metal dichalcogenide (TMDC) materials, large oscillator strength organic systems like J-aggregates, as well as various types of 2D and 3D semiconductors [73, 144–149, 156, 161–163]. The rationale is that strong coupling gives access to, for instance, strongly nonlinear photonics via excitonic nonlinearities, which in turn gives rise to exciting opportunities for bistable optical devices, nonlinear sensing, and classical and quantum hardware optical Ising simulators [169, 170]. Recent experimental reports include strong coupling of microcavities and plasmonic arrays with organic dye molecules [73, 145, 146, 148], extremely dense organic molecular ensembles that form J-aggregates [149], and for instance 2D transition metal dichalcogenide flakes [147, 163]. These recent reports in fact build on experiments pioneered by Weisbuch [161] (III-V microcavities and quantum wells) and Lidzey [162] (microcavities with organic excitonic layers).

For decades, the transfer matrix has been used to predict classical strong coupling in microcavities filled with J-aggregates, quantum wells, or other

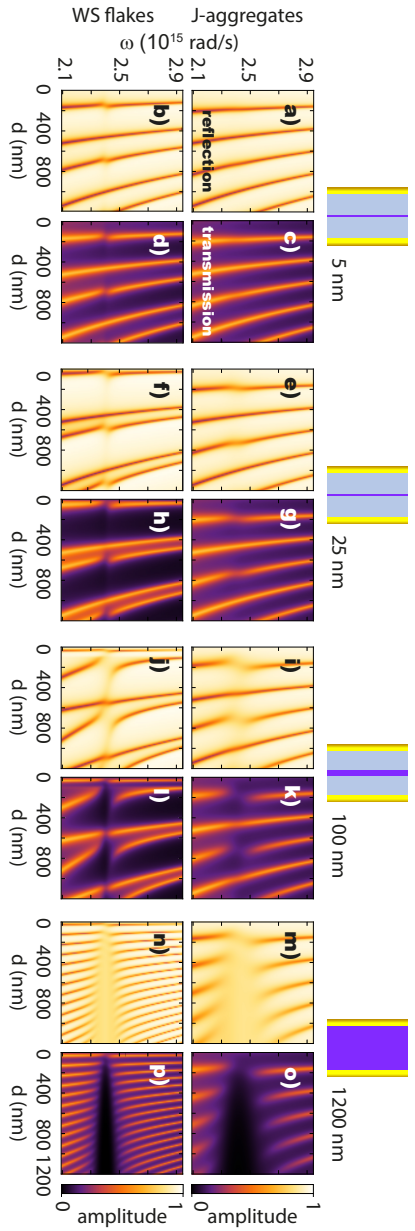

Figure 2.11: Calculated reflection and transmission for Fabry-Pérot etalons with an increasing thickness d_{exc} of excitonic material placed in its center (from left to right: 5, 25, 100 nm and completely filled), as a function of total etalon width d and frequency ω. The top row is for J-aggregates (values from Ref. [149]) while the bottom row is for WS_2 (values from model reported in Ref. [147]). For the first three panels only $d > d_{\mathrm{exc}}$ should be considered.

excitonic materials [144–146, 161, 162]. As model for the dielectric constant of such layers we use

$$\epsilon_{\text{polaritonic}} = n_{\text{bg}}^2 + 2\Delta n \frac{\omega_{0,p}\gamma_{0,p}}{\omega_{0,p}^2 - \omega^2 - i\omega\gamma_{0,p}}.$$

The model accounts for a background refractive index n_{bg}, and reparametrizes oscillator strength such that Δn is approximately the magnitude of the complex refractive index change on resonance. Figure 2.11 shows example etalon transmission for J-aggregates ($\Delta n = 0.8, \omega_{0,p} = 2.4 \cdot 10^{15}$ s^{-1}, $\gamma_{0,p} = 1.7 \cdot 10^{14}$ s^{-1} and background index $n_{\text{bg}} = 1.55$ (values commensurate with Ref. [149] for TDBC in a poly(vinyl) alcohol, with adjusted resonance frequency to match the plasmon antennas assumed throughout in this chapter), and for WS_2 flakes ($\Delta n = 4, \omega_{0,p} = 2.4 \cdot 10^{15}$ s^{-1}, $\gamma_{0,p} = 6.25 \cdot 10^{13}$ s^{-1}, consistent with Ref. [147]). Strong coupling is predicted in both systems at sufficient layer thickness, where the stronger exciton line of WS_2 means that a smaller thickness is required. The J-aggregate system with these parameters suffers from signifant loss (broadening of bands obscures anticrossing). Peculiar to the WS_2 system is the fact that the very large constant background index of the semiconductor significantly changes the mode frequencies even in absence of the excitonic line (due to n_{bg} only). For small thickness the antisymmetric modes (node at the excitonic layer) hardly shift, but the resonance conditions for even ones are dramatically changed. This re-orders the modes at modest thickness (100 nm), and modifies the mode spacing for full filling.

Given that excitonic matter can strongly couple to resonances of metasurface arrays, there is interest in understanding what the optical signatures are when etalons are constructed that contain *both* excitonic media *and* plasmon particle arrays. Bisht et al. [98] recently reported measurements of Rabi splitting in cavities with simultaneously plasmonic and excitonic materials loaded in them, reporting observation of a joint Rabi splitting even exceeding the summed Rabi splitting from just particles, and just excitonic material alone. We present absorption calculations, as absorption partitioned over its plasmonic and excitonic contribution also report on the degree to which each type of polariton contributes to the hybrid plasmonic-excitonic polariton. As parameters we assume a material similar to the J-aggregate (200 nm slab), and a metasurface array with antennas also as before, at a pitch 350 nm. We take the mirrors to be non-absorbing (setting $\epsilon = -22$ for gold purely negative) so that absorption calculations strictly trace plasmonic and excitonic loss channels. Figure 2.12a shows that if the etalon, which we take to have lossless mirrors, is filled with just a plasmon particle array, then absorption as function of frequency and etalon spacing simply traces the dispersion of the anticrossing even etalon modes (mode maximum at the etalon center). The odd modes are absent in absorption, even if they do appear as transmission resonances, as they have an antinode at the absorbing particles. If instead

a slab of excitonic material is placed in the middle of the etalon, both the even and odd modes show in absorption (Fig. 2.12b) since the slab thickness required for strong coupling means that also the anti-symmetric etalon modes have overlap with it. Finally, the absorption spectrum of the joint system is shown in Figure 2.12c. Evidently, the even modes now show a wider anti-crossing than is the case for either excitonic, or plasmonic system alone. This is qualitatively consistent with the experimental report of Bisht [98].

To more quantitatively assess the anticrossing, we examine absorption spectra at the first-order bare-etalon resonant thickness in Figure 2.13, where we furthermore separate out absorption in the metasurface (panel a) and in the excitonic material (panel b). For reference also the absorption is shown for either of the layers alone, in presence and in absence of surrounding mirrors. The absorption spectrum of the individual plasmonic and exitonic layer is a single peak, though not Lorentzian in shape as at the assumed oscillator strength extinction is strong. Upon introduction of the mirrors, the peak in both cases splits, indicating that strong coupling occurs for the case of etalon and metasurface, and for the case of etalon and excitonic material (orange curves). Coincidental to the choice of parameters is that the splitting in both systems is similar in magnitude. In the joint plasmonic-excitonic system the apparent Rabi splitting is larger than in either system separately, but not larger than the sum of Rabi splittings. Moreover, it is noteworthy that in both subsystems the absorption maxima occur at the same frequencies, indicating that these are the eigenfrequencies of the tripartite hybrid modes. A first order approximation to the Rabi splitting $\Omega_{\mathrm{meta+exciton}}$ predicted by

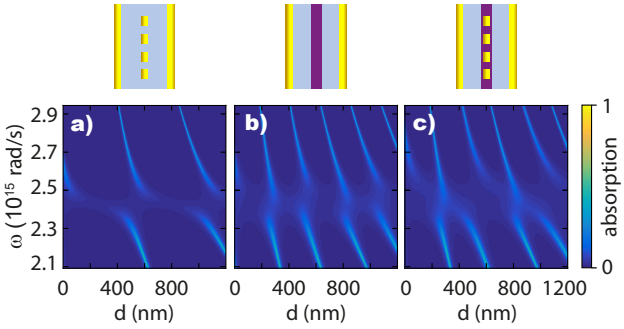

Figure 2.12: Absorption as function of frequency and etalon spacing for etalons in which either a plasmonic metasurface is placed (a, assuming same antennas as in Fig. 2.2-2.5, at pitch 350 nm), or excitonic material (b, a 200 nm thick layer of J-aggregate), or both (c). In the plasmonic case, only the symmetric modes are visible, and show strong coupling. In the tripartite case (c), the Rabi splitting for those modes exceeds that achieved in either a) or b). Note that for this example mirrors were chosen non-absorbing.

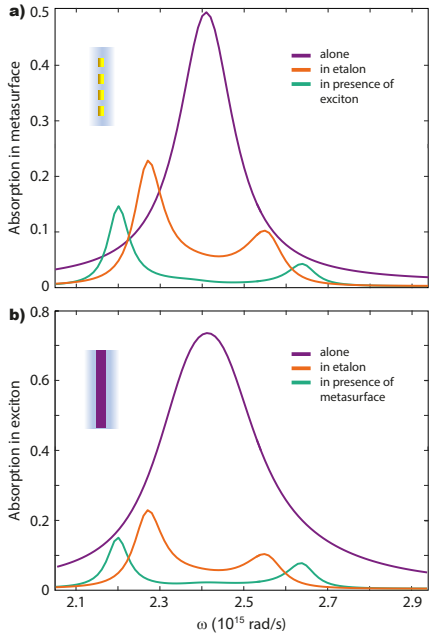

Figure 2.13: Absorption spectra of a) a plasmonic metasurface, resp. b) an excitonic medium (J-aggregate), considering them in isolation (purple curves centered on the resonance $\omega_0 = 2.4 \cdot 10^{15}$ s^{-1}), inserted into an etalon (orange curves), resp. when in the tripartite system of etalon, exciton, and plasmonic metasurface. Parameters are as in Fig. 2.12, with the etalon opening d fixed such that the first order bare etalon resonance is at ω_0.

the membrane-in-the-middel model is

$$\Omega_{\text{meta+exciton}} = \sqrt{\Omega_{\text{meta}}^2 + \Omega_{\text{exciton}}^2} \tag{2.25}$$

in terms of the Rabi splittings Ω_{meta} and Ω_{exciton} of the etalon with just the metasurface alone, and with just the excitonic material. Thus it appears that as reported by Bisht et al. [98] a large Rabi splitting is indeed easier to achieve by combining excitonic and plasmonic constituents in an etalon, even if in distinction to Ref. [98] the joint Rabi splitting can not exceed the sum of Rabi splittings. Unfortunately, this larger splitting would not necessarily be of help for envisioned scenarios in cavity exciton-polariton physics, where one usually seeks to imbue photons with nonlinearities by casting a significant fraction of the excitation into the intrinsically nonlinear exciton. Figure 2.13b reveals that in the tripartite system the absorption in the upper and lower plasmon-exciton-polariton branch is not larger than that in case of the exciton-only etalon. An interesting question outside the scope of our transfer matrix model is in how far near-field enhancement, which is poorly represented in

our model, contributes to further enlarged Rabi splitting and to the fraction of the energy in the hybrid mode that resides in the exciton, as is suggested by the work of Bisht [98].

2.6 Domain of validity and benchmark

While the metasurface multilayer transfer model as we sketched it already applies to many interesting problems, it is important to demarcate its validity and provide a benchmark. The model as we sketched it is specific to normal incidence, and, as it is scalar, does not include polarization effects. This is only a valid approach in case all the plasmon arrays in the stack have the same principal polarization axis, and in case the stack as a whole is interrogated with a polarization coincident with such a principal axis. As we showed for the particular case of the birefringent Salisbury screen, in case the antennas are, for instance, rectangular and aligned with the principal axis of rectangular arrays, one can trivially extend the formalism to deal with polarization-dependent scattering phenomena by decomposing the incident polarization in the two principal polarization components, for which separately the formalism applies. The model can also be easily extended to more complicated scenarios, such as off-normal incidence, metasurfaces with intrinsically magneto-electric or chiral unit cells [62, 64, 171], or when metasurfaces are stacked in a twisted manner. Since one must then account for two polarizations, this requires a 4×4 transfer matrix approach to allow for the polarization cross coupling effects. This would bring the proposed method on par with the S-matrix multilayer approach for metasurface stacks developed by Menzel and Sperrhake et al., who focused specifically on polarimetric applications [154, 155]. A more fundamental limitation of our approach is that it can not deal with propagating and evancescent diffraction orders. This implies, firstly, that grating diffraction phenomena, such as surface lattice resonances and waveguide lattice resonances that are reliant on grating diffraction orders that are propagating in at least one of the layers are beyond the scope of our model. Evanescent diffraction orders are required to describe near- field hybridization effects, which become relevant when particle arrays come to within a fraction of a wavelength ($\sim \lambda/2\pi$) from interfaces or other metasurfaces [136]. Here we discern two distinct cases. First, many metasurface realizations deposit scatterers *on* a dielectric interface, e.g., in air, but on a glass substrate. In this case a practical approach is to model the antennas as being positioned at the location of their center of mass (slightly away from an interface), and adjusting the polarizability V, ω_0 and γ to match full wave calculations. This applies because for moderate index contrasts between either side of the interface, the presence of the interface only slightly renormalizes the polarizability but without changing the resonance character of the antennas. Instead, as a second extreme one could consider the applicability of our model to patch antenna

arrays, i.e., antenna arrays at deep subwavelength separation from metal interfaces. The strong near-field interaction then fundamentally changes the resonance character of the antennas, and the model does not apply. Even within the dipole approximation, our model ignores near-field interactions with interfaces that are encoded in evanescent diffraction orders. In addition near-fields calculated in this model are only of qualitative use, as the model assumes dipolar scatterers instead of the real particle geometry.

To illustrate some of these limitations, Figure 2.14 provides finite element, i.e., full-wave, simulations for select examples from Fig. 2.2 (Salisbury screen) and 2.5 (strong coupling). These calculations use identical parameters for mirrors and glass layers as in the multilayer transfer matrix approach, and as particles assume rectangular nanorods (88 by 40 nm, with a height of 20 nm), and a Drude model for the antenna dielectric constant of the form $\epsilon = \epsilon_b - \omega_p^2/(\omega(\omega + i\gamma))$ with $\epsilon_b = 9.54$, $\omega_p = 1.35 \cdot 10^{16}$ s^{-1} and $\gamma = 9.42 \cdot 10^{13}$ s^{-1}. The particle size was chosen to match the bare lattice response at pitch of 450 nm in COMSOL with that given by Eq (2.14) (resonance frequency, peak reflectivity, transmission and absorption). The benchmark uses symmetry planes to simulate just one quarter of the unit cell, and measures input/output through ports located at either end of the stack (somewhat away from the mirror interfaces). Figure 2.14 shows that the full wave benchmark calculations confirm all our predictions regarding the peculiar amplitude and phase response of Salisbury screens, the appearance and magnitude of strong coupling in etalons, and the progression with antenna density. At the same time the benchmark calculations provide instructive insights in the limitations of the method, where there are three main effects at play. First, the resonance feature slightly blueshift with increasing lattice density, as a consequence of dipole-dipole interactions between antennas (guides to the eye to indicate bare lattice resonance incl. particle interactions indicated by horizontal lines in graphs, labelled "I"). These are in fact contained in the *real part* of the lattice Green function in Eq. (2.14) which renormalizes the real part of the resonance frequency. While for clarity of presentation we set this real part to zero for our illustration examples so as to be able to compare the salient features with strictly aligned resonances, they in fact can be accounted for in lattice sum theory. Second, at distances well below 100 nm between particles and mirror, near-field interactions set in that strongly redshift the antenna resonance frequency (features labelled with letter "II" in graphs). Description of this effect both requires evanescent grating orders that are not contained in our model, and would require to go beyond the dipole approximation. Since neither evanescent grating orders nor microscopic near-field detail is contained in the transfer matrix approach, this highlights a limitation on the domain of validity. Finally, the third effect is that for the lowest antenna density the large pitch allows launching of real grating diffraction into glass, as well as grating-vector assisted coupling into a variety of resonances that include the symmetric and antisymmetric surface plasmon polariton modes supported

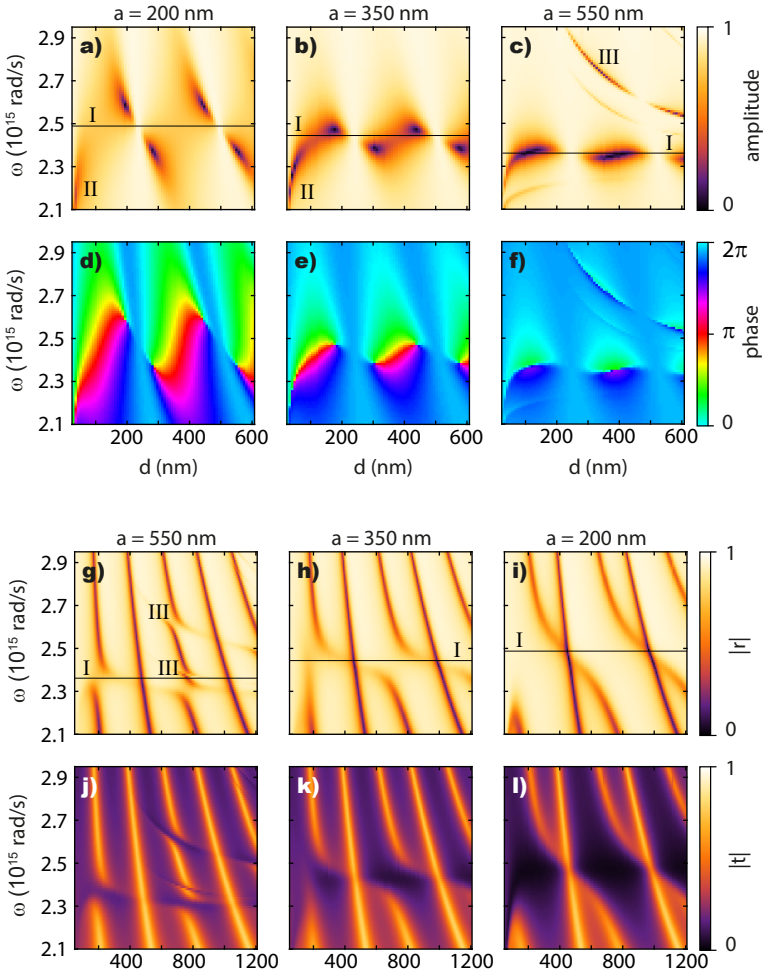

Figure 2.14: COMSOL full wave simulation results to benchmark the transfer matrix model predictions for the Salisbury screen case (panels a-c, reflection amplitude, d-f reflection phase) and strong coupling of etalon resonances with plasmon resonances (panels g-i resp. j-l for reflection resp. transmission amplitude). The x-axes start at 24 nm resp. 48 nm gap for the single-mirror resp. double mirror case. Parameters have been chosen to best compare to Fig. 2.2 resp. Fig. 2.5. Letters "I" indicate the bare lattice resonance frequency, which depends on density. At very small separations to the mirror, the resonances red shift due to near field coupling with the mirror, labelled as "II". At the largest pitches grating wave vector assisted coupling into guided modes and high wave vector etalon resonances can occur at the sharp features labelled as "III". Note that these themselves can show strong coupling with the etalon resonances in panel g).

by the metal mirror, as well as grazing angle etalon resonances in the spacer between mirror and particles. This explains the sharp features that occur for the largest pitch only (labelled with "III" in the graphs). To include such grating diffraction in a dipole antenna scattering model in stratified systems is possible, but far from easy to implement [172].

Finally we note that despite the fact that these are very small COMSOL models (just of order $5{\cdot}10^4$ elements) that take just between 3 and 10 seconds to evaluate (Intel I7-6950X 10 cores, running at 3.3 GHz), the total evaluation time for Fig. 2.14 is of order 18 hours for the Salisbury screen case (leftmost three panels, ca. 6000 parameter combinations per panel), and over three times that for the strong coupling. This should be contrasted to the multilayer approach, where it takes on order of minutes to simulate the bare lattice reflectivity in COMSOL that is input in our model, and which suffices to generate all the graphs.

2.7 Conclusion

To conclude, we have presented a simple yet powerful transfer matrix model for analyzing arbitrary stacks of dielectric and metallic layers combined with metasurfaces that can be inserted in any of the dielectric layers. The power of this approach is that once a library of metasurface reflection and transmission coefficients has been calculated, complex structures can be analyzed easily. We have demonstrated the power of this approach to gain insight into topical nanophotonic problems on basis of three examples. The first is the response of Salisbury screens, i.e., etalons in which one mirror is replaced by a resonant metasurface. The phenomenon of perfect absorption in such Salisbury screens actually has a deeper origin as a topological property in parameter space that is evident as pairs of phase singularities. These singularities in turn imply strong linear dichroism and linear birefringence properties, if one elicits the Salisbury screen response in just one resonant polarization axis. The second example that we analyzed concerns strong coupling between plasmonic metasurfaces and etalon resonances. While scaling laws for the magnitude of the splitting in function of oscillator strength and density are similar to those for classical models of vacuum Rabi splitting in a cavity filled with an excitonic medium, the underlying physics is different. Indeed, in metasurface etalons, the metasurface acts as a dispersive version of the 'membrane in the middle' problem with a strong phase response due to its interface reflectivity and transmission phase, and not due to accumulation of propagation phase. Finally, we have explored the combination of plasmonic and excitonic media in etalons, which provide Rabi splittings beyond the values possible with just either of the constituents.

The model that we proposed extends far beyond the three simple examples that we analyzed. As already foreseen by Menzel and Sperrhake [154, 155] a

rich variety of polarization conversion phenomena with twisted chiral and achiral metasurfaces can be readily analyzed by a simple expansion of our model. Also, one can envision the analysis of stacks of metasurfaces in the context of computational optics, where each metasurface may execute a mathematical function. Of large importance for this agenda is to deal with space-varying amplitude, phase and polarization responses in the plane of each metasurface. In current state of the art metasurface design, space varying metasurfaces are often built using fixed lattice sites, but individually varying scatterers, chosen on basis of library simulations *for purely periodic systems*. For structures discussed here we anticipate that similarly our results apply as a library to construct the space varying response of space-varying metasurfaces if they would be tessellated over tiles over ~ 5 unit cells in size. In how far this approach would hold also for vertically much more extended structures (widely separated layers) is an open question. Our model can also deal with a variety of light-matter interaction scenarios in which stacks of metasurfaces interact with layers of excitonic media, of large interest in the field of collective strong coupling of organic molecules to metasurfaces and etalons. The approach can be easily extended to off-normal propagation and magneto-electric (chiral, non-reciprocal) scattering phenomena, as well as inclusion of gain alongside loss. A drawback of the model is the neglect of grating diffraction orders, both of propagating and evanescent nature. This implies that microscopic details on near-fields and near-field hybridization between very close layers and interfaces are neglected. Nonetheless our model can provide crucial guidance to researchers, helping to delineate which observed phenomena originate truly from hot spots and near-field hybridization effects, and which observed phenomena originate strictly from the zeroth-order phase and amplitude response of metasurfaces, in their multiple scattering interaction with dielectric stacks.

3

Perfect absorption and phase singularities in plasmon antenna array etalons

We present an interferometrically resolved study of the amplitude and phase response of plasmon array etalons composed of a reflective surface with in front of it a metasurface of resonant plasmonic dipole antennas. We find that above a minimum antenna oscillator strength (set by antenna size and density), such structures show conditions of perfect absorption. In the parameter space spanned by frequency and etalon spacing, the singular points unavoidably come in pairs and are associated with a phase singularity. The topologically oppositely charged point pairs occur around the geometric Fabry-Pérot condition. We elucidate the origin of these singularities, and their continuous evolution with oscillator strength in the 2D plane spanned by optical frequency and mirror-antenna spacing. Our findings extend the understanding of Salisbury screens and of 'pixels' in reflective metasurfaces for full control of amplitude and phase. Finally, our data demonstrates the limits of transfer-matrix approaches to predicting the response of arbitray stacks of metasurfaces and dielectric layers.

3.1 Introduction

Resonant metasurfaces are of large interest in the field of electromagnetism, from the radio-frequency domain to nano-optics [112]. While most efforts to utilize metasurfaces as 'flat-optics' wavefront-shapers and holograms focus on transmissive devices, also 'meta-mirrors' are of interest for their tunable response in amplitude, phase, and absorption. A basic reflective geometry is that of a mirror, or ground plane, in front of which a resonantly absorbing and scattering surface is placed, typically in the form of an array of metallic or dielectric antennas with a strong scattering resonance [63, 114, 126–128, 133, 135, 173–178]. Perhaps the best known example of a reflective frequency-selective surface, far predating the field of metasurfaces, is the so-called Salisbury screen in which strong absorption in a thin layer at a quarter wavelength from a mirror can be achieved, even if the layer is by itself only weakly absorbing and not resonant [127, 128]. Salisbury screens with spatially patterned absorbing layers have been studied for applications ranging from RF antireflective technologies [179], to THz and IR radiation detectors, to plasmonic sensors [63, 133, 135, 173–175]. Perfect absorption in materials just in front of a reflector [176–178] has also been linked to *coherent perfect absorption* [180, 181] whereby coherent two-sided illumination of a (partial) absorber can lead to perfect absorption. More recently, reflective metasurfaces have enjoyed new interest owing to the possibility to independently control

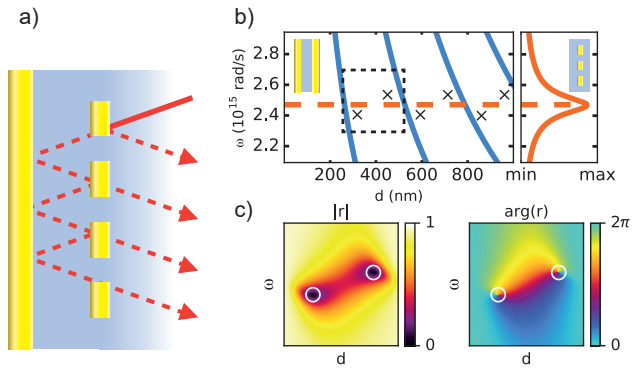

Figure 3.1: a) Schematic of a plasmon array etalon consisting of a mirror and an array of plasmonic antennas. b) Blue: Fabry-Pérot etalon resonance as function of mirror-mirror separation and angular frequency, relevant if the particle array were replaced by a simple mirror. Orange: the resonance of the resonant plasmonic nanorod array in isolation. In the parameter plane spanned by frequency and etalon spacing, plasmon array etalons will feature pairs of points of perfect absorption and phase singularity, as indicated by crosses. c) Calculated response of a plasmon antenna array in amplitude (left) and phase (right) for the dashed region shown in b). Upon hybridization of the Fabry-Pérot modes and the plasmonic resonance a pair of singular points appears (indicated by circles).

the amplitude and phase of reflected light [114, 129, 182], with any phase increment upon reflection within a full 2π interval possible by tuning of the antenna resonance, and antenna-mirror separation. One can distinguish three types of distinct philosophies in design, namely *etalons* where an antenna-mirror spacing on the order of a (quarter) wavelength [130, 131, 133] is used, diffraction based structures, where antennas diffractively couple into surface plasmon guided modes supported by the underlying mirror [183], and gap-antenna based systems as pioneered by Nielsen and Pors et al. [114, 129, 182] where metal nanoparticles are separated by a very narrow gap from a metal plane such that the notion of phase retardation in the gap plays no role. In the context of reflective metasurfaces one envisions that these constructs can act as metasurface pixels that can be assembled to form a full hologram in reflection [184], that can serve as color pixels (acting on amplitude) [137, 185], that perform as polarimetric components, or that can serve as efficient reflectors with controlled phase dispersion, similar to Gires-Tournois mirrors for ultrafast pulse compression.

In this chapter we present a comprehensive study of the amplitude and phase response of reflective resonant metasurface etalons in the near-infrared domain that uncovers several surprising aspects in their physics that have not been hitherto noticed. Figure 3.1a shows a sketch of the basic geometry of such mirror-metasurface etalons, where one reflector is a simple mirror, and the second reflector is a lattice of dipolar nanoantennas. The term 'etalon' delineates that our work neither concerns gap plasmons, nor diffractive coupling, and instead purely hinges on Fabry-Pérot etalon resonances as function of mirror-metamirror spacing (blue curves in Figure 3.1b), the resonant response of the nanoantennas (shown in orange), and the hybridization of these two distinct resonance types (Figure 3.1c). Our amplitude and phase-resolved experiments show that from a minimum antenna oscillator threshold onward, the resulting hybridization gives rise to *pairs* of conditions of zero reflection. This is not foreseen in literature reports on perfect absorption that sofar always reported, or postulated, *single* conditions of zero reflection, for instance arguing that perfect absorption is easily understood from coupled mode theory as a unique critical-coupling condition for absorptive and radiative loss of a resonator [134, 186]. We show that instead in the parameter space spanned by frequency and etalon spacing, (1) the conditions of zero reflection come in pairs, and in fact must unavoidably do so because (2) they are each *necessarily* associated with a phase singularity of opposite topological charge ± 1.

The main questions that our study seeks to address revolve around how such topological points of perfect absorption and phase singularity appear, and how they evolve as a function of resonator density and etalon thickness. A simple model shows that indeed from a minimum density of antennas onwards, points of perfect absorption and phase singularity inevitably appear in pairs. We examine what that entails for the phase response of metasurfaces, following the evolution of the amplitude and phase response as the density of

antennas is increased. The phase singularities in the parameter plane spanned by frequency and etalon spacing do not mean that for any given fixed geometry the observable reflection phase becomes undefined. Instead they serve to show that the phase response swings through a full 2π for each reflectivity spectrum corresponding to any geometry with a thickness *in between* the two distinct thicknesses spanning a pair of singularities. With increasing density the structure essentially evolves from a Gires-Tournois meta-etalon (particles by themselves form a weak reflector) to a Fabry-Pérot etalon (antenna layer alone is strongly reflective). Thus, our work provides a complete mapping of the fundamental tradeoffs in metasurface etalons between absorption, reflection amplitude and phase control. Finally, we also address the domain of validity of Fabry-Pérot models for such systems.

3.2 Theory

In this study we focus on reflective metasurfaces that can essentially be viewed as an etalon consisting of a dielectric spacer of variable thickness d, surrounded by two mirrors, the first of which is a simple gold film, and the second of which is a periodic antenna array (Fig 3.1a). Following Refs. [64, 154] and the detailed overview by Alaee et al. [133], an approximate model for such a stack is to apply the classical two-layer reflectivity model for etalons

$$r = \frac{r_a + r_m(1 + 2r_a)e^{2inkd}}{1 - r_a r_m e^{2inkd}} \tag{3.1}$$

where one inserts for the plasmon antenna array the reflectivity/transmission coefficients (reflectivity r_a) calculated in *absence* of the second interface. Here, $k = \omega/c$ is the wave number of light, n, d are the spacer index and thickness respectively, and r_m denotes the mirror reflection coefficient (which we set to -0.95, corresponding to the reflectivity of a 50 nm gold film). We have already inserted the fact that for 2D lattices of dipole scatterers $t_a = 1 + r_a$, as argued by de Abajo [61, 157]. This model for etalon reflectivity r is approximate if one of the reflectors is a metasurface because it ignores diffraction orders, i.e., both real and evanescent orders that a periodic lattice of scatterers may generate. This distinguishes the physics that enters our model from that studied by [183] (diffractive coupling into surface plasmon polaritons of the mirror), and by Nielsen and Pors et al. (near-field hybridization with the mirror to form gap plasmons) [129, 182].

The reflectivity of a 2D lattice of resonant scatterers in homogeneous space can be approximated using electrodynamic point dipole scattering theory, where all the near- and far-field interactions between antennas are accounted for through Ewald lattice summation [61–64]. According to de Abajo [61], the normal incidence reflection of an antenna array reads (units used as tabulated

in Ref. [171])

$$r_a = \frac{2\pi i k}{a^2} \frac{1}{1/\alpha - \mathcal{G}} \tag{3.2}$$

with α the antenna polarizability, a^2 the unit cell area, and $\mathcal{G}$ a lattice sum accounting for dipole-dipole interactions between antennas. For lattices that are sufficiently densely packed not to have propagating diffraction orders, de Abajo [61] quotes $\mathrm{Im}\ \mathcal{G} = 2\pi k/a^2 - 2/3k^3$, specific for normal incidence (the real part of $\mathcal{G}$ is in our work absorbed into the metasurface resonance frequency). For a resonant antenna array, the antenna polarizability presents a Lorentzian lineshape of the form

$$\alpha = \frac{1}{1/\alpha_0 - i\frac{2}{3}k^3} \quad \alpha_0 = \frac{V\omega_0^2}{\omega_0^2 - \omega^2 - i\omega\gamma} \tag{3.3}$$

where V is the effective scatterer volume, ω_0 the resonance frequency, and γ is the Ohmic damping rate. The radiation damping term [61, 64] that is added to obtain the dynamic polarizability from the static polarizability [171] does not need to be evaluated in practice, owing to the fact that it is exactly cancelled in the imaginary part of the lattice sum $\mathrm{Im}\ \mathcal{G}$. Effectively, in a lattice radiation damping is replaced by a lattice-density dependent superradiant radiative damping, ensuring that the lattice transmission and reflection coefficients remain bounded by energy conservation for all physical choices of α_0.

Figure 3.2a reports the calculated reflectivity in this model for four lattices of antennas increasing in density, in absence of the back reflector. We assume that each antenna has the properties $\omega_0 = 2.4 \cdot 10^{15}$ rad/s, $\gamma = 9.3 \cdot 10^{13}$ rad/s and $V = 6.9 \cdot 10^{-23}$ m^3 such that the extinction cross section on resonance equals $8.8 \cdot 10^{-2} \mu$m^2. These antenna parameters closely match a full wave simulation (COMSOL Multiphysics 5.2) of scattering and extinction cross sections of single antennas to the dipole model. As one would expect, the antenna-arrays show a resonant reflectivity around ω_0, with a strength that increases with density, and a π phase increment when crossing through resonance [62] (Figure 3.2b).

Figure 3.2c displays amplitude and phase of the reflectivity of the plasmon array etalon, predicted using the simple model Eq. (3.1-3.3) for a set of antenna densities (varying pitch), as a function of ω and distance d between antennas and mirror. The pitches used for Figure 3.2c cycle through the canonical cases of low to very high antenna density. For the lowest density, the reflectivity barely shows a phase signature and is essentially that of the back reflector, with pockets of reduced reflection at the antenna resonance frequency only appearing for those separations where the antenna is in an antinode of the 'driving field', i.e., of the field reflected by the back reflector. Conversely, at high densities (pitch 350 and 200 nm), the reflectivity clearly shows points of zero reflection and perfect absorption, which correspond to phase singu-

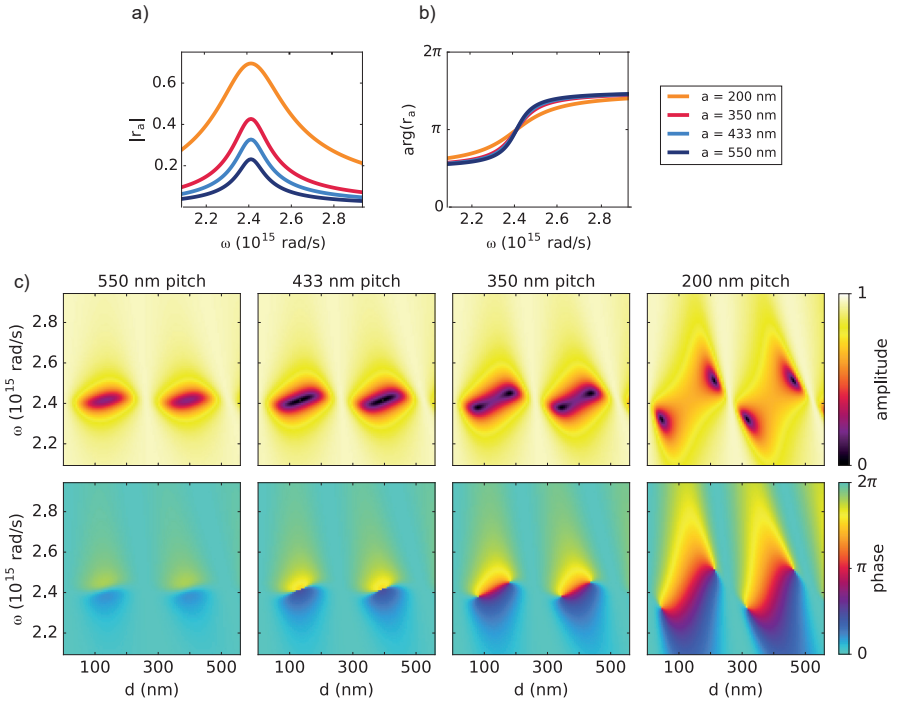

Figure 3.2: a) and b) Amplitude and phase of the reflectivity of a plasmon array (no backing mirror), at different antenna densities (pitch a as indicated), according to Eq. (3.2,3.3). The Lorentzian response strenghtens and broadens (due to superradiant damping) with density, and shows a π-phase jump through resonance. c) Calculated amplitude (top row) and phase (bottom row) of an etalon consisting of a plasmon antenna array and a mirror, as function of optical frequency and etalon spacing, using antenna array pitch as in a,b).

larities. These singularities come in *pairs* of topological charge ± 1, meaning a full 2π phase swing when encircling them. In light of literature this is a surprising result. In some treatments, such as in the very similar dipole modelling approach by Alaee et al [133], this result was not noticed although it may implicitly be part of their reported formalism. Importantly, it is not covered by the commonly accepted coupled-mode theory analysis of perfect absorption by [134, 186], which does report that at a fixed geometry perfect absorption comes with a 2π phase increment in reflectivity, but otherwise *a priori assumes* a single resonance and states that perfect absorption occurs at a unique matching condition for radiative and absorptive loss.

The benefit of considering the 2D plane of frequency versus etalon spacing, and to consider reflection *phase* instead of merely reflectivity amplitude of individual geometries as reported in previous works [133], becomes apparent

when examining the evolution of the *pairs* of points of perfect absorption in it. Apparently, perfect absorption emerges by the creation of phase singularities that topologically must come in pairs of opposite charge. As density is increased, the singularities move away from each other and from the antenna resonance frequency ω_0, towards the lines of near unity reflection. At an intermediate density of 433 nm, the reflection amplitude at minimum is low but never zero, and no phase singularities are apparent. Indeed, a numerical study suggests that this is close to a condition where the pairs of singularities of opposite charge have annihilated each other. In the remainder of this chapter we first experimentally demonstrate that this behavior is real, and then explain the topological origin of the singularity pairs.

3.3 Results

3.3.1 Reflectivity amplitude and phase

We have built an interferometric setup (Figure 3.3a) to measure the amplitude and phase response of micro/nanostructures using femtosecond pulse interferometry, inspired by a design by Kop et al. [187] that we adapted to a common-path layout, and that uses tunable femtosecond pulses from a Light Conversion Orpheus-F OPA. operated at 1 MHz repetition rate. As metasurface we use gold nanorods fabricated on a flat glass substrate in square arrays of various pitches made by e-beam lithography. An SEM image of the resulting rods is shown in Figure 3.3b, taken before completing the etalons with a dielectric spacer and backreflector. To realize etalons, we evaporated a staircase of SiO_x giving access to thicknesses from 60 to 540 nm in 17 nm steps, on top of which we evaporated a homogeneous 50 nm gold layer as back reflector (providing an r_m of -0.95). Figure 3.3c shows an optical microscope image of the nanoantenna fields, viewed from the backside of the sample. Due to interference, the varying antenna-mirror spacing gives rise to a range of colors. We refer to the Methods section for an explanation of our protocol to obtain signal and reference measurements in interferometry.

Figure 3.4a shows reflection measurements for four different pitches. We first examine the data set with an antenna pitch of 350 nm, which classifies as moderately strong scattering. The reflection amplitude colormap as function of angular frequency and etalon spacing shows near unit reflection, except in pockets of spectral width 10^{14} rad/s around $\omega = 2.5 \cdot 10^{15}$ rad/s (750 nm wavelength). This wavelength and bandwidth correspond to the resonance band of the bare antenna array (the measured reflection of a bare antenna array at 200 nm pitch is 740 nm). The alternating bands of near-unit reflection at d around 270 and 520 nm and pockets of strongly reduced reflection correspond to sweeping through the Fabry-Pérot resonance and anti-resonance conditions, respectively. The measured phase response reveals pairs of phase

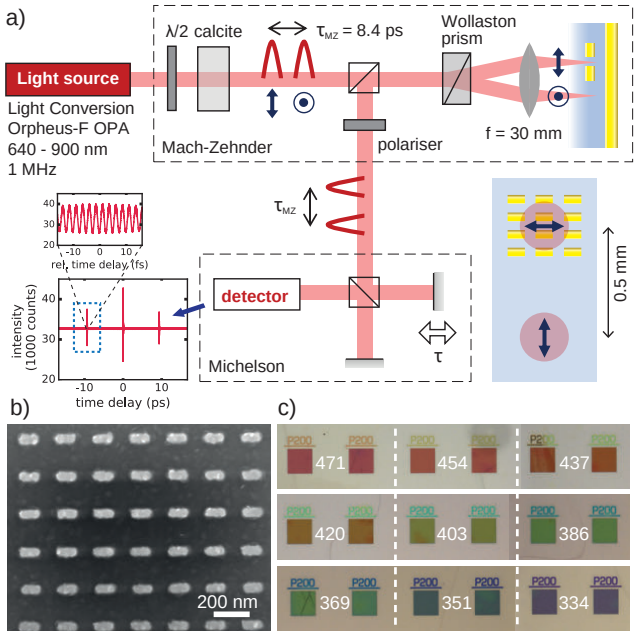

Figure 3.3: a) Schematic of the setup. Femtosecond pulse pairs split temporally exit from a calcite prism into a common-path Mach-Zehnder interferometer (Wollaston prism acts as beam splitter). Reflected sample and reference are correlated by the Michelson interferometer. In the interferogram (inset left), the blue dashed region marks the left cross correlation. On the sample (inset right), each plasmon array is accompanied by an unpatterned region 500 μm downwards, for the reference beam. b) Scanning electron micrograph of a plasmon antenna array. c) Optical micrographs of 200 nm pitch arrays, for various etalon spacings (white text, in nm). The dielectric spacer is stepped (edges marked by dashed lines), each step spanning two arrays.

singularities for each pocket of low reflection. Tracing a loop around each of two nearby singularities results in a total accumulated phase of $+2\pi$ or -2π, indicative of opposite topological charge. Cross cuts in reflection amplitude and phase versus frequency at select thicknesses further highlight the presence of singularities (Figure 3.4c). On either side of a *pair* of singularities, the data (red and yellow curves) show a deep but nonetheless non-zero reflection dip with just small phase signatures. The cross cut closest to the singularity at $d = 365$ nm (blue) shows an overall 2π phase change over the spectrum. Right at a singularity the reflection must vanish completely, although for practical reasons one would not expect to be able to hit the *exact* singularity at any finite sampling of thickness and frequency. Actually measured reflectivity amplitudes closest to the phase singularities are as low as $9 \cdot 10^{-3}$ (i.e. 10^{-4} in intensity reflectivity). Fabricating smaller increments in d would allow to measure even smaller values.

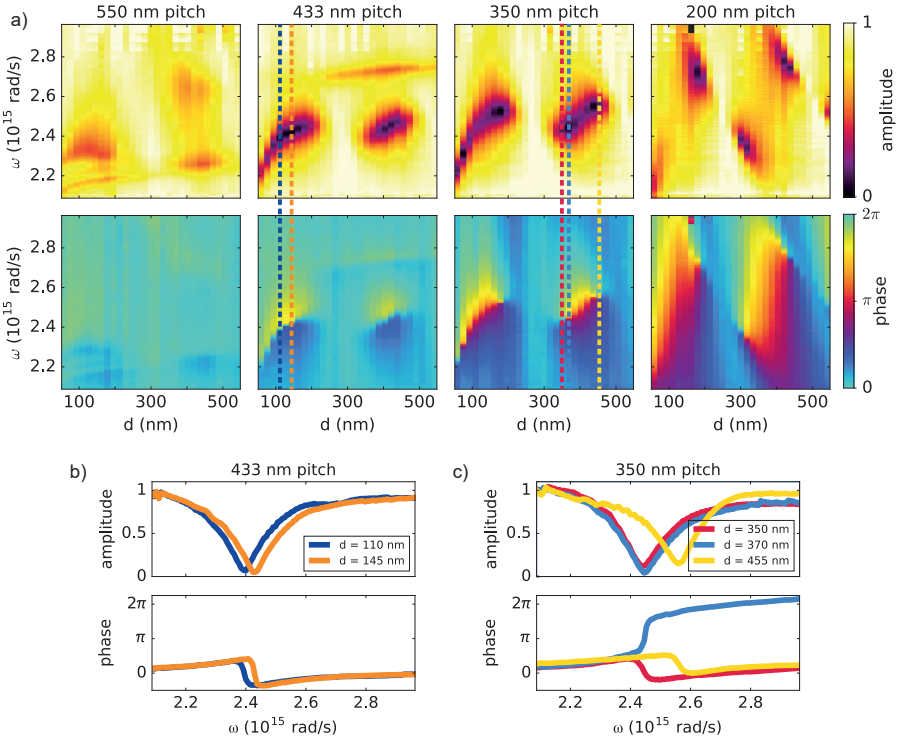

Figure 3.4: a) Measured amplitude (top row) and phase (bottom row) as function of optical frequency and etalon spacing, for plasmon antenna array etalons of pitch decreasing from 550 nm to 200 nm as indicated. From 350 nm onwards, phase singularities and perfect absorption occur. b,c) Crosscuts at fixed etalon spacing (as indicated by dashed vertical lines in a), showing reflection amplitude and phase versus frequency for 433 and 350 nm pitch.

The data set at pitch 350 nm is very similar to the simple model in Figure 3.2c at the same pitch, highlighting the applicability of our simple etalon analysis. A remarkable deviation occurs at the smallest lattice-mirror separations, where the reflection band red-shifts significantly with vanishing separation owing to near-field coupling between atennas and mirror (further discussed below). To evidence the appearance and evolution of the singularities versus oscillator strength, Figure 3.4a reports data for a range of samples both more dilute and more dense than the 350 nm pitch. For the very dilute lattice, no phase singularities occur, and the reflection amplitude is only moderately modulated. Evidently the 550 nm pitch is below the threshold for phase singularity pairs and perfect absorption. For 433 nm, the sample is quite close to the threshold for appearance of phase singularities, showing the apparent "blue-yellow" discontinuity but no full 2π phase sweep, matching

the calculation in Figure 3.2c. Measured reflectivity minima are as deep as $3 \cdot 10^{-2}$ in intensity, but there are evidently no true zeros as there are no resolved phase singularities. Figure 3.4b shows cross cuts through the data at fixed spacing and as function of frequency (dark blue and orange), which distinctly show no evidence for the 2π-phase sweep seen in the data at pitch 350 nm. On the opposite side of the threshold, i.e., pitch 350 nm and above, the reflection shows pairs of singularities of opposite topological charge, coinciding with measured $|r| < 1 \cdot 10^{-4}$ (for the case of 200 nm pitch). At the largest particle density the singularities clearly move from the band of the bare antenna resonance, to the hyperbolas of fixed kd-values that set the Fabry-Pérot interference condition. All these observations are consistent with the progression evident in the simple Fabry-Pérot model that we plotted in Figure 3.2.

3.3.2 Topological origin of the singularities

Returning to the Fabry-Pérot model, it is immediately evident that a mirror-metasurface etalon will attain exactly zero reflection, and hence perfect absorption, when the numerator of Eq. (3.1) crosses zero. This requires the condition [157]:

$$r_m e^{2inkd} = \frac{-r_a}{(1+2r_a)}. \tag{3.4}$$

A graphical solution for the case at hand is very insightful (Figure 3.5). For non-absorbing spacers, the lefthand side of Eq. (3.4) circumscribes a full circle in the complex plane of radius r_m around the origin (gray dashed), each time that one sweeps the product of (optical) spacing nd and wavenumber k a full 2π (assuming nondispersive mirror reflectivity r_m). On the other hand, the right hand side of Eq. (3.4) as function of frequency traces out a curve in the complex plane that for a Lorentzian antenna model (Eq. (3.3), same antenna properties as used in Figure 3.2) happens to also be a circle (colored lines). However, this circle is displaced exactly by its radius along the real axis, and can have essentially any radius, increasing with the oscillator strength per unit area. As the oscillator strength is increased and the peak antenna reflectivity goes through $r_a = -1/2$, the radius goes through infinity, after which the circumscribed circle shrinks again in radius, now in the opposite part of the complex plane (negative real part).

The topology of the problem in the complex plane immediately shows a number of salient features. First, there are no solutions for a zero in etalon reflection below a minimum antenna oscillator strength (blue curves in Figure 3.5), as the circular locus traversed by $-r_a/(1+2r_a)$ is too small to cross $|r_m|$. Second, above this minimum the equality always has a *pair* of solutions, i.e., there are two distinct values for e^{2inkd} at which reflection vanishes. Hence reflection zeroes will always come in pairs, with pairs repeating at half-integer wavelength spacing between layers. The resulting absolute zeroes in

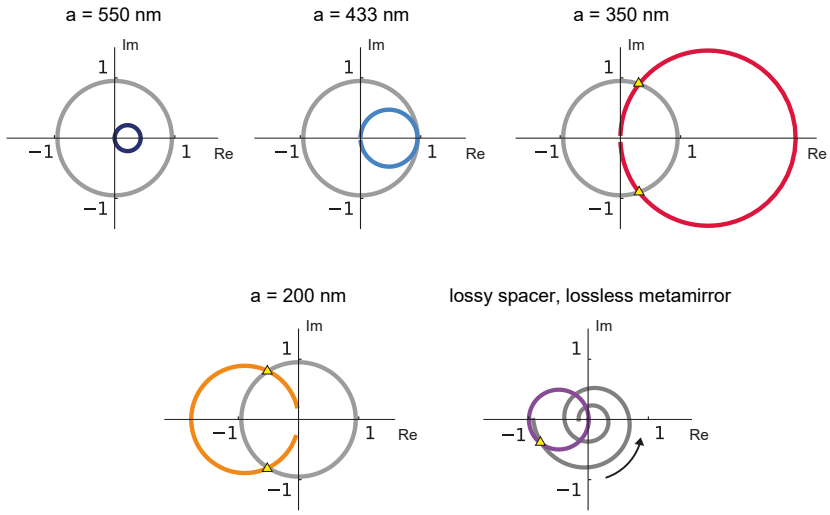

Figure 3.5: Graphical construction of Eq. (3.4) in the complex plane, plotting the trajectories that the left hand and right hand side sweep through as function of frequency, for lattices ranging from dilute to dense, matching our experiment. In each diagram, the gray circle is $r_m e^{iknd}$ (back mirror and spacer), while the colored circles represent the trajectory of $-r_a/(1+2r_a)$. Intersection points (marked) correspond to the solutions of Eq. (3.4): zero reflection and phase singularities necessarily come in pairs, as soon as the array reflectivity exceeds a threshold strength (radius of the colored circles). The rightmost diagram is for a case not studied in our experiment, but common in literature [130, 186]: when the spacer absorbs, the term $r_m e^{2iknd}$ becomes a counterclockwise turning, shrinking, spiral. When the metasurface mirror is itself non-absorbing, the curve $-r_a/(1+2r_a)$ has radius $1/2$, and is centered at $-1/2+0i$. There is automatically one first intersection close to the metasurface resonance frequency.

reflectivity are each associated with a phase singularity of opposite charge. We attribute this to the analytical properties of the reflectivity specified by Eq. (3.1), which is a complex valued analytical function of ω, and all geometrical parameters, and to the fact that the intersections in Figure 3.5 correspond to first-order zeroes, except in the case of $a = 350$ nm (touching circles). A fourth prediction that is evident from Figure 3.5 by tracing the location of the intersection points is that when the zeros just appear (oscillator strength just above threshold), they will do so close to the reflection resonance of the bare particle array. For increasing oscillator strength, the zeros shift towards $r_m e^{2inkd} = \pm i$, or equivalently towards the Fabry-Pérot resonance condition ($e^{2inkd} = 1$ for near-unit efficiency mirrors). Both the Fabry-Pérot calculations in Figure 3.5, and the experimental datasets in Figure 3.4c illustrate exactly these scenarios: going from no intersection at low density, via the point of touching at intermediate pitch of 433 nm, to the regimes of intersection at moderate and strong oscillator strength. Commensurate with the discussion

of Figure 3.5, only the cases of intersecting circles show perfect absorption, with concomitant pairs of phase singularities. The transition from pitch 433 nm to 350 nm documents the birth of two oppositely charged singularities. Here it should be noted that our experiment does not visualize the very first singularity, not just because our sample does not afford access to sufficiently thin spacers, but also because physics *beyond* the Fabry-Pérot model shifts the first singularity to the red of our laser range.

In the literature on perfect absorption a very well-known viewpoint is that it can be described as critical coupling of a single-mode resonator to the far-field by matching of loss and damping rates [130, 186]. To connect to this viewpoint, we observe that the critical coupling formula for a single resonance with a single input/output port has as an essential property that the real-frequency zero in the scattering matrix or response function at critical coupling is associated to a nearby pole in the complex frequency plane, where the real part of the frequency is that of the perfect absorption condition. The etalon response function encoded in Eq. (3.1-3.3) evaluated at thicknesses where perfect absorption occurs also carries complex-frequency plane poles at frequencies near to the zero in the scattering matrix. This highlights that the metasurface etalons realize the physics reported by Solli et al. and Asano et al [188, 189], with the associated implications of parameter-space singularities and perfect-absorption points on anomalous dispersion properties. At the same time it should be noted that the literature critical coupling conditions arguments [130, 186] in essence *postulate* a single resonance with its resonance frequency and damping rate, without any predictive power to decide on the existence or number of these poles or their parameters on basis of the constituents of the etalon, as opposed to the analysis in this work. Effectively, the single-mode critical-coupling model can parametrize [by fitting parameters], but not predict, the perfect absorption and phase response spectra. This parametrization is only valid close to singular points: actual reflectivity spectra (vertical cuts in our calculated diagrams) can be distinctly non-Lorentzian, meaning that the single-pole approximation of [130, 186] does not apply. Finally we note that in the literature on perfect absorption, some reports actually deal with *absorbing spacers* captured in the index n surrounded by non-absorbing reflectors, as opposed to the case of a non-absorbing spacer, yet absorption in the sheet quantified by r_a (see [130, 186]). To deal with this case, one should consider that now the left hand side of Eq. (3.4) turns from a circle into a spiral that for a near-lossless back reflector starts close to $r_m = -1$ and then turns clockwise and shrinks to the origin with increasing kd. If the metasurface reflector is itself lossless, the conditions $t_a = 1 + r_a$ together with $|t_a|^2 + |r_a|^2 = 1$ constrain its reflectivity r_a, and coincidentally also $-r_a/(1 + 2r_a)$ to a circle of radius exactly $1/2$, centered at $-1/2 + 0i$ in the complex plane. In this topologically different scenario, if the metasurface has a resonance (at resonance automatically $r_a = -1$), there is automatically a *single*, first crossing with the spiral, i.e., a *single* thickness for perfect absorption

occurs, at a frequency close to the resonance. This single first resonance is the case studied in Ref. [186] and Ref. [130]. Just increasing thickness from this first perfect absorption condition onwards, while remaining at the same frequency, will not reveal further conditions of perfect absorption unlike the case of a lossless spacer. However, there is a further infinite series of pairs of singularities, with frequency detuning steadily increasing with spacer thickness (within the assumption of a non-dispersive refractive index).

3.3.3 Beyond the Fabry-Pérot model

Finally we turn to the differences between our experimental results and the simple Fabry-Pérot model. First, near-field coupling between the antennas and the mirror substrate causes a significant resonance redshift at small separations for each of the antenna arrays, and hence also for the collective response. This is especially clear for the intermediate densities (433 and 350 nm). This effect was predicted to occur in this context by Kwadrin et al. [64]. To describe the redshift, a model that includes near-field coupling to the mirror is required. One viewpoint is that in this regime one enters the regime of gap plasmons studied by Pors et al. [129], where it is more fruitful to solve for the antenna-mirror system as a resonator, instead of applying a Fabry-Pérot model. Another viewpoint is appropriate for the description of stacked (meta)surfaces as multilayers. For standard multilayers, transfer matrix/S-matrix methods are robust because the interface reflection constants apply at any spacing to adjacent layers, owing to the fact that they follow directly from boundary conditions on parallel field components of $\mathbf{E}, \mathbf{H}$. Instead, metasurfaces are only effectively homogeneizable, but not actually homogeneous. At small spacings, the antennas hybridize with their own mirror image. This 'backaction' effect is mediated by near-fields, i.e., by evanescent lattice diffraction orders that are not contained in Eq. (3.1,3.2), and that would only be accounted for if the layer S-matrix method that gave rise to Eq. (3.1) were expanded to a full Fourier modal method. This observation essentially impacts any effort to design multilayer stacks of metasurfaces, as is pursued, for instance, for analog processing of images [123] and metasurface polarimetry [154]. Clearly, standard transfer matrix approaches to construct the response of a stack out of the response of constituents only holds if (meta)surfaces are widely spaced (in excess of $\sim \lambda/2\pi$).

A second and distinct deviation between our data and the simple Fabry-Pérot interference model is that for larger pitches diffractive coupling can occur into grazing angle grating diffraction orders in the glass, or possibly surface plasmon polariton (SPP) waveguiding modes, at least for sufficiently small wavelengths and large pitches [61]. These features require grating-assisted parallel momentum matching of incident light to the glass/SPP and would hence occur in the measured reflectivity diagrams as horizontal lines, sharply defined in frequency and not (strongly) dependent on spacer thick-

ness. This corresponds to the scenario considered by Christ et al. [183]. For diffraction into a waveguide mode, or into a grazing grating diffraction order, of a given effective index n_{eff}, diffractive coupling from normal incidence occurs at $\lambda = n_{\text{eff}}a$, with a the lattice pitch. For the densest lattice no diffraction condition can be met. However, diffractive coupling is clearly evident for pitches 433 nm and 550 nm, through dark, narrow and near-horizontal features of reduced specular reflectivity near 680 nm resp. 860 nm ($2.77 \cdot 10^{15}$ rad/s resp. $2.19 \cdot 10^{15}$ rad/s). We observe apparent indices of around 1.57, exceeding the index of the glass substrate and cover layer. Furthermore, the diffraction features are not quite horizontal but disperse slightly with mirror-particle spacing, indicating that the relevant effective index n_{eff} varies somewhat with spacer thickness at small separations. This points to the fact that the grating incoupling is into a surface plasmon polariton mode (since the index exceeds that of the dielectric layers) that is a hybrid between the surface plasmon polariton of a flat glass-gold interface and the particles, as evidenced by the separation dependence of n_{eff}. At the largest pitch, the diffraction condition overlaps partially with the particle resonance, leading to a more complicated response. Indeed, overlapping particle and diffraction responses can give rise to intricate Fano-type lineshapes, as is well-studied in the field of surface lattice resonances and waveguide plasmon-polaritons [190].

3.4 Discussion

To summarize, we have reported the amplitude and phase response of metasurface etalons of which the backreflector is an unstructured mirror, and the other is a resonant antenna array. Our theoretical and experimental results both show that from a minimum threshold oscillator strength density, controllable via antenna density and cross section, *pairs of points* of perfect absorption necessarily appear in the parameter space spanned by frequency and mirror-antenna separation space. Furthermore, these points are necessarily associated with pairs of phase singularities of charge ± 1. As the antenna oscillator strength and density are increased, the singular points move away from the bare antenna resonance, and from the condition that the antenna must be in the antinode of the backreflector standing wave, and shift towards the Fabry-Pérot conditions of a standard mirror-sandwich. The singularities in parameter space directly imply for the response of any fixed geometry that meets a condition of perfect absorption that the concomitant reflection spectrum will have a phase that is never singular, but will show a full 2π phase increment.

Our work has several interesting repercussions. It provides a deeper understanding of the general design rules for reflective metasurface 'pixels' for reflection amplitude and phase control. The presence of the singular points means that reflection amplitude over a large range down to true zero is possi-

ble, and reflection phases over the entirety of 0 to 2π. For the given material system, reflectivity of $> 50\%$ can be maintained at any desired phase, using the densest lattices. In our work, the rod-shaped antennas imply phase control for just one linear polarization channel, meaning that these reflective metasurfaces will also allow polarimetric operations such as polarization-selective absorption and retardation. Furthermore, several authors have previously suggested that sensing schemes could benefit from working around phase singularities in parameter spaces, i.e., around points of zero reflection [132, 191–194]. In the systems considered here the phase singularities are dependent on one hand on the product nkd (giving sensitivity to frequency, and etalon refractive index and spacing), and to r_a on the other hand (sensitivity to antenna resonance). Finally we note that the *deviations* between the simple etalon model and the data at small mirror-metasurface separation also point to interesting aspects of designing *stacked* metasurfaces, as is pursued for metasurface polarimetry, as well as for analog computing with metasurfaces [123, 154], where one would hope to concatenate functions by stacking surfaces. Transfer matrix theory will only predict the response of closely-spaced stacked metasurfaces if one keeps track of evanescent diffracted orders.

3.5 Supplementary information

3.5.1 Interferometry setup

We implemented an interferometric setup to measure the amplitude and phase response of micro/nanostructures due to the design by Kop et al. [187], adapted to a common-path layout. The principle is that the sample is placed in one arm of a Mach-Zehnder interferometer which is fed by a femtosecond pulse train. The second arm provides a reference path with a fixed, non-zero time delay that well exceeds the pulse duration. This ensures that at the output of the interferometer, the sum $E_r(t+\tau_{MZ}) + E_s(t)$ of two temporally separated pulses emerge, one of which has travelled through the reference arm and was delayed by an amount τ_{MZ}, and the other one of which has interacted with the sample. Next, this double-pulse train is fed into a scanning Michelson interferometer, to record an interferogram $I(\tau)$ as a function of time delay τ, i.e.

$$\int |(E_r(t+\tau_{MZ}) + E_s(t)) + (E_r(t+\tau_{MZ}+\tau) + E_s(t+\tau))|^2 dt \tag{3.5}$$

As argued by Kop et al. [187], the interferogram will show around its zero delay the sum of the field-field autocorrelations of the sample and reference pulse, while at scan delays near $\pm\tau_{MZ}$, cross-correlations of the reference and sample pulse appear. This allows to retrieve back the complex-valued sample transfer function $H(\omega)$ since

$$\mathcal{F}I_{CC}(\tau) \propto H(\omega)|E_r(\omega)|^2 e^{i\omega\tau_{\mathrm{MZ}}}. \tag{3.6}$$

The input pulse spectrum $|E_r(\omega)|^2$ can be retrieved either from the autocorrelation (blocking the sample arm), or from a reference measurement on a reference sample with $H(\omega) = 1$.

Figure 3.3a shows the realization of this principle in our work, where the difference with Kop et al. [187] is that we have built the Mach-Zehnder interferometer in an almost entirely common path layout, so that reference and sample beam both pass through the same optics, arriving at only slightly offset locations on the sample. To arrange this, we follow a design by van Dijk [195]. The femtosecond pulse train of a Light Conversion ORPHEUS-F OPA at 1 MHz is polarized at 45 degrees relative to the lab frame (taking 0 degrees to be vertically polarized), and then fed through a birefringent calcite block of 15 mm length. This results in two orthogonally polarized (horizontal and vertical) pulses at a fixed temporal delay of 8.4 ps, travelling along the same optical axis. Next, these beams are split in a 1 degree angle by a Wollaston prism. Upon focusing with a lens or microscope objective, this means that two foci arise, offset in time by 8.4 ps, as well as being offset in space. In our setup we use a simple focusing lens (f = 30 mm, achromat), resulting in a spatial

separation of 500 μm. Our setup can be operated both in reflection and in transmission, by ensuring that the collection path follows an identical geometry to the excitation path. In this work we focus on reflection, in which case we simply use the fact that after passing through the same Wollaston prism the reflected pulses are collinear again. We split off the reflected light using a beam splitter between Wollaston prism and calcite, and project the orthogonally polarized reference and sample pulses on the same polarization axis using a polarization analyzer at 45 degrees to the lab frame. This is the point of recombination of pulses in the Mach-Zehnder interferometer. Next, the co-polarized and collinear pulse pair is fed into a Thorlabs OSA202C spectrum-analyzer, which is in fact a scanning Michelson interferometer. We read out interferograms as shown in Figure 3.3a inset, clipping out cross-correlates as shown. In this work we reference the measurement to measurements with $H(\omega) = 1$ (nominally), simply by displacing the sample to a measurement region with no plasmon antennas, i.e. with only the reflector.

3.5.2 Sample

As metasurface we use gold nanorods fabricated on a flat glass substrate in square arrays of various pitches made by e-beam lithography. We use a multi-stack for lift-off, consisting of an e-beam resist (top layer, thin for resolution), a thin germanium layer and a thicker bottom spacer layer that generates the undercut and thickness needed for lift off. The germanium serves as an etch mask for the spacer. The fabrication procedure is as follows: we spincoat 100 nm PMMA 495-A8 on cleaned glass slides (base piranha) followed by evaporation of 20 nm germanium. We then spincoat 50 nm of CSAR AR-P 6200:09 as e-beam resist. Exposure of the sample is done in a Voyager e-beam system (Raith, 50 keV). The nanorod size (100 by 50 nm) is chosen to obtain a resonance in our lasing tuning window. We fabricate four different pitches, from dilute (550 nm) to dense (200 nm), as limited by the desire to avoid grating diffractions. We write 100 x 100 μm sized fields in rows with a spacing of 150 μm between the fields. This is chosen to accomodate a staircase of controlled glass thickness to be evaporated over the field to ultimately create etalons. After exposure we develop the resist in pentyl acetate for 60 s. Next, the germanium is plasma etched in a 1:5 O_2:SF_6 mixture for 60 s, and PMMA is isotropically etched in an O_2 plasma. Finally we evaporate 40 nm gold and perform liftoff in 45°C acetone.

To obtain etalons of controlled spacing we evaporate SiO_x using e-beam evaporation (Polyteknik Flextura M508 E). A linear shutter is used to realise a staircase of increasing thickness ranging from 60 to 540 nm in steps of 17 nm, with each step spaced by 500 μm. Irrespective of the exact alignment of the staircase relative to the fields, this ensures that we obtain all lattice-height combinations. As a final step, the sample is covered with 50 nm gold as back reflector (providing an r_m of -0.95).

3.5.3 Measurement protocol

Our optical measurement protocol consists of a sample and reference measurement at every spacer thickness d, and runs through the following steps. First we focus our sample beam on a nanorod field, with the nanorods' long axis aligned with the polarisation of the sample beam (90 degrees with respect to the lab frame, i.e. horizontally polarized). The orientation of the Wollaston prism dictates where the focus of the reference beam is positioned. In this work, the reference focus is vertically offset from the sample beam by 500 μm. Our sample design ensures that it lands on the back mirror of the etalon, and at the same spacer thickness d (see right inset in Figure 3.3a). To span the spectrum from 640 to 900 nm (exceeding the 12 nm spectrum of our pulses), we take data at a sequence of pulse central frequencies. Subsequently we perform a sequence of reference measurements after vertically shifting the sample to have both beams focusing on the mirror. Repeating this sequence for each spacer separation leads to the complex reflection r versus d and ω.

4

Strong coupling to generate complex birefringence - metasurface in the middle etalons

We have measured the optical signatures of strong coupling between the resonance of etalons and plasmon antenna arrays in transmission and polarization. Planar etalons in the middle of which a plasmon antenna array is placed show anticrossings in transmission between the etalon resonances and plasmon antenna resonance, which we map as function of frequency, etalon opening and oscillator strengh. We argue that the proper interpretation of strong coupling and the magnitude of the Rabi splitting requires a 'metasurface-in-the-middle' cavity model, and is distinct from strong coupling between a cavity and a dispersive material. Furthermore, we quantitatively connect the Rabi splitting to the electrostatic antenna polarizability, i.e., the polarizability in absence of radiative damping corrections. Finally, we demonstrate that the strong coupling brings very strong polarization conversion effects, as the hybrid modes provide for a strong retardance that can be leveraged for linear birefringence and dichroism.

4.1 Introduction

Strong coupling of classical as well as quantum resonances is a seminal textbook problem in physics, both as an undergraduate illustration of coupled oscillator physics, and as foundation for schemes to control, e.g., the flow of energy and coherence between degrees of freedom [145, 146, 166, 196, 197]. In nanophotonics there is a large interest in eliciting coupled oscillator signatures in the scattering response of dielectric and plasmonic systems [158, 198]. Hallmark examples are Fano-resonant plasmonic oligomers [198], exceptional points [199], and hybrid dielectric-plasmonic resonators [21, 78, 87, 89, 90]. A main motivation for these efforts is to gain control over confinement on one hand, and over linewidth on the other hand, that is not available with the constituent individual resonators alone. Thus Fano resonances in coupled resonant photonic systems have been proposed for applications in refractive index sensing [89], infrared vibrational spectroscopy [200], and local density of states control that enables potentially microcavity Q with plasmonic confinement [21, 78, 87, 201]. Furthermore, strong coupling of optical resonances with material resonances is also of large current interest, for instance to hybridize photons with excitons, phonons, and molecular vibrations [73, 144–146, 148, 150, 156, 161, 162, 202, 203]. This domain seeks to imbue light with nonlinear properties through those of matter, and conversely to control photophysical, electronic, and chemical processes in matter by controlling the mode structure of the photon field.

In this chapter we experimentally address strong coupling of etalon resonances with inserted lattices of plasmon antennas, a scenario first proposed

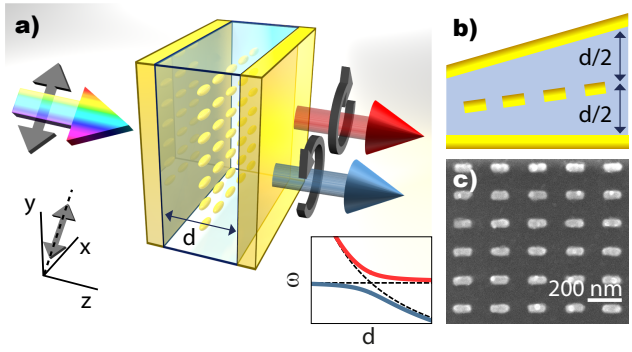

Figure 4.1: a) Sketch of a Fabry-Pérot cavity filled with resonant metallic nanorods. Strong coupling causes anti-crossing of the lattice and etalon resonances in the ω,d plane (inset). The two branches appear with very strong circular polarization conversion. b) Sketch of the wedge-shaped sample (height variation of order 1 μm over lateral distance of several millimeters. c) SEM image of Au nanorods (200 nm pitch lattice along x as example - for all samples the pitch along y is reduced by factor 0.75 compared to pitch in x), before completion of the sample.

by Ameling *et al*. [94–97] as 'microcavity plasmonics' (system as sketched in Fig. 4.1a). In these pioneering works the authors showed that full wave numerical simulations display avoided crossings in the etalon response that can be effectively parametrized by a coupled oscillator Hamiltonian, and they reported spectroscopy for select geometries [94–97]. This system has recently regained attention as a system in which to pursue strong coupling of light with matter, since Bisht *et al*. [98] claimed that when excitonic material is placed right at the antennas, Rabi splitting in transmission exceeds that achievable with the plasmon and excitonic material alone. In this light a more precise understanding of the relation between geometry and anticrossing, i.e., between antenna polarizability, and magnitude of the anticrossing, is called for. In this work we experimentally survey the parameter phase space of frequency and etalon spacing while systematically varying the antenna lattice oscillator strength, by varying the lattice density. Thereby we elucidate the emergence of anticrossing, providing a more microscopically motivated viewpoint than that provided by fitting full wave simulations to an ad hoc Hamiltonian of coupled mode theory. Next we examine polarimetric signatures of the strong coupling in our systems. We have studied microcavity plasmonics on basis of nanorods that provide a resonance, and hence strong coupling, only along one polarization axis. Thereby the microcavity-plasmon etalons display a very strong linear dichroism and polarization-dependent retardance. This complex birefringence expresses as very distinctive strong linear and circular polarization conversion signatures for strong coupling.

4.2 Strong coupling transmission experiment

Figure 4.1 demonstrates the experimental system. The etalon in this work consists of two planar Au mirrors of 20 nm thickness separated by a variable thickness d of evaporated SiO_x (380 - 1300 nm) deposited in an evaporator with a continuously moving shutter (Fig. 4.1b, wedge of micrometer height extending over millimeters). The etalon is chosen such that we can study the lowest order modes (up to order 7), while providing a Q of order 100. Centered between the mirrors we place scattering Au nanoantenna arrays that are fabricated by electron-beam lithography and lift off after depositing the first mirror and half of the spacer. An SEM image is shown in Fig. 4.1c. The antennas are fabricated with dimensions around 100×50 nm so as to have a resonance around 700 nm (see section 4.6.1). We fabricated lattices of antennas with varying density, so that thereby the oscillator strength per unit area that is loaded into to the cavity to induce normal mode splitting is systematically varied. We label arrays by their pitch along the long axis. Along their short axis the pitch is slightly smaller (factor 0.75) to raise the packing density.

The gentle slope of the wedged spacer ensures that we can measure transmission as function of etalon spacing in transmission simply by displacing

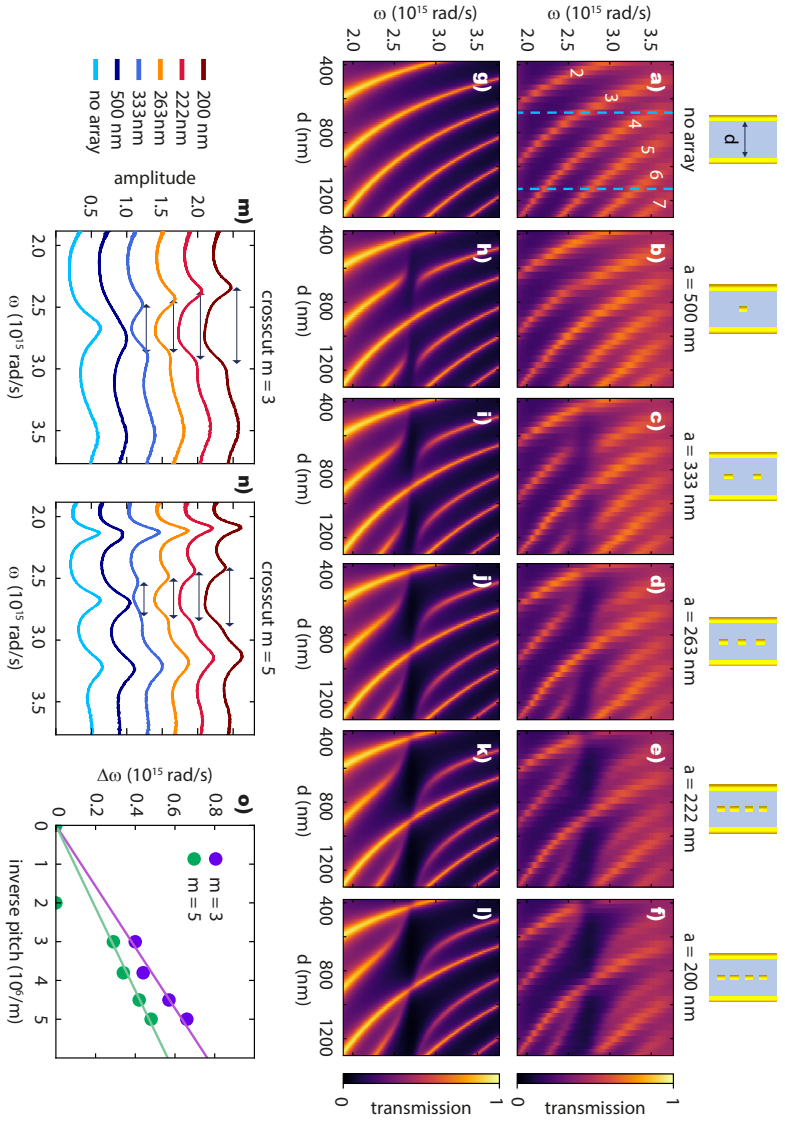

Figure 4.2: a-f) Transmission through planar Fabry-Pérot cavity-antenna hybrids as a function of etalon thickness and frequency. a) Empty cavity, b-f) the antenna array scattering strength is increased from pitch 500 to 333, 263, 222 and 200 nm. Panels g-l) show the corresponding calculated transmission from a simple transfer matrix model. m) and n) Transmission versus frequency at 665 nm and 1110 nm etalon width, corresponding to the bare etalon 3rd and 5th mode. Curves at increasing antenna density are offset vertically. o) Rabi splitting versus inverse lattice pitch for etalon mode 3 and 5.

the wedge through a $\sim$ 50 μm collection area. We employ a simple white light normal incidence transmission spectroscopy set up with a fibercoupled grating spectrometer [204]. Figure 4.2a-f shows transmission plots of these cavity-antenna hybrids as function of cavity length d and frequency ω, with the incoming polarization aligned to the resonant, i.e., long, antenna axis (horizontal polarization), and no polarization analysis in the detection path. Transmission spectra are taken at etalon thicknesses d in steps of approx. 22 nm. Fig. 4.2a plots the transmission in absence of a perturbation, and simply displays the well known Fabry-Pérot transmission peaks at frequencies for which the etalon length matches the cavity resonance conditions. White numbers denote mode order, and blue lines mark the thicknesses at which crosscuts are shown in Fig. 4.2m,n. Figures 4.2b-f plot transmission in presence of the scattering antenna array of pitch a decreasing from 500, 333, 263, 222 to 200, i.e., arranged in order of increasing density and hence weak to strong perturbation. At 500 nm density only a mild reduction of transmission at the etalon transmission maxima occurs that is barely observable for frequencies around the plasmon resonance. At 333 nm pitch the odd resonance orders (mode orders m clarified using white labels in Fig. 4.2a) show a distinct disappearance of the transmission maxima. At pitches from 263 nm and lower, the appearance of an anticrossing is evident for the odd modes, while the even modes are left unaffected. Qualitatively this data confirms the expectation due to Ameling *et al*. [96] that once the scattering strength of the arrays reaches a certain threshold, strong coupling sets in. The case of 333 nm pitch (Fig. 4.2c) is clearly at or above this threshold. Since the plasmonic particles reside in the center of the etalon, they are at a node of the *even* etalon modes, which are hence left unaffected. Conversely, the odd modes have excellent field overlap with the antennas. Qualitatively, increasing the array density (Fig. 4.2d-f) makes the splitting more pronounced, while conversely the Rabi splitting decreases with mode order. This is consistent with the qualitative expectation that Rabi splitting scales with the square root of oscillator strenght and inverse cavity length. While this behavior was observed also in full wave simulations by Ameling *et al*. [96], the systematic progression has not been mapped experimentally before.

The figure of merit for the strength of coupling is the magnitude of the anticrossing, or Rabi splitting [145, 146, 166]. As a first-order quantification we obtain Rabi splitting from spectra at resonant etalon thicknesses. We determine the etalon thickness at which the bare etalons have their resonance at the bare antenna array resonance (ca. 710 nm vacuum wavelength in this work) and report the spectral dependence of transmission at these thicknesses for the 3rd and 5th mode order in Fig. 4.2m and n, curves vertically offset for clarity. Spectra show the expected distinct evolution from a single transmission maximum to a split doublet. At the very high and low end of the frequency spectrum, furthermore peaks appear that correspond to higher resp. lower mode orders, while for the bluest wavelengths the contrast generally deterio-

rates due to increased material absorption in the gold mirrors and antennas. Nonetheless, the Rabi splitting can be readily extracted. We find values of order $\Delta\lambda = 180$ nm, or equivalently $\hbar\Delta\omega = 400$ meV in the densest lattices and for the lowest order (3rd) mode.

4.3 Metasurface-in-the-middle model

It is very tempting to interpret the plasmonic signature in transmission as the classical anticrossing one gets in an etalon filled with an atomic gas with a dispersive polarizability, as described in the seminal paper by Zhu *et al*. [144]. In fact the physics for metasurface etalons is quite different. This is easily seen by examining a so-called 'membrane in the middle' model for etalons in which a partial reflector is introduced in the middle, as discussed by Jayich *et al*. [167, 205] in the context of cavity optomechanics. For a planar reflector of amplitude reflection r_a and transmission $t_a = 1 + r_a$ centrally placed in an etalon of width d and identical mirror response (reflection and transmission r resp. t), the transmission reads

$$t_{\text{stack}} = \frac{(r_a + 1)t^2 e^{ikd}}{1 - r^2(2r_a + 1)e^{2ikd} - 2rr_a e^{ikd}}. \tag{4.1}$$

with $k = \omega/cn(\omega)$ the wavenumber in the medium inside the cavity at frequency ω. The textbook case of classical strong coupling in a cavity completely filled with an atomic gas [144] has no middle reflector ($r_a = 0$) and a dispersive phase accumulation $\phi = 2\omega/cn(\omega)d$ provided through the frequency-dependent gas refractive index $n(\omega) = 1 + \frac{1}{2}\rho\alpha$ (ρ the density and α atomic polarizability). This dispersive phase accumulation causes the resonance condition (minimum in the denominator $\mathcal{L}$ of Eq. (4.1), found by Ref. [144] by assessing when the *argument* of $\mathcal{L} + 1$ equals an odd-integer multiple of π) to be achieved twice for a given mode order. These two conditions are spaced in frequency by the Rabi splitting. Instead for a plasmon array as reflector, there is no propagation delay that enters through e^{iknd} as the entire effect of the antennas is contained in the dispersive metasurface reflection and transmission coefficient r_a resp. $t_a = 1 + r_a$. This is an important difference: for the densest lattices in our work, the bare lattice reflectivity exceeds 50%, indicating that strong coupling indeed is associated not with a propagation delay n, but with a dispersive impedance in the system.

The metasurface reflection in a semi-analytical coupled dipole approximation for infinite lattices of scatterers reads [61, 136]

$$r_a = \frac{2\pi ik}{\mathcal{A}}\alpha_{\text{latt}} = \frac{2\pi ik}{\mathcal{A}}\frac{1}{1/\alpha_{\text{stat}} - \mathcal{G}} \tag{4.2}$$

where $\mathcal{A}$ is the unit cell area, $\mathcal{G}$ is an Ewald lattice-summation accounting for all dipole-dipole interactions, α_{stat} is an electrostatic antenna polarizability. As

unit definition, we use $\mathbf{p} = 4\pi\epsilon\alpha\mathbf{E}$ (with ϵ the host medium permittivity) so that α has units of volume. Importantly, there are three polarizabilities overall that one can distinguish for a scatterer. First, the electrostatic polarizability is a purely mathematical construct that in the limit of, e.g., small spheres follows from Rayleigh's approximation in terms of just scatterer volume and dielectric constant. This is not actually an observable, since inserting it in literature expressions for extinction and scattering cross sections of a single antenna shows violation of energy conservation. In those observables instead the electrodynamic polarizability $\alpha_{\text{dyn}} = (\alpha_{\text{stat}}^{-1} - i\frac{2}{3}k^3)^{-1}$ appears, which follows from the static one by addition of dynamic corrections (radiation damping). This is the polarizability that can be retrieved from full wave simulations and extinction measurements, through $\sigma_{\text{ext}} = 4\pi k\text{Im}\alpha$. Finally, in a lattice the radiation damping term $\frac{2}{3}k^3$ is replaced by $\mathcal{G}$, giving the lattice polarizability α_{lat}. For non-diffractive lattices, $\text{Im}\mathcal{G} = \frac{2\pi ik}{\mathcal{A}}$. The interpretation is that superradiant damping ensures that the reflectivity remains below unity in magnitude.

Figures 4.2g-l report calculations using a transfer matrix model that slightly improves upon the simple metasurface-in-the-middle model by taking the finite thickness of the mirrors into account [205]. The model accurately reproduces all features of the experiment. We use as electrostatic polarizability a Lorentzian model $\alpha_{\text{stat}} = \omega_0^2 V/(\omega_0^2 - \omega^2 - i\omega\gamma)$ with $\omega_0 = 2.7 \cdot 10^{15}$ s^{-1} the bare lattice resonance frequency, $\gamma = 9.5 \cdot 10^{13}$ s^{-1} the Ohmic loss rate of the metal composing the antennas. Finally, $V = 4.2 \cdot 10^{-23}$ m^3 is an effective scatterer volume, quantifying the single antenna oscillator strength that is comparable to its physical volume (discussed extensively below). The parameters are matched to simulated metasurface transmission in absence of the etalon mirrors. The mirrors are chosen as 20 nm thick Au reflectors ($n = 0.25 + 4.5i$, chosen dispersionless). Overall, the model reproduces all salient features of the data, with the noted difference that the model material constants underestimate the increased damping of gold towards higher frequency (most notably this prevents strong coupling in data at pitch $a = 500$ nm).

The Rabi splitting in the metasurface-in-the-middle model in the limit of small r_a as [205] can be found by mirroring the analysis strategy of Zhu et al. [144], analysing when the *argument* $\mathcal{L} + 1$ equals an odd-integer multiple of π. We find

$$\omega_{\pm} = \omega_0 \left(1 \pm \sqrt{\frac{2\pi V}{\mathcal{A}d}}\right). \tag{4.3}$$

We have verified numerically that Eq. (4.3) describes the splitting also for large r_a, i.e., if very dense and highly reflective antenna arrays are assumed in the membrane-in-the-middle model. The splitting is in form very similar to that derived for cavities filled with an atomic gas, which scales as the square root of the product of atomic oscillator strength and density. This is remarkable, given that the oscillator now appears through r_a and not through n. The

inverse dependence of the splitting with $\sqrt{\mathcal{A}d}$ is clearly evident in the splittings extracted from the data (splitting determined at $d = 665$ nm for mode 3, and $d = 1110$ nm for mode 5), plotted versus inverse pitch in Fig. 4.2o. Fitting straight lines through the origin to the observed splittings, we find the slopes for mode 3 and 5 to stand in the ratio 1.35, in reasonable accord with the expected $\sqrt{5/3} \sim 1.29$, or equivalently the difference in d.

A very peculiar aspect of the predicted Rabi splitting in Eq. (4.3) is that it *only* depends on the effective scatterer volume V, in essence a purely *electrostatic* characteristic of the antenna. None of the 'dynamic' polarizability corrections in either α_{dyn} or α_{latt} appear in the splitting despite fully accounting for dynamic effects in its derivation (telltale signature is the absence of terms involving the speed of light c in Eq. (4.3)). This distinction is actually significant in this work. The slopes of the linear fits in Fig. 4.2o translate to an effective scatterer volume $V \approx (4.2 \pm 0.2) \cdot 10^{-23}$ m^3. This number is in remarkable accordance with the physical particle volume of $100 \times 50 \times 40$ nm^3 $= 5 \cdot 10^{-22}$ m^3 if one recognizes that one should expect V to differ by a factor $\sim 3/4\pi \approx 0.24$ from physical volume (Fröhlich model for a Drude model plasmonic nanosphere). This volume implies a concomitant *on-resonance quasistatic polarizability* $\alpha_{\text{stat}} = (\omega_0/\gamma V) \approx 1.3 \cdot 10^{-21}$ m^3. This far exceeds the *dynamic* polarizability attainable for a single dipole scatterer (strictly bounded by radiation damping to $\alpha_{\text{dyn}} \leq (\frac{2}{3}k^3)^{-1} \approx 6 \cdot 10^{-22}$ m^3 on resonance), and even more so that attainable in a lattice ($\alpha_{\text{latt}} \leq \mathcal{A}/(2\pi k) \approx 4.6 \cdot 10^{-22}$ m^3 to avoid reflectivity exceeding unity). A related surprise is in stock when checking if the strong coupling condition is met on basis of damping rates and Rabi splitting. The loss of a plasmon antenna array is the sum of Ohmic loss ($Q \approx 30$) and radiative loss that increases strongly with antenna scattering strength and array density due to collective superradiant damping. For instance, at 200 nm pitch, the FWHM of the bare array reflectivity corresponds to a $Q < 5$ (evaluated from Eq. (4.2)). One should then conclude that strong coupling is hardly attainable since the Rabi splitting in Fig. 4.2o corresponds to $\Delta\omega/\omega = 0.24$. Instead, the observed anticrossing is very well resolved in Figure 4.2f, and evidently it is the quasistatic $Q \sim 30$ that is relevant. The observation that the electrostatic polarizability with no dynamic corrections matters for Rabi splitting is highly peculiar, since it is not an observable in any measurement that measures scattering strength, e.g. through extinction. This underlines the caution with which one should approach predicting Rabi splittings from full wave numerical simulations or measurements: inverting measured extinction into α, and subsequently into an apparent scattered volume for insertion in Eq. (4.3) through $V \approx \gamma/\omega_0(\sigma_{\text{ext}}/(4\pi k)$ one would obtain a dramatic underestimate of the Rabi splitting. To rationalize our peculiar finding we note that even if *on-resonance* polarizabilities are strongly reduced by dynamic corrections [$\alpha_{\text{latt}}(\omega_0) \ll \alpha_{\text{stat}}(\omega_0)$], in fact the correction is small $\alpha_{\text{latt}}(\omega_\pm) \approx \alpha_{\text{stat}}(\omega_\pm)$ at the normal mode frequencies $\omega_\pm$.

4.4 Polarimetric signature

The nanorod antennas used in this work only have a resonant response along x for the wavelengths considered in this work. Thus the antenna-etalons display strong coupling for x-polarization, but the response for y-polarized input light is essentially that of an empty etalon. This anisotropy causes very distinct polarization signatures in transmission when illuminating the etalons with any polarization that contains both x and y contributions. The root cause is that strong coupling in the x-polarized channels carries not only a distinct amplitude response, but also a distinct phase. Figure 4.3a,b report the calculated phase in transmission for the etalon in y-polarization (calculated as etalon with no nanorods), and the etalon in x-polarization respectively. The phase reference is the front facet of the etalon, meaning that the equivalent homogeneous space would show a phase linearly incrementing as nkd (not shown here). The bare etalon instead has a flat response punctuated by jumps by π at each resonance. The etalon with plasmons finally has for every odd mode a distinct S shape in the phase response, due to the dispersive lattice reflectivity. The *phase difference* between bare and filled etalon brings out as a phase signature the anticrossing bands (Figure 4.3c). We argue that polarimetry can reveal exactly this *phase difference* between x and y transmission coefficient. Figure 4.3d illustrates precisely this scenario as expressed in the *polarization ellipticity* ε of transmitted light predicted for 45° linear input polarization (ellipticity defined as ratio of minor to major axis of polarization ellipse, with sign coding for handedness). The ellipticity is predicted to directly reveal the anticrossing bands. One interpretation is that by coming in at 45° linear polarization and performing polarimetry one in essence uses the

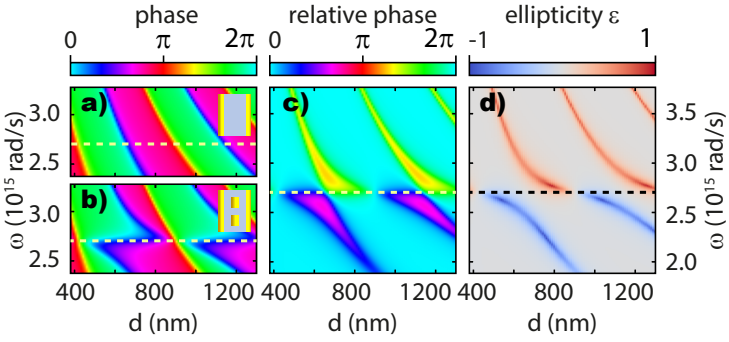

Figure 4.3: a) Calculated transmission phase through an empty cavity, as function of cavity thickness d and frequency ω (etalon front facet as phase reference). Note a cropped frequency axis. b) Case a) but with 200 nm pitch nanorod array. c) Phase difference between a) and b), revealing the relative phase between x and y polarized transmitted light. d) Polarization ellipticity for transmitted light upon diagonally linearly polarized input. The phase difference translates into polarization ellipticity.

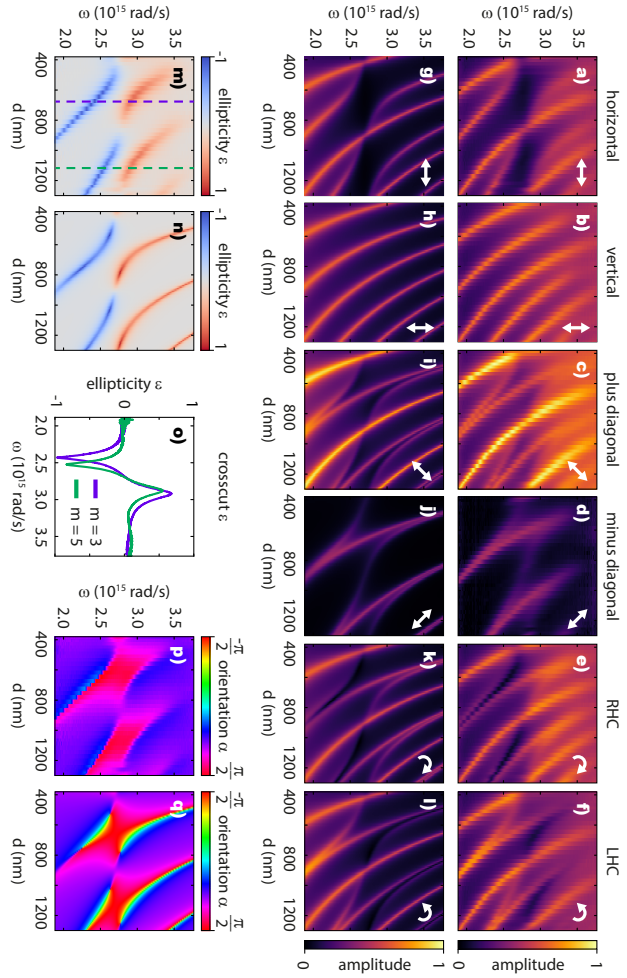

Figure 4.4: a-f) Transmission through the planar Fabry-Pérot cavity-antenna hybrid shown in Fig. 4.2f (pitch 200 nm), for six different detection polarization channels, with identical diagonal input polarization P. Color plots show spectra taken at a range of etalon spacings d, at approx. 22 nm increments. a) Detection aligned with the antenna resonance axis, reporting strong coupling. b) Detection perpendicular to the antenna long axis, returning bare Fabry-Pérot lines. c) Linear diagonal polarization P along the input polarization. d) The crosspolarization channel M is nonzero, a clear sign of polarization conversion. e and f) Circular right- and lefthanded polarization. g-l) Calculated response of the system. m,n) Measurement and calculation of the polarization ellipticity ϵ, retrieved from the six polarization measurements. o) Crosscuts through ϵ at the third and fifth cavity mode. p,q) Experimental and theoretical orientation of the polarization ellipse long axis α.

y-polarized channel as reference beam against which to perform interferometry and measure the phase imparted by the strong coupling in the x-channel. An equivalent viewpoint is that the microcavity plasmonic structure is a multilayer metasurface stack that shows distinct linear dichroism and birefringence particularly at the anticrossing hybrid modes.

We have observed the predicted complex birefringence in full Stokes polarimetry measurements, coming in at diagonal $\pm 45^\circ$ linear polarization and collecting transmitted intensity normalized to the overall lamp spectrum in the linear horizontal, vertical, diagonal and antidiagonal channels, as well as the right and left handed circular polarization channel (T_H, T_V, T_P, T_M resp. T_R and T_L, see section 4.6.3 and Ref. [206]). The measurements require distinct care in cancelling out residual birefringence of lenses, and polarization selectivity of the fiber-coupled spectrometer for which we refer to section 4.6.2. Figure 4.4a-f show for $+45^\circ$ input polarization the transmission in the detection channels. We take from Fig. 4.2 the case in which splitting is the most pronounced (panel f, 200 nm pitch). For horizontal polarization detection the measurement simply replicates that of Fig. 4.2f, but at half the amplitude since only half the input is in the strong coupling polarization channel. For vertical, i.e. y-polarized, detection (Fig. 4.4b) we observe the signature of a bare etalon, as the x-oriented antennas have essentially no response when driven along their short axis. The P polarized transmission (diagonal, along the input) is qualitatively much like the sum of H and V, so that etalon mode 2 and mode 4, which are decoupled from the plasmons and hence appear in both H and V, appear twice brighter than the odd modes. Peculiar is the appearance of light in the cross-polarized diagonal channel, pointing directly at significant polarization rotation. Calculations using our metasurface-in-the-middle approach confirm all observed features.

Through Stokes formalism (see section 4.6.3) we extract the *polarization ellipticity* ε and the polarization ellipse orientation α, which together quantify the full transmitted polarization ellipse. The ellipticity directly brings out the peculiar phase response associated to strong coupling. Generally throughout parameter space and away from the hybrid plasmon-etalon mode the input linear polarization remains largely linear (white shading in Figure 4.4m), though with rotations in the polarization *angle* shown in Figure 4.4p (blue indicates orientation unchanged from incoming polarization at $+45^\circ$, i.e. $\pi/4$). This is commensurate with the fact that the x and y-polarized transmission generally have different magnitude but identical phase. However, right at the hybrid modes the polarization signature is very different, with strong conversion from the input linear polarization to circular output. The helicity is of opposite sign for the upper and lower branch. The strong ellipticity signatures appear *only* for the perturbed modes ($m = 3$ and $m = 5$). Crosscuts through the ellipticity landscape (Figure 4.4o) show that the hybrid mode is revealed with large contrast, which is advantageous for extracting the Rabi splitting when comparing to, e.g., just the transmission of horizontally polarized light

in Fig. 4.2f. All features in intensity and polarization are well reproduced in a simple model that simply evaluates the appropriate polarization projections from a linear superposition of the x- and y-polarized transmission (Eq. (4.1) respectively with and without r_a, Fig. 4.4g-l for transmission in each polarization channel, panels n and q for polarization ellipticity and ellipse orientation).

4.5 Conclusion

In summary, we have reported the experimental signature of strong coupling between etalon resonances and those of embedded resonant metasurfaces in transmission and in polarimetry. While superficially similar to the classical strong coupling between planar cavities in dispersive matter, in fact the strong coupling has quite a different origin: it does not originate from phase pickup upon traversing the length of a medium with dispersive refractive index, but instead maps onto a 'metasurface-in-the-middle' cavity model with a strong, resonant reflection response. Rabi splitting is customarily anticipated to scale with the square root of the *on-resonance* polarizability. Peculiar is that it is the *electrostatic* antenna polarizability that enters the scaling, which is not an observable in any known measurement or full-wave calculation of scattering strength. This is of high relevance for large splittings, since the electrostatic polarizability can far exceed the electrodynamic one, and is also relevant for the bare-resonator Q to which the Rabi splitting should be compared. These conclusions are of large relevance for the quantitative study and optimization of strong coupling between light and matter, as facilitated by hybrid photonic-plasmonic structures. Finally, the plasmon array etalons show a very strong linear birefringence and dichroism. On one hand this provides a new modality for evidencing strong coupling in experiments. On the other hand it may have implications for metasurfaces aimed at realizing complex birefringence for amplitude, polarization and phase control of light. We furthermore note that linear birefringence in microcavities can give rise to eigenmodes with singular chiral properties that correspond to Voigt exceptional points [207]. These appear at off-normal incidence as polarimetric singularity at select frequencies and parallel momenta set by the eigenmode dispersion. The cavities that we studied could provide an exquisite platform to engineer such singularities.

4.6 Supplementary information

4.6.1 Sample fabrication

As etalons we use a planar Au - SiO_x - nanorod array - SiO_x - Au layer structure fabricated on a glass substrate (or: mirror - spacer - metamirror - spacer - mirror). A crucial step in this process is to have tight control over the thickness of the deposited spacer layers. These two SiO_x layers are deposited in a wedge shape, with their thickness increasing in the same x-direction, in order to realise the desired range of etalon spacing (380 - 1300 nm) while keeping the nanorods centered in the cavity. Nanorod arrays are fabricated by electron beam lithography over a rectangular writefield that stretches the entire spacer wedge using e-beam lithography. Five different pitches are fabricated offset in y-direction.

The fabrication procedure is as follows. After cleaning the glass substrate, a 3 nm Cr adhesion layer is deposited, followed by a 20 nm Au layer. This constitutes the first etalon mirror. Next, the application of a thin layer of ORMOCOMP (approx. 20 nm) is found to be critical to reduce stress in the subsequently deposited spacer layer. Thermal evaporation of SiO_x is done using a linear shutter to realize a wedge of increasing thickness ranging from about 150 to 610 nm. Next, nanorods are fabricated using electron beam lithography, for which we use a stack that has ca. 100 nm PMMA 495-A8 covered with a $\sim$20 nm Ge etch mask and finally ca. 50 nm of CSAR AR-P 6200:09 as actual resist. We use Raith Voyager 50 keV e-beam lithography system to expose the CSAR, and after development etch through the Ge (1:5 O_2:SF_6 plasma etch), and subsequently isotropically etch the PMMA. Finally we evaporate gold and perform lift-off in acetone to obtain rectangular arrays (y-pitch 0.75 times pitch along x, the long antenna axis) of nanorods, ca. $100 \times 50 \times 40$ nm in size. Despite our efforts, a small systematic variation of antenna size with dose remains (smaller size at larger pitch). The second layer of SiO_x is applied in the same way as the first layer, now aiming at a wedge of 210 to 670 nm thickness to compensate for both the ORMOCOMP in the bottom layer and the thickness of the antennas. As a last step, the cavity is completed by evaporating the final 20 nm Au mirror. The intermediate and final spacer thickness profiles are inspected by (mechanical) profilometry, and in the final measurements cavity length is calibrated by fitting a Fabry-Pérot response to empty cavity transmission spectra. Evaporation of Cr, Au and SiO_x (outer mirrors and spacers) is performed in a thermal evaporation system (Polyteknik Flextura M508 E). For the nanorods a homebuild thermal evaporator was used, however similar quality antennas have been achieved using the Flextura system.

4.6.2 Setup

To measure transmission spectra we use a simple setup reported in [204] in which light from a fiber coupled halogen lamp (Avalight, Avantes) is collimated and subsequently focused on the sample by an $f = 30$ mm lens. On the transmitted side, light is recollimated by an identical lens, relayed through polarization analysis optics, and finally coupled into an Avantes grating spectrometer. The detection area is approximately 50 μm across on the sample. A challenge in such a set up is to get consistent polarimetry results as there are minor birefringence effects in achromatic lenses, and since the fiber-coupled grating spectrometer presents a polarization-selective responsivity. In this work we first pass the light through a fixed horizontal linear polarizer, and subsequently set the incident polarizer by a second polarizer in diagonal/anti-diagonal orientation. This ensures that the input spectrum is identical for both input polarization settings. Polarimetry on the output is performed using a broadband quarter wave plate and linear polarizer (wave plate Thorlabs AQWP05M-600, all linear polarizers Thorlabs LPVIS100-MP2, setting sequence as in [206]).

4.6.3 Polarimetry

To deal with the slight polarization selectivity of the detector, we obtain the transmission coefficients for the 6 detection channels from measurements through plain glass as follows (superscript indicates incident polarization, subscript output selector setting):

$$T^{P,M}_{H,V,R,L} = 0.5 \cdot I^{P,M}_{\text{sample},H,V,R,L} / I^{P,M}_{\text{glass},H,V,R,L}$$

for the 4 channels neither coincident with nor crossed to the input,

$$T^{P,M}_{P,M} = I^{P,M}_{\text{sample},P,M} / I^{P,M}_{\text{glass},P,M}$$

for the channel coincident with the input, and finally

$$T^{P,M}_{M,P} = I^{P,M}_{\text{sample},M,P} / (\langle I_{\text{glass}} \rangle - 0.5 \cdot I^{P,M}_{\text{glass},P,M}).$$

Here we have used the fact that despite the slight polarization selectivity in the detection the *sum* over orthoganal channels is to a few percent identical for whichever orthogonal polarization combination is chosen ($H+V$, $R+L$, or $P+M$). This sum is indicated as $\langle I_{\text{glass}} \rangle$. We have verified that for the bare etalon this gives the expected response (i.e., no cross polarization generated) and that our measurements are consistent when swapping the input polarization from diagonal to anti-diagonal. Polarizations are defined as $H = x, V = y$, $P, M = \frac{1}{\sqrt{2}}(x \pm y)$, $R, L = \frac{1}{\sqrt{2}}(x \pm iy)$ with x horizontal, y vertical, and $x \times y$ pointing from light source to detector.

The six polarized transmission measurements redundantly encode the four Stokes parameters as $S_0 = T_H + T_V$, $S_1 = T_H - T_V$, $S_2 = T_P - T_M$ and $S_3 = T_R - T_L$ which allow to reconstruct the full polarization ellipse. Ellipticity is defined as the ratio of minor to major axis of the polarization ellipse and is calculated as $\varepsilon = S_3/(\sqrt{S_1^2 + S_2^2 + S_3^2} + \sqrt{S_1^2 + S_2^2})$. ϵ takes values -1 or $+1$ for entirely left-handed (LHC) resp. right-handed (RHC) circulary polarized light, and equals 0 for linear polarization. The polarization orientation is specified by the angle $\alpha = \frac{1}{2}\text{arg}(S_1 + S_2)$ from polarization ellipse major axis to x-axis, with values from $-\pi/2$ tot $\pi/2$ and 0 encoding for horizontal orientation.

5

Nonlinear interferometric autocorrelation for plasmonic time dynamics retrieval

Temporal dynamics of plasmonic-photonic hybrid resonances are an important parameter for the understanding of light-matter interaction at the nanocale. While far-field measurements, as demonstrated in the previous chapters, yield spectral transmission and reflection profiles/maps and in principle offer some insight in resonance decay time through linewidths, the far-field gives no information on the magnitude and spatial distribution of the local field enhancement. Such quantities can only be probed locally. In this chapter we demonstrate a fully common path setup for interferometric autocorrelations in the focus of an objective. After characterizing our femtosecond pulse system we present preliminary results using two-photon excited luminescence emitted by quantum dots in the near field of Ag nanoparticles.

5.1 Introduction

Confining light to the tiniest length scales is a fascinating field that is widely studied, as it allows to dramatically enhance light-matter interaction [208], paving the way towards applications such as nano lasers [18], surface enhanced Raman spectroscopy [209, 210], biomedical diagnostics [5], photo thermal therapy [6], bio imaging [211, 212] and sensing [51]. Plasmonic nanoparticles are particularly suited for such confinement, due to their inherent ability to host localized surface plasmons [208, 213]. In addition, metal nanoparticles are very useful as probes of the local electromagnetic field, given their nonlinear response that arises from the large local field enhancement, combined with the intrinsic nonlinear response of metals [214, 215]. Nonlinear two-photon luminescence spectroscopy is for example applied to quantify accumulated Au nanoparticles in cells in tissue [216]. Second harmonic spectroscopy has been used to characterize for example the response of split ring resonator arrays, surface lattice resonances and even hybrid plasmonic-dielectric nanontennas [110, 111, 217]. Nanoparticle second harmonic and third harmonic, as well as two-photon excited luminescence signal can reach substantial count rates under suitable excitation (ultrashort pulses, high repetition rate) [218–221] such that down to single particle measurements have been readily demonstrated [106, 109].

We are interested in the dynamics of the local fields in complicated plasmonic structures. Far field spectroscopic techniques generally do not provide direct information on the magnitude, phase and temporal shape of near fields. Moreover, we already encountered in this thesis scenarios where a near-field resonance provides no scattered light, as at a point of perfect absorption. Similarly, there are dark plasmonic modes, and bound states in the continuum in certain nanophotonic lattices that do carry near fields, but hardly carry far field in signatures. In order to probe local field dynamics we must fully characterize the time domain response. This characterization is often done using an interferometric autocorrelation (IAC) technique, in which two temporally delayed pulses interfere in a nonlinear sample and signal is collected as a function of delay. Importantly, this nonlinear operation preserves the spectral phase of the signal which is essential for capturing the time dynamics.

The retrieval of ultrafast optical pulse durations using a nonlinear response in metals using autocorrelation techniques was proposed and demonstrated by Bennett and Zheludev in 1996 [222, 223]. Shortly after, Lamprecht et al. measured the decay time of plasma oscillations in Au and Ag nanoparticles using SHG [102, 224] and THG [220]. Also the chirp signature can be retrieved from second harmonic generation in nonlinear media [225]. Even single nanoparticles are able to produce such IAC traces, employing SHG [108] and THG [105]. THG from single Au nanoparticles was used to produce IAC and frequency resolved optical gating (FROG) traces of ultrashort pulses, to extract plasmon dephasing times [109]. Accanto and

van Hulst demonstrated the use of single nonlinear nanoparticles to calibrate the spectral phase of ultrashort pulses, by iteratively measuring IAC traces and compensating the spectral phase [104]. In addition to single particle resonances also split ring resonator arrays [226] and surface lattice resonances (SLRs) have been used to enhance nonlinear signal [111, 227, 228].

In this chapter we report on the design and realization of an optical setup to study the resonant properties of plasmonic antennas through interferometric autocorrelation measurements. We have built a common path interferometric setup using a birefringence based Mach-Zehnder interferometer to detect nonlinear IAC signal generated in the focus of a lens or a microscope objective. By using a CCD camera as detector, we have an imaging capability, meaning that we can simultaneously record the IAC of nano-antennas, nano-antenna arrays and adjacent reference areas. As the setup is common path, and the IAC of sample and reference is generated in the same field of view, it is in principle possible to directly observe the pulse reshaping effect of nanophotonic resonances. We argue that it is thus possible from a measured reference and sample pulse and using a theoretical model that represents the local field of a Lorentzian nanoresonator to infer properties of the nanoresonator. We report on a calibration of our pulses using a BBO crystal, and on our initial attempts to employ nonlinear signal from bare gold nanoantennas. We demonstrate potential issues one can encounter when using SHG of bare gold. Next, we turn to two-photon excited luminescence (TPEL) of luminescent quantum dots exposed to the near fields of Ag antenna arrays, and show that IAC traces can be measured using TPEL. The preliminary results presented in this thesis on nano-antennas and lattice resonances serve as a simple starting point before investigating more complex systems.

5.2 Theory

5.2.1 Ultrashort pulses

'Ultrashort' electromagnetic pulses are events on the order of picoseconds and less in duration. The pulsed nature of such short time events arises not from, e.g. chopping a continuous wave monochromatic laser beam, but from lasers that intrinsically provide a broad spectrum of frequency components that coherently sum to a pulse. The spectral width of this range of frequencies is inversely proportional to the minimum pulse length in time (at this minimum length the pulse is 'bandwidth limited'). The creation of pulses far below 100 fs has become routine and pulses as short as 3.8 fs (or 1.5 optical cycle) have recently been reported [229]. Experimentally realizing the shortest possible pulse given a certain bandwith becomes increasingly challenging at larger bandwidths, since all frequencies must be synchronised at the pulse's peak.

After a pulse exits a carefully aligned laser, it has yet to pass all optics

present in an experiment before arriving at sample and detector. Given that most types of glass possess a frequency dependent refractive index (e.g., BK7 glass with a refractive index $n \approx 1.52$ varying by about 0.02 over the visible spectrum), and that an average optical path easily contains several centimeters of dispersive material to propagate through, a group delay dispersion of 1000 fs^2 is no exception. Such dispersion will lengthen a 20 fs pulse to 140 fs, while an 80 fs pulse will stretch to 87 fs [230]. In order to execute an experiment at the shortest timescales or highest intensities, knowing the pulse length and shape is of utmost importance, as is combatting dispersion of the optics [231].

Electromagnetic pulses can be described in both the time and the frequency domain. Since the former is most intuitive, we start by expressing the instantaneous electric field of a laser pulse in the time domain, using the complex function

$$E(t) = A(t)e^{-i\omega_0 t}e^{-i\phi(t)}. \tag{5.1}$$

In this equation $A(t)$ is the Gaussian temporal envelope: $Ae^{2\ln 2\frac{-t^2}{\Delta t^2}}$, with A a maximum amplitude and Δt the full width at half maximum (FWHM) of the intensity profile. The exponent $e^{-i\omega_0 t}$ represents a harmonic oscillation with a central angular frequency $\omega_0 = 2\pi c/\lambda$, and $e^{-i\phi(t)}$ adds a temporal phase to the electric field. Figure 5.1 shows example fields with few fringes for didactic purposes. Figure 5.1a plots the real part and absolute value of $E(t)$ for Δt $= 10$ fs, vacuum wavelength $\lambda = 800$ nm and flat phase $\phi(t) = 0$. Looking at Eq. (5.1), it is not straightforward that the field plotted in Fig 5.1a is actually composed of a range of frequencies around the central frequency ω_0, of a bandwidth set by the envelope width. To bring this out, it is necessary turn to the frequency domain by Fourier transformation. Fourier transforming

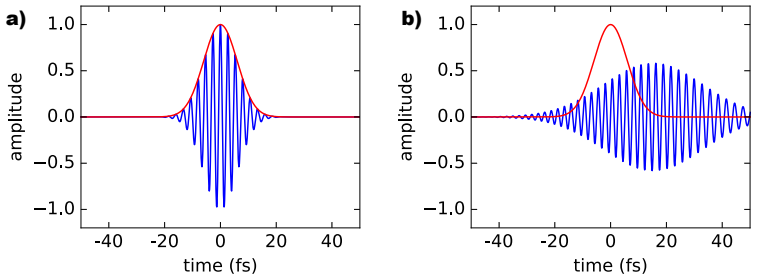

Figure 5.1: a) Real part of the electric field in equation 5.1 plotted as a function of time, at center wavelength 800 nm and a FWHM of 10 fs. Blue: a) no chirp b) 50 fs^2 spectral chirp. The resultant pulse is stretched in time and has a smaller amplitude. Red: absolute value of the unchirped field in both panels, for comparison.

$E(t)$ gives* a result of the form:

$$\hat{E}(\omega) = \sqrt{S(\omega)}e^{i\phi(\omega)}$$

which reveals the spectrum, or bandwidth, $S(\omega)$ that can be measured using a spectrometer. The spectral phase $e^{i\phi(\omega)}$ accounts for the temporal overlap of all frequency components, and determines if the pulse is bandwidth limited (as short in time as the spectrum allows), or longer. If one expands the spectral phase as a Taylor series [232]

$$\phi(\omega) = \phi_0^{(0)} + \phi_0^{(1)}(\omega - \omega_0) + \frac{1}{2}\phi_0^{(2)}(\omega - \omega_0)^2 + ... \tag{5.2}$$

with $\phi_0^{(0)} = \phi(\omega_0)$ and $\phi_0^{(n)} = \mathrm{d}^n\phi/\mathrm{d}\omega^n|_{\omega_0}$, then $\phi_0^{(0)}$ is the carrier-envelope phase, $\phi_0^{(1)}$ is equivalent by the Fourier-shift theorem to shifting the pulse by an overall delay relative to the origin of time, while all higher order terms affect the pulse shape. The second order phase term $\phi_0^{(2)}$ is the most important when it comes to pulse length, and in experiment is effectively seen as pulse lengthening, and chirping. Pulses generally pick up such second order phase terms upon propagation through optical materials due to group velocity dispersion. Figures 5.1a,b provide a comparison of a pulse with identical Gaussian spectrum that is without chirp ($\phi^{(2)} = 0$) in Fig. 5.1a and hence bandwidth limited (10 fs in this example) and with 50 fs^2 linear chirp, and hence elongated in time, in Fig. 5.1b. In this work we are interested in the spatiotemporal properties of near fields, meaning that our experiments require to control and measure precisely the spectrum, chirp and duration of pulses at plasmonic resonators.

5.2.2 Nonlinear optical response

In this chapter we use nonlinear IAC measurements originating in nanoscale systems to study the behavior of plasmonic resonances through their time domain response. We give a brief overview of the field of nonlinear optics in general and of the two nonlinear pathways studied here in particular.

The field of nonlinear optics is concerned with the behavior of light in nonlinear media. In such media, the polarization induced by propagating optical fields is expressed as

$$P = \epsilon_0 \left(\chi^{(1)}E + \chi^{(2)}E^2 + \chi^{(3)}E^3...\right) \tag{5.3}$$

with E the electric field amplitude inside the material, $\chi^{(1)}$ the usual linear susceptibility, $\chi^{(2)}$ the lowest order nonlinear susceptibility and the following

*Note that physical fields are understood to be real-valued quantities, whereas we use complex notation. This means that in the time domain the real field is given by $E(t) + c.c.$ (*c.c.* for complex conjugate). The Fourier transform of this real quantity then gains a negative-frequency counterpart.

$\chi^{(n)}$ the n-th order nonlinear susceptibilities. Since nonlinear susceptibility terms are usually very small compared to the linear term, nonlinear processes are not easily observed, unless very high fields are at hand. Hence, the field of nonlinear optics generally implies ultrafast pulses, with high instantaneous field strengths. While the first nonlinear optical process, two photon absorption, was theoretically predicted in 1931 [233], physicists had to wait for the invention of the laser some thirty years later to demonstrate the first *experimental* realisation of nonlinear optical processes [234, 235]. While in daily life, nonlinear optical processes are hardly evident (except for perhaps green laser pointers [236]), in technology they provide for frequency-converted lasers, a host of ultrafast laser spectroscopy techniques, and are seen as instrumental for classical and quantum optical signal processing.

The nonlinear interaction of electric fields with matter gives rise to a large host of nonlinear processes. In this chapter we will use only processes that provide emitted signals of a strength proportional to the square of the incident intensity. These are the second order ($\chi^{(2)}$) process of second harmonic generation (SHG), and luminescence upon two-photon excitation (TPEL). The latter is a third order process, related to the imaginary part of $\chi^{(3)}$, but depends quadratically on the incident intensity. Both of these processes we will elicit in nano-resonators to characterize their near-field optical field behavior. Far-field measurements on *linear* optical response can not reveal local electromagnetic field properties, whereas one can retrieve near-field pulse properties locally from nonlinear signals, if the nonlinearity at hand is spatially confined to that near-field.

Second harmonic generation

Second harmonic generation (SHG) is a second order nonlinear process, in which two photons of the same frequency are converted into one photon of double the frequency, which is qualitatively easily seen to be one of the consequences of the $\chi^{(2)}$ term in Eq. (5.3) (since squaring $E = \mathrm{Re}E_0e^{-i\omega t}$ provides terms at frequency 2ω). The process follows a second order power dependence, i.e. the second harmonic intensity depends quadratically on the input power. In order for a medium to allow the occurrence of SHG some conditions have to be met to achieve nonzero χ^2. Generally, nonlinear optical responses result from an anharmonic response of the electrons in matter, as could be modelled, e.g. as anharmonic corrections to the Lorentz-model for the refractive index in solids due to the response of bound electrons in solids. For anharmonicity to result in $\chi^{(2)}$, further some sort of symmetry breaking in the nonlinear material is required, as is the case for all *even* order nonlinear processes. In a bulk solid this requirement is met when the crystal structure is non-centrosymmetric, in other words, in such a medium the polarization response is slightly different depending on the propagation direction of E. An example of such material is the non-centrosymmetric version of barium borate

(β-BaB_2O_4, β-BBO), a nonlinear crystal that is widely used for frequency conversion processes [237]. Materials that *do* carry inversion symmetry can still show a nonlinear response via symmetry breaking at interfaces, defects and by asymmetric geometry designs [238]. Even though bulk gold is inversion symmetric, it is still often used in nonlinear experiments in plasmonics [239], where both the interfaces and asymmetric designs can provide high nonlinear susceptibility.

To identify a measured signal as originating in SHG, it must be checked that the signal shows a quadratic power dependence, and the spectrum is at exactly half the wavelength of the incident light. SHG furthermore inherits its temporal and coherence properties from the incident light, as is for instance evident in the requirements of phase matching to obtain efficient SHG from bulk nonlinear crystals. In this work phase matching is not relevant, as we work with samples much thinner than a wavelength.

Two-photon luminescence

Two-photon excited luminescence is a third-order nonlinear optical process originating from two-photon absorption (same or different frequencies), and depends on the imaginary part of the third-order nonlinear optical susceptibility, $\mathrm{Im}\,\chi^{(3)}$. Physically, two-photon excited luminescence corresponds to eliciting an electronic transition in the matter, where for instance an electron is brought from the ground state to the excited state of a fluorophore, to subsequently generate fluorescence by spontaneous emission. In this process, generally a single input photon has insufficient energy to match the fluorescence transition, so that two pump photons are required. As a result the common denominator with SHG is that the output power depends quadratically on the input power. However, there are also important distinctions between TPEL and SHG. In $\chi^{(2)}$ processes, electrons do not undergo real quantum mechanical transitions, the nonlinearity is essentially instantaneous and SHG thus preserves spectral, coherence and temporal properties of the input light in the output. In contrast, the spectrum of TPEL is fixed by the quantum mechanical level structure of the fluorophore at hand, the emission is temporally incoherent, and the dynamics are set by the fluorescence decay kinetics of the fluorophore. The consequence of this is that fixed-frequency power dependence measurements will not be able to discriminate between SHG and TPL, but temporal and spectroscopic analysis of the nonlinear emission readily will. Efficient TPEL signal requires a suitable fluorophore, and constraints on centrosymmetry are less relevant.

5.2.3 Characterizing ultrashort pulses using correlation measurements

In this chapter, we are interested in determining the near-field strength and dynamics inside nanoscale photonic resonators. Since experimental research in the field of ultrafast optics generally requires the researcher to calibrate pulse characteristics, there are well established techniques that we review in this section. Temporal pulse characterisation generally requires intricate techniques since no optical detector in itself is capable of resolving the instantaneous electric field at optical frequencies. Instead, optical detectors generally measure intensity ($|E(t)|^2$), averaged over many optical cycles. A further issue with characterizing at femtosecond resolution is that ultrashort pulses are already amongst the shortest man-made events, meaning that also there does not exist a shorter event to sample the waveform in, e.g., a stroboscopic approach [240]. Pulse characterization methods therefore rely on sampling a pulse with a copy of itself in a form of nonlinear interferometry, or autocorrelation.

This section introduces the basic concept of field and interferometric autocorrelation. Field autocorrelation was used in chapter 3, and can retrieve the spectrum but not the the spectral phase of a pulse. To retrieve a pulse's spectral phase, one has to use the interferometric autocorrelation, which is a nonlinear instead of linear interferometric signal. Pulse characterization with interferometric autocorrelation requires a model for the pulse shape, and within such a model provides a retrieval of parameters such as pulse length, spectrum and chirp.

Field autocorrelation

A field autocorrelation operates by creating two copies of an optical pulse at mutual delay τ, overlapping them on a detector, and determining the time integrated sum, i.e., the overlap between the two fields. No nonlinear element (apart from the detector) is used. The measured intensity of the two collinear beams on a detector is given by

$$\begin{aligned} I_{\text{field}}(\tau) \propto \langle |E + E_\tau|^2 \rangle(\tau) &= \int_{-T}^{+T} |E(t) + E(t+\tau)|^2 \mathrm{d}t \\ &= \int_{-T}^{+T} |E(t)|^2 + |E(t+\tau)|^2 + E(t)\overline{E(t+\tau)} + \overline{E(t)}E(t+\tau)\ \mathrm{d}t \\ &= 2\langle |E|^2 \rangle + 2\,\mathrm{Re}\,(E \star E) \end{aligned} \tag{5.4}$$

where $\overline{(\dots)}$ means complex conjugation and $\star$ is the cross correlation

$$f \star g = [f(t) \star g(t)](\tau) = \int_{-\infty}^{+\infty} \overline{f(t)} g(t+\tau)\ \mathrm{d}t.$$

The delay τ between two pulse copies is generally realized using a delay line that varies the optical path of the pulse trains in sub-micrometer steps resulting in a time resolution in τ sufficient to adequately resolve optical fringes, exactly as in chapter 3. The detector integration time T is typically much longer than the pulse length and often even encompasses many pulses, such that each datapoint in the autocorrelation trace is an average over multiple pulses. The field autocorrelation encodes only the spectrum of the pulse: bandwidth limited pulses and chirped pulses with the same bandwidth will yield exactly the same autocorrelation. This is illustrated in Figure 5.2, which plots the field autocorrelation in Eq. (5.4) of the example pulses shown in Fig. 5.1, as a function of time delay τ. The integrand in Eq. (5.4) contains four terms of which the first two are a delay independent background, normalized to 1. The last two terms are the cross correlation terms resulting from constructive and destructive interference between the two fields, which add an envelope of oscillations to the plotted signal. The two traces in Fig. 5.2a and b are identical,

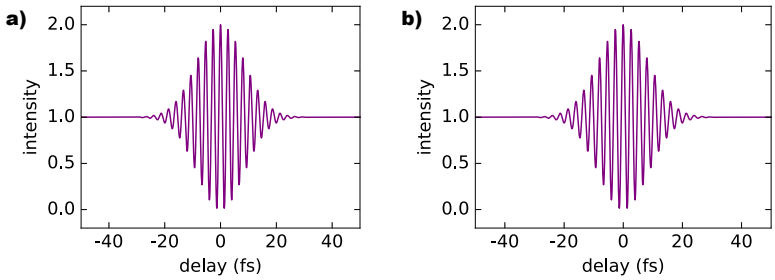

Figure 5.2: Field autocorrelations (Eq. (5.4)) of the pulsed electric fields shown in Fig 5.1. Input fields have a center wavelength at 800 nm, 10 fs pulse duration and a) no chirp, b) 50 fs^2 chirp. Since the interference terms in the field autocorrelation lose their spectral phase information once they hit the detector, the two correlations shown are identical.

as the only difference between the two input fields is in the spectral phase $e^{-i\phi(\omega)}$ to which the field autocorrelation is insensitive. Using the Wiener-Khinchin theorem[†] the measured interference term $\int_{-\infty}^{\infty} \overline{E(t)}E(t+\tau)\mathrm{d}t$ can equivalently be written as the Fourier transform of $|E(\omega)|^2$. Upon taking the absolute value of the spectrum $E(\omega)$, the spectral phase is lost (the only characteristic feature that distinguishes a chirped pulse from a not chirped pulse). Thus a field autocorrelation can be used to determine the complex-valued *transfer* function of samples (comparing cross correlations without and with sample), as in chapter 3, to determine the linear spectral response function of a sample, but not to evaluate the pulse shape itself.

[†]The cross correlation theorem applied with $f = g$.

Interferometric autocorrelation

In order to record the crucial spectral phase information that characterizes a pulse, interference of the fields (or: squaring) should take place *before* the fields hit a detector. A common method to realize this is to perform an autocorrelation in which the two collinear beams are combined in a second order nonlinear material. The frequency-doubled light created by the interaction between the two beams contains both contributions from each individual beam [241], and interference terms. The resultant interferometric autocorrelation (IAC) signal measured by a detector, as a function of delay τ then reads

$$\begin{aligned} I_{\text{interferometric}}(\tau) \propto \langle |(E+E_\tau)^2|^2 \rangle(\tau) &= \int_{-\infty}^{+\infty} \left| (E(t)+E(t+\tau))^2 \right|^2 \mathrm{d}t \\ &= \int_{-\infty}^{\infty} |E(t)^2 + 2E(t)E(t+\tau) + E(t+\tau)^2|^2 \mathrm{d}t \\ &= 2\langle |E^2|^2 \rangle + 4\,\mathrm{Re}\left(\overline{E}\,E^2 \star E\right) + 4\,\mathrm{Re}\left(E \star \overline{E}\,E^2\right) \\ &\quad + 2\,\mathrm{Re}\left(E^2 \star E^2\right) + 4\left(|E|^2 \star |E|^2\right) \end{aligned} \tag{5.5}$$

Here the interference of the new terms, $E(t)^2$ and $E(t+\tau)^2$, both with each other and with the cross correlation term $2E(t)E(t+\tau)$ (which was in principle already there in the field autocorrelation) are the contributions that ensure that spectral phase information is contained. Figure 5.3 illustrates the interferometric autocorrelation (IAC) for the example input electric fields $E(t)$ and $E_{\text{ch}}(t)$ from Figure 5.1. In both panels the signal is composed of an envelope of oscillations offset from a constant nonzero background. With this background normalized to 1, the fringes take values from 0 up to 8. The traces shown in a and b are clearly different. Compared to the the unchirped case, the chirped pulse results in notable wings at long delays. In addition the IAC

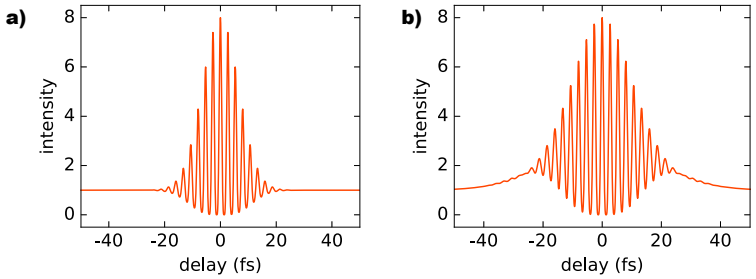

Figure 5.3: Interferometric autocorrelations of the pulsed electric fields shown in Fig 5.1, plotted using Eq. (5.5). The input fields have a center wavelength at 800 nm, 10 fs pulse duration and a) no chirp, b) 50 fs^2 chirp. In contrast to the field autocorrelation, the interferometric autocorrelation is able to distinguish between chirped and non chirped pulses.

trace of the chirped pulse results in a wider envelope. The IAC can not be directly inverted to obtain center frequency, bandwidth and chirp. Instead, determining the chirp of a pulse proceeds by fitting IACs calculated for an explicit model (e.g., Gaussian chirped pulses) to the data to match the fringes, envelope and wings. The 1:8 contrast is not strictly a fit parameter, as this ratio is only dependent on the process of the IAC being quadratic in intensity, and not on pulse shape. Eq. (5.5) can be separated into 3 contributions: the background envelope, oscillations at ω and oscillations at 2ω, which are plot for a bandwidth limited pulse and a chirped pulse in Figure 5.4. It shows that, in comparison to the IAC of a bandwidth limited pulse, in a chirped pulse i) the background envelope is wider, ii) the 2ω oscillations span over a *smaller* delay, whereas iii) the ω oscillations span over a *wider* delay. This increased range of interference at the fundamental frequency comes from the aforementioned interference between $E(t)^2$ and $2E(t)E(t+\tau)$ and helps, alongside an increased oscillation-free background, to intuitively distinguish between measured IAC traces.

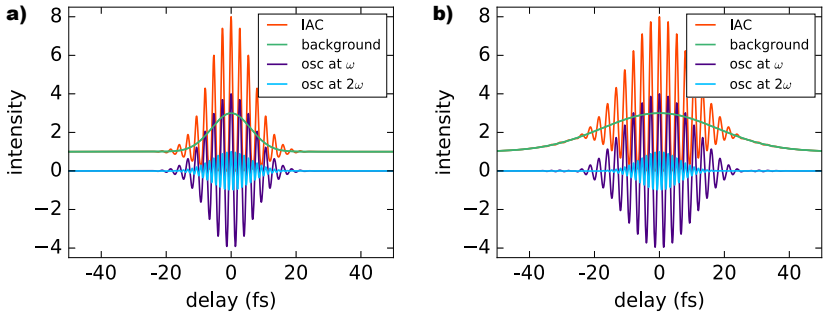

Figure 5.4: Interferometric autocorrelations from Figure 5.3 split in three contributions: background, oscillations at ω and oscillations at 2ω for a) an unchirped and b) a chirped pulse of 10 fs at center wavelength 800 nm. In b), at $\pm$ 30 fs an oscillation-free elevated background is visible, a characteristic chirp feature.

5.2.4 Interferometric autocorrelation on resonant systems

At the heart of this chapter is the ambition to study the dynamics of near fields at plasmon antennas by interferometric autocorrelation, where the nonlinear signal is generated *at* the antennas. An important distinction with most nonlinear crystals used for femtosecond pulse characterisation is that these have a nonlinear response that is in itself essentially frequency independent over the scale of the experiment. Instead, the main physics of interest for nanophotonic resonators is their strongly structured spectrum, which is equivalent in the time domain to, e.g., resonance ring down effects. Important contributions in this field have already been made by [104, 105, 108, 109, 224], as reviewed in

the introduction. The interferometric autocorrelation technique presented in the previous section can be easily extended to also allow a resonant response to the incoming electric field, which we will treat theoretically next.

We propose a simple model for how the interferometric autocorrelation is modified by a nanoresonator that is resonant near the fundamental (pump) frequency, but not near the harmonic frequency. We assume a resonant system with a single Lorentzian response at the fundamental frequency, and assume this system to also provide the nonlinearity for IAC. The measured IAC trace will thus originate not from the incident field $E(t)$ but from the local field $E_{\mathrm{loc}}(t)$, which is given by the incident field convoluted with $\mathcal{G}(t)$, the response of the system in the time domain:

$$E_{loc}(t) = E * \mathcal{G} \tag{5.6}$$

where $*$ is the convolution

$$f * g = [f(t') * g(t')](t) = \int_{-\infty}^{+\infty} f(t')g(t-t')dt'.$$

For a harmonic resonator, which has a Lorentzian lineshape, the time domain response function $\mathcal{G}(t)$ reads

$$\mathcal{G}(t) = iH(t)\frac{e^{-i\omega_+ t} - e^{-i\omega_- t}}{\omega_+ - \omega_-} \tag{5.7}$$

$$\omega_\pm = -\frac{i\gamma}{2} \pm \sqrt{\omega_0 - \left(\frac{\gamma}{2}\right)^2} \tag{5.8}$$

$$H(t) = \begin{cases} 0 & \text{if} \quad t < 0 \\ 1 & \text{if} \quad t \geq 0 \end{cases} \tag{5.9}$$

An example response function $\mathcal{G}$ is plotted in Figure 5.5, with damping

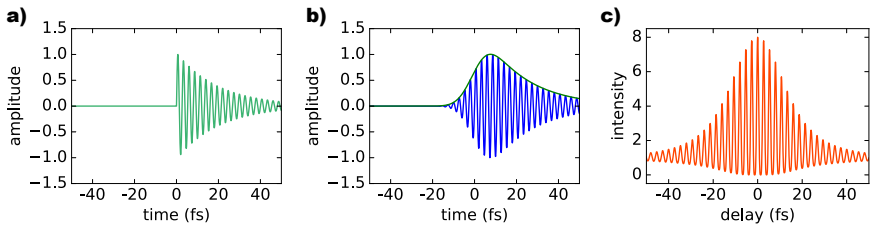

Figure 5.5: a) The time domain response function $\mathcal{G}$ of a resonance centered at 800 nm, with a damping rate γ = 1x10^{14}/s. b) The resultant local field $E_{\mathrm{loc}}(t)$ after convolution with a bandwith limited pulse of 10 fs duration at the same wavelength c) The interferometric autocorrelation trace of $E_{\mathrm{loc}}(t)$.

rate γ = 1x10^{14}/s and center frequency at $\omega_0 = 2\pi c/\lambda$ with λ = 800 nm. Fig. 5.5a shows the resonator's oscillatory response to some excitation at $t = 0$ (imposed by $H(0)$). The convolution between $\mathcal{G}$ and the example pulse in Fig. 5.1a, i.e., $E_{\mathrm{loc}}(t)$ is plotted in Fig. 5.5b. The IAC trace for a resonant system as a nonlinear medium takes the same form as Eq. (5.5), but now evaluated with the local field $E_{\mathrm{loc}}(t)$, instead of with the incident field $E(t)$. Figure 5.5c shows the IAC trace for the local field in (b). Extracting $\mathcal{G}$ from an IAC such as shown in (c) requires a reference measurement on a non-resonant sample to retrieve the incident pulse properties, and a model for $\mathcal{G}$.

This simple model gives a basic understanding for the quadratic nonlinear process of SHG and its effect on a correlation function. Since SHG is a coherent process, effects similar to $E * \mathcal{G}$ can occur for a system that is resonant at 2ω. Generally, the IAC will be appreciably modified relative to that of the incident field only when the decay rate γ is small, meaning that the resonance shows a ring down comparable to the incident pulse width.

5.2.5 TPEL and interferometric autocorrelation

In this chapter we report an experimental configuration to study the local dynamics of plasmonic arrays of nanoantennas, and we demonstrate the essential experimental techniques that are needed for such an undertaking. Using as nonlinear signal initially SHG from Au nanoparticles to measure IAC traces proved to be challenging in our setup that uses a laser at 1 MHz repetition rate, meaning lower repetition rate but higher peak pulse power than in many earlier studies that use 80 MHz systems [106, 218–221]. This, and other issues in terms of stability, resonant spectral dependence and additional (nonlinear) emission mechanisms, lead us to explore a different approach on basis of TPEL.

In this work we will show that many of the issues with SHG can be circumvented using two-photon excited luminescence from a monolayer of quantum dots aided by the field enhancement from nanoparticles as the key process underlying IAC measurements. TPEL from quantum dots shows a very high signal compared to SHG from gold antennas, helping to reduce integration times and avoid thermal/structural stability issues that occur at high excitation power. In addition TPEL can be excited over a broad frequency range but is emitted at a fixed frequency. This assists in separating out resonance enhancements at the fundamental frequency from effects that might occur at 2ω, simply by tuning the pump laser. Nonetheless, like SHG, TPEL depends quadratically on input power and is therefore very suited for nonlinear correlation measurements. Since it is not trivial that TPEL and SHG produce nominally identical interferometric autocorrelation traces, we provide a derivation here.

Following [242], the time-averaged photon flux of TPEL can be expressed

as:

$$\langle F_{TPL}(t)\rangle \approx \frac{1}{2}\,\eta_{col}\,\eta_2\,C\sigma_2\,\langle I^2(t)\rangle \int_V s(\mathbf{r})dV \tag{5.10}$$

where η_{col} is the collection efficiency, η_2 is the luminescence quantum yield, C is the molar concentration (since most applications assume fluorophores like fluorescent dyes), σ_2 is the molecular two-photon absorption cross-section (common units: 1 GM = 10^{-50} cm^{4}s/photon), $I(t)$ is the excitation field intensity

$$I(t) = \frac{cn\varepsilon_0}{2}\,|E(t)|^2$$

and $s(\mathbf{r})$ is the spatial distribution of the excitation field over the volume of excited nonlinear medium. The key distinction between SHG and TPEL is that for SHG it is the square field E^2 that enters, meaning that coherence matters. In fact, this ultimately underlies, for instance, phase matching. Instead, for IAC it is the fundamental intensity $|E|^2$ that converts into local generation of TPEL, meaning that TPEL contributors add incoherently. The IAC formula for two-photon excited luminescence reads:

$$\begin{aligned} I_{TPA}(\tau) \propto \langle |E+E_\tau|^4\rangle(\tau) &= \int_{-\infty}^{+\infty} |E(t)+E(t+\tau)|^4\,dt \\ &= 2\langle |E|^4\rangle + 4\,\mathrm{Re}\left(\overline{E}\,E^2 \star E\right) + 4\,\mathrm{Re}\left(E\star\overline{E}\,E^2\right) \\ &\quad +2\,\mathrm{Re}\left(E^2\star E^2\right) + 4\left(|E|^2\star|E|^2\right) \end{aligned} \tag{5.11}$$

The above formula is identical to the IAC formula for SHG, except the first term $2\langle|E|^4\rangle$, which in the case of SHG equals $2\langle|E^2|^2\rangle$. Following [242], one can express $\langle|E|^4\rangle$ (which occurs in both the above equations) as $g\langle|E^2|^2\rangle$, where g is the degree of the second-order temporal coherence of the excitation field. As a result, both two-photon luminescence and SHG have quadratic dependence on the excitation power, *and*, upon normalization, both phenomena will produce exactly the same IAC traces. The notion that $\langle|E|^4\rangle$ and $g\langle|E|^2\rangle$ are identical is intuitively understood by a simple power argument according to which the IAC at long delay and at zero delay must always stand in 1:8 ratio. The terms at hand correspond to the constant 'background' at large pulse delay, which is twice the SHG signal due to a single pulse. Instead at zero delay, the signal is due to a single pulse at twice the field strength, hence 16 times the signal (argument equivalent to noting the square intensity dependence).

5.3 Methods

5.3.1 Experimental setup

We present a fully common path interferometric autocorrelation setup, which implements birefringent wedged crystals to create pulse pairs that

are collinear, yet with a precisely scanneable time delay, in a configuration due to Brida et al. [243]. The stability delivered by this common path arrangement and the possibility to use microscope objectives for in and out coupling enables in principle measurements down to single nanoparticles. A main difference with the setup presented in chapter 3 is in where the delay time for interferometry is scanned. In chapter 3 we passed a sample and reference pulse at fixed time delay and slight spatial offset through the sample plane, recombined them spatially (essentially forming a Mach-Zehnder interferometer), and subsequently used a scanning Michelson interferometer to collect interferograms on a detector. Instead the setup presented here is designed so as to impose a scannable time delay *before* the sample, allowing interference between the two beams right at the focus, where the nonlinear interaction takes place. Interferometric autocorrelations from nanoparticles have been used to fully characterize and chirp-compensate femtosecond pulses, as demonstrated by [104].

Birefringent crystals for phase-locked pulse pair generation are commonly used in femtosecond common path interferometry schemes, as demonstrated by [244, 245]. To collect IAC traces a compact and stable method to scan the mutual delay in a perpendicular pulse pair is to use a birefringent wedge pair as introduced by Brida et al. [243]. This socalled 'TWINS' technique (Translating-Wedge-based Identical pulses eNcoding System) has already been used in plasmonics to collect nonlinear interferometric autocorrelations from colloidal gold nanorods by Zhao and coworkers [103]. We present a slightly modified version of this system by implementing the delay line in reflection, such that we need not four but only two wedges, which makes the alignment easier. Figure 5.6 shows the setup schematically.

First we discuss the common path delay line, visible in Fig. 5.6 as the right most part (starting at the beamsplitter). An incoming linearly polarized femtosecond pulse train, filtered to block light below 700 nm using a longpass filter (FELH0700, Thorlabs), is oriented with its electric field vector at 45 degrees relative to horizontal using an achromatic half wave plate (AHWP10M-980, Thorlabs). A beamsplitter (BP145B2, Thorlabs) sends this pulse train to the delay line that operates in reflection and works as follows. First, a birefringent α-barium borate (α-BBO) block with its fast, extraordinary, axis oriented horizontally, separates the horizontal and vertical field components of the pulse in time. This splitting principle relies on the fact that different polarizations experience a different refractive index in birefringent media. A fixed time delay between the two polarizations results, the magnitude of which is determined by the crystal thickness and the refractive index contrast. In this setup, a crystal thickness of 4.5 mm is used to imprint a 1.7 ps delay (the refractive index difference between the two optical axes in α-BBO is 0.115 at $\lambda = 800$ nm). The pulse pair subsequently travels through a pair of α-BBO wedges with the fast optical axis oriented perpendicular to that of the block (i.e. *vertically*). First we position the wedges such that their combined optical

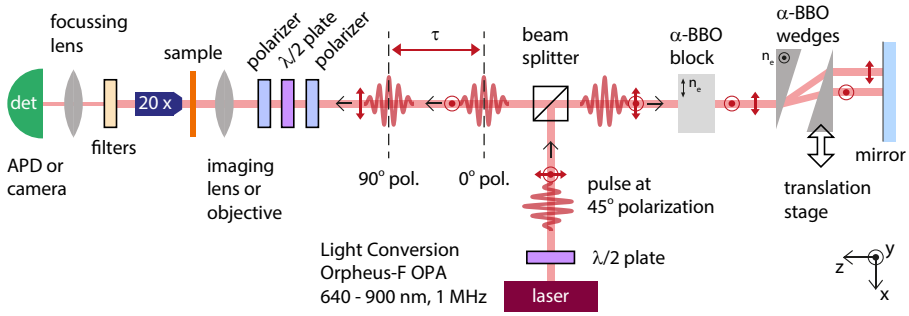

Figure 5.6: The common path interferometry setup presented in this chapter, used to collect nonlinear autocorrelation traces of ultrashort pulses that interacted with plasmonic near fields. Right of the beam splitter is the birefringence based delay line. A 45 degrees polarized femtosecond pulse is split in time in its horizontal and vertical parts in an α-BBO block. Next, the two pulses are mutually delayed using an α-BBO wedge pair of which the second wedge is translated in the x-direction to control the time delay. The rest of the setup shows the excitation of the sample with either a lens or an objective. Nonlinear signal is collected using an objective, filtered, and send to a spectrometer, focussed on an APD or imaged on a camera. Details of the optics and detectors used are described in the main text.

path equals the optical path in the α-BBO block. In this configuration the fixed delay imposed by the block is exactly cancelled by the wedges, resulting in overlapping pulses. One can then translate the second wedge in the transverse direction to tune the optical path difference between the two pulses, and thereby their mutual delay, by passing though more or less material. After passing the wedges, the orthogonally polarized and temporally shifted output beams are still parallel to one another but offset in the x-direction. After being reflected by the mirror the two beams trace back the same path, which doubles the time delay and removes the spatial offset. A diagonal polarizer (LPVIS100-MP2, Thorlabs) is used to project the two polarizations on the same axis such that they can interfere. Finally, the beam passes through a half waveplate (AHWP10M-980, Thorlabs) and a second polarizer (LPVIS100-MP2, Thorlabs), where the half wave plate is used to control the incident power and the second polarizer is positioned antidiagonal with respect to the first to compensate for beam distortion. All experiments are performed at diagonal incident polarization.

The main advantage of this approach is that attosecond stability and resolution can be attained, and that large sideways movements of the wedged prisms translate into fine control over the time delay. Specifically, the stepper motor (a combination of a DC Servo Motor Controller, TDC001, and a motorized actuator, Z812, Thorlabs) in the delay line scans a distance of 4 mm in increments of 0.5 μm, resulting in scans consisting of up to 8000 data points. The wedges are cut at an angle of 15 degrees, such that a sideways displacement

of the second wedge of 0.5 μm results in a temporal delay increment between the two pulses (after double passing) of 1.03 as. The total delay range spans 800 fs. All α-BBO crystals in this setup are custom made (supplier: Foctek Photonics, China).

Having singled out the delay line in particular, we now to turn to a description of the full setup. The incoming pulse train is produced by a Light Conversion PHAROS 16 W pump laser centered at 1028 nm at a repetition rate of up to 1 MHz, half of which is fed into a Light Conversion ORPHEUS-F OPA that is continuously tunable between 650 and 920 nm, resulting in a final pulse duration of 70 fs and output power 600 mW. The output is passed through the delay generator and sent to the sample. We weakly focus the beam on the samples on glass substrates using a lens with focal distance 5 mm (AC254-050-B, Thorlabs) or a 20x objective (NA 0.45, LU Plan Fluor, Nikon). The degree of focusing varies per experiment and depends on the stability of the sample and on the obtained count rate. All experiments in this setup were done in transmission, with on the rear side of the sample either a 20x (NA 0.5, Plan Fluor, Nikon) or 50x or 100x air objective (NA 0.8 or NA 0.9 respectively, LU Plan Fluor, Nikon) or a 100x oil objective (NA 1.45, Plan APO, Nikon). The choice of objective depends on the type of sample and the specific detection scheme. For all measurements described in this chapter we use two 650 nm shortpass filters (FESH650, Thorlabs) to block the fundamental beam. For the SHG measurements we use a bandpass filter around 400 nm (FB400-40, Thorlabs), while for the process of TPEL we switch to a set of shortpass and longpass filters (2x FESH0650, Thorlabs and 1x HQ500LP, Chroma Technology). After filtering there are several means that we employed to characterize the generated (nonlinear) signal. For spectral measurements we use a Si-CCD equipped grating spectrometer (Andor Shamrock 303i).

For the collection of IAC traces we implemented two detection schemes. One is an avalanche photodiode Micro Photon Devices PDM-50 (Geiger mode APD, over 15% quantum efficiency at 400 nm), used as a point detector in Geiger mode. Signal is collected using a 50x or 100x air objective or the 100x oil objective. For focussing on the APD we used a lens or a 20x or 50x objective. Due to the very low background and high sensitivity of APDs we can work with very low nonlinear signals, using furthermore temporal gating to only measure signal coincident with the laser pulse train, thereby suppressing the background signal. A downside of this detection scheme is that count rates should be well below the laser repetition rate to avoid skewing of the photon counting statistics. The low repetition rate of 1 MHz of our laser system then requires an integration time of 10 seconds per data point. Alternatively, we image the transmitted signal on a CCD camera (Coolsnap, 12-bit CCD using Sony ICX285AL chip, commonly used in single molecule microscopy) using a 200 mm focal distance lens (AC254-200-A-ML, Thorlabs). Capturing an image of the nonlinear signal at each delay τ yields a data set from which autocorrelation traces of a single pixel, or averaged over a larger region of

interest can be taken. This method is very convenient as it enables to measure in parallel multiple lithographically defined nano-antenna arrays of different geometries, and at the same time record a reference trace right next to each field. A downside of this approach is the data volume.

5.3.2 Sample design and fabrication

The plasmonic samples we study in this chapter are Au and Ag nanoparticle arrays which are lithographically fabricated on glass. For the TPEL measurements these arrays are covered in a monolayer of quantum dots. We first explain the choice of design parameters and then describe the fabrication procedure.

For the first sample studied, which is composed of arrays of resonant Au nanorods on glass, we chose particle dimensions $L \times 40 \times 50$ nm ($l \times w \times h$) with length L varying from 100 to 150 in steps of 10 nm, to support resonances between 700 and 900 nm, around the fundamental laser excitation wavelength. We also prepared variants of simple nanorods where one side of the rods has been narrowed in order to break inversion symmetry in the design (increase SHG efficiency), and to have sharper tips that further enhance plasmonic hotspots via the lightning-rod effect (concentration of the field at surfaces of strong curvature [246]). We implemented square array pitches of 270 and 400 nm in order to enhance the outcoupling of nonlinear emission in the normal direction by grating anomalies around the SHG wavelength, assuming an index of 1 or around 1.58 (typical for the glass substrate). The nanorods were covered in a 150 nm layer SiO_x using electron beam physical vapor deposition at 57 nA (Flextura M508 E, Polyteknik), in order to switch between an air and an oil objective during experiments. The second, main set of experiments used silver instead of gold nanorods, in order to benefit from lower Ohmic losses. We prepared a plethora of silver nanorod arrays, with a wider range of antenna lengths (50 to 150 nm in steps of 5 nm), pitches to control diffractive surface lattice resonance effects (pitches between 500 and 600 (steps of 5 nm)), and with multiple nanorods grouped per unit cell to generate narrow gaps. The resulting sample had 21 by 21 arrays of size 10 by 10 micron each, thereby being ideally suited for parallelized detection of the IAC traces by imaging on the CCD camera.

As regards fabrication of the antennas, we refer to section 5.3.2 for the electron beam lithography and lift off process. The fabrication processes are identical for Ag and Au antennas, except for the metal evaporation step, which for the case of Ag is done using an evaporation current of 40 mA. After employing the bare Au nanorods for the initial SHG measurements we turned to collecting TPEL signal, which as opposed to SHG is not scattered by metal nanoparticles but rather emitted by luminescent particles. For this purpose we selected the most bright and stable emitters at hand, which are CdSe/CdS/ZnS (core/shell/shell) quantum dots, with an inner and outer shell of 8 and 2

monolayers thickness respectively. Quantum dots are donated by coworkers from the group of Houtepen in Delft. The dots are covered with a mixture of ligands, i.e., oleic acid and oleylamine, and are initially dispersed in toluene. Before spincoating the substrate is cleaned by immersion in first acetone and subsequently isopropanol for 15 seconds each, and blow dried. The quantum dots are spincoated using a small amount (30 μL) at high concentration (precise concentration unknown) at two sequential speeds. The spinning is started at 500 rpm for a duration of 32 s, with ramp rate of 250 rpm/s. After 32 seconds the spin rate is increased to 1000 rpm for 92 seconds with ramp rate 250 rpm/s. During spin coating the toluene evaporates and the quantum dots assemble in a continuous layer covering the surface. We measured the thickness of this layer using a mechanical surface profilometer (KLA Tencor Stylus Profiler P7) to be 17 nm, corresponding to a monolayer.

5.3.3 Fit procedure to analyze IAC traces

We fit the measured interferometric autocorrelation traces to an explicit model. For the case of a reference pulse this model takes the shape of a Gaussian shaped chirped pulse, and uses two fit parameters: the pulse length (FWHM) in fs and the chirp in fs^2. In the case of an IAC taken from a resonant sample we fit the measurement to the IAC of local field, which we model as a convolution between the incident Gaussian (with the previously fit parameters from the reference measurement as fixed input) and the response function in Eq. (5.7), to retrieve the life time parameter γ.

We describe the fitting process step wise, starting with the reference. To obtain an initial guess for the fitting we first take the Fourier transform of the IAC trace. This yields a spectrum with nonzero values close to zero, representing the pulse envelope and the background, a main peak around ω for the fundamental oscillations (which gives an estimation for the chirp), and a peak around 2ω for the oscillations at double the incident frequency. We select a frequency window around the lowest frequencies and inverse Fourier transform to retrieve an initial guess for the pulse length. Similarly we spectrally select around ω to obtain a guess for the chirp. The next step is to use the trial function with this estimated pulse length and chirp to generate an IAC, subtract the experiment from this trace and calculate the error squared. Subsequently an error minimization algorithm is used to find the pulse length and chirp that best match the data. To control the fit of the chirp signature we implemented a weighted error function that allows to emphasize in the fitting on larger delays $\pm\tau$, to more accurately fit the wings. Fitting the reference IAC takes a few seconds up to a minute. For a demonstration of the fitting procedure we refer the reader to Figure 5.9.

For the IAC traces that we obtained from a plasmonic local field we assume that the local field that yields the IAC is a convolution between the incident field and a response function as described in Eq. (5.6). Following the proce-

dure above, in this case using a local field with the previously fitted values (pulse length and chirp) as fixed input, the damping rate γ is fitted to the measurement.

5.4 Setup calibration

The results presented in this chapter have an exploratory character and the goal of this chapter will be two fold. First, we report the calibration of the setup through a set of measurements on a simple nonlinear crystal. Next, in section 5.5.3 we intend to demonstrate the intricacies of collecting nonlinear IAC traces from nanometric volumes using SHG as the nonlinear signal. We present a set of IAC results obtained from resonant Au nanoparticle arrays, and demonstrate several potential pitfalls that one should be aware of. These generally occur, but are exacerbated by the fact that we built a setup on basis of a relatively low repetition rate laser (1 Mhz as opposed to 80 MHz) to measure plasmonic nonlinear signal. Finally, this chapter introduces TPEL as a promising alternative for SHG to obtain plasmonic IAC traces. We show an initial set of results using quantum dots of which the signal is strongly enhanced using the plasmonic hotspots of resonant Ag nanoparticle arrays. Also measuring a reference IAC, the IAC traces can be fitted to an oscillator model to extract resonant effects that manifest in the time domain response.

5.4.1 Calibration of setup functionality on BBO

The initial calibration of the setup is performed using a 10 μm thick β-BBO crystal, which is known for efficiently producing SHG. The verification includes frequency conversion, power dependence and IAC trace collection measurements. To collect the frequency-converted spectrum, the transmitted signal of a single pulsed laser beam, i.e., without using the delay line, is

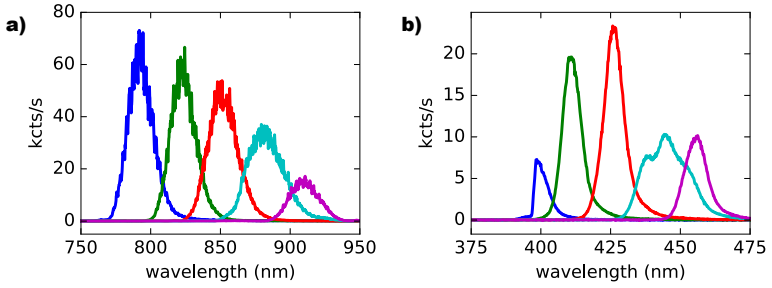

Figure 5.7: a) Spectra of the fundamental beam of the laser, for center wavelengths 790, 820, 850, 880 and 910 nm. b) Corresponding spectra of the SHG signal generated in β-BBO.

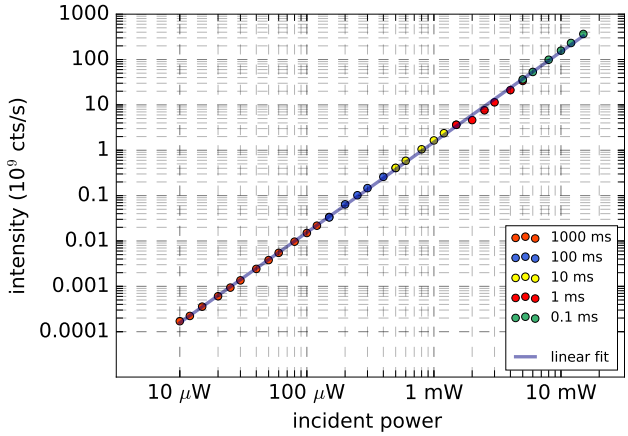

Figure 5.8: SHG signal from a 10 μm thick β-BBO crystal as a function of incident power at excitation wavelength 820 nm, collected on the camera, using a bandpass filter around 400 nm. Both axes show a log scale. The measured intensity shows perfect quadratic power dependence (slope is 1.99), which confirms, together with the frequency doubling in Fig 5.7, that the detected signal originates in second harmonic generation.

collected using a 20x objective (Plan Fluor, NA 0.5, Nikon). The fundamental beam is blocked and the transmitted second harmonic light is collected on a spectrometer (see section 5.3.1 for details). Figure 5.7a shows the spectrum of the fundamental beam used for this measurement, collected in absence of sample and color filters, where the laser central wavelength is tuned from 780 to 920 nm in steps of 30 nm. The pulse bandwidth at 810 nm is around 30 nm and the pulse spectrum follows a Gaussian shape. Figure 5.7b then shows the corresponding spectrum of the collected SHG generation from β-BBO, showing the expected frequency doubling. The SHG spectrum at 395 nm is clipped by a bandpass filter around 400 nm. In order to assure that the collected signal indeed originates from SHG, a second requirement that needs to be verified is a quadratic dependence of the signal on the input power. Filtering the scattered signal using a bandpass filter around 400 nm (FB400-40, Thorlabs) and varying the laser input power from 10 μW to 10 mW we collect between 10^5 and 10^{11} photons per second on the camera. Figure 5.8 shows this data on a log log scale with the camera exposure time indicated in the legend. Fitting a straight line to the data finds a slope of 1.99, confirming the quadratic power dependence in this range of input powers.

Finally, we verify in a third calibration measurement that it is possible to collect a SHG interferometric autocorrelation in our setup. Figure 5.9 shows in orange an example trace measured as a function of delay τ, with fundamental wavelength 820 nm and 1.3 mW incident power. With the background

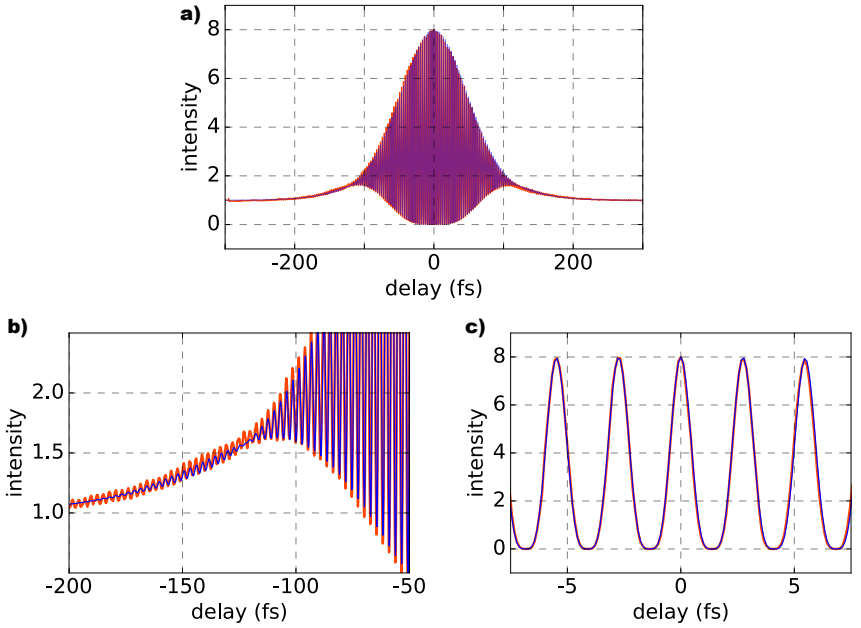

Figure 5.9: a) IAC trace of SHG generated in BBO as a function of mutual pulse delay τ, data in orange, fit in blue. At $\pm$ 50-200 fs the chirp signature of the incoming pulses shows in wing-like behavior (i.e. fringe minima exceed 1). b) The fit is observed to also match the oscillations in the wings. From the fit we retrieve an incoming pulse width of 110 fs and 4750 fs^2 chirp. c) Zoom around $\tau = 0$ shows that we resolve individual oscillations.

normalized to 1, it shows the typical IAC characteristics for a chirped pulse: at $\tau = 0$ the fringes reach a maximum value of 8, and at the tails of the trace (at $\pm$120 fs) the fringes are entirely above 1. This measurement can be directly used to characterize the femtosecond laser emission. In order to retrieve the pulse length (parameter Δt in Eq. (5.1)) and second order spectral chirp (parameter $\phi^{(2)}(\omega)$ in Eq. (5.2)) this trace is fitted to a theoretical pulse on two assumptions: (1) that its amplitude follows a Gaussian lineshape and (2) that there are no contributions to the spectral phase of order 3 and higher. The procedure for this characterization is described in section 5.3.3. Fig. 5.9 shows the fit in blue. We retrieve our pulses to be of 110 fs length, while containing 4750 fs^2 of chirp (at the laser fundamental, 820 nm, the laser bandwidth is 22 nm, yielding a bandwith limited pulse length of 46 fs). Fig. 5.9b plots a zoom on one of the wings, demonstrating that also at longer delay and at smaller intensity all the fringes are fitted. The zoom of the center fringes in Fig. 5.9c shows perfect overlap of the fit and the measured data. We verified that *increasing* the chirp in the beam using the built-in compressor in

the laser shows increased chirp signatures (wings) in IAC traces (not shown here). Conversely, adjusting the compressor settings such as to reach the shortest pulses possible in the focus of the objective, we could reduce the pulse length to around 100 fs, but could not completely precompensate the chirp that is added by the optical components between compressor and sample. This puts no constraint on the IAC method itself to interrogate antennas, as it will always be necessary to perform a reference IAC measurement to retrieve the initial pulse length and chirp, alongside measurements on the photonic system of interest. While not *in principle* a constraint, *in practice*, shorter pulses at the antenna would be advantageous due to the short expected ringdown times of plasmonic resonances. To obtain such shorter pulses an SLM-based pulse shaper and iterative pulse shaping algorithm would be required, as demonstrated by Accanto et al. [104].

5.5 SHG and IAC traces from Au antennas

5.5.1 Signal in SHG wavelength-band, power dependence

Having shown that our setup is in principle able to trace an autocorrelation at 0.1 fs delay resolution (dictated by the cutting angle and displacement of the wedges in the delay line, described in section 5.3.1), we next investigate whether we are able to collect sufficient signal from arrays of nanoscale resonant systems. Figure 5.10a shows an example SEM image of the Au nanorods studied (length 140 nm, pitch 270 nm). A white light transmission spectrum of the sample is shown in Figure 5.10b, showing resonances between 720 and 840 nm that redshift upon increasing nanorod aspect ratio. Following the procedure described for BBO, one ideally evidences SHG by measuring the generated nonlinear spectrum using adequate blocking of the fundamental

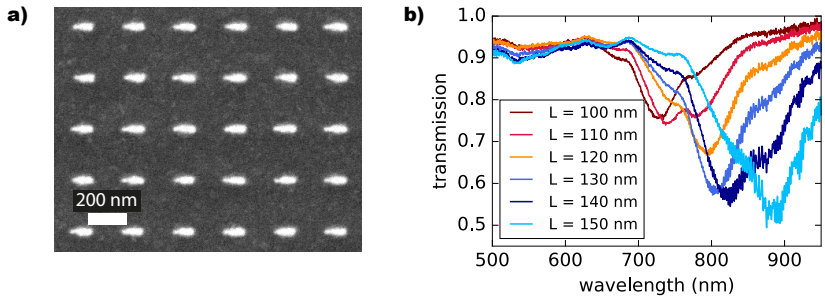

Figure 5.10: a) SEM imags of Au nanorods with one sharp end on glass fabricated using e-beam lithography, of 140 nm length and 270 nm pitch. After SEM imaging the samples were covered in a 150 nm layer SiO_x to allow the use of both air and oil objectives. b) Transmission spectra of the nanorods of lengths indicated.

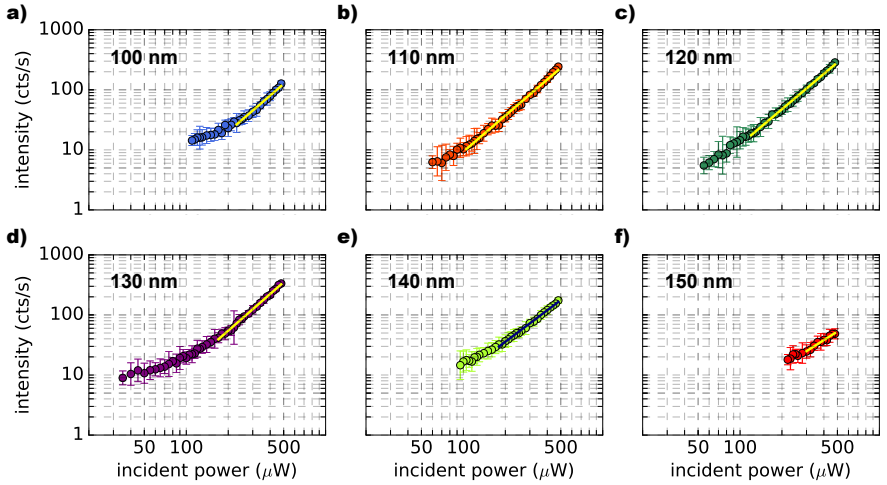

Figure 5.11: SHG generation in Au nanorod arrays as a function of incident power, for various rod lengths as indicated. Note the log scale on both axes. The signal was collected on an APD with temporal gating using a bandpass filter around 400 nm. Yellow (or navy) lines are a fit trough part of the data with slopes of 1.99, 1.99, 1.95, 2.03, 1.74 and 1.47 for a) to f), demonstrating a square power dependence for 110, 120 and 130 nm length.

beam. Unfortunately, using a filter that only transmits in a 40 nm window around 400 nm the maximally achievable count rate (incoming wavelength fixed at 790 nm) is only a few hundred counts per second on our APD detection, and not sufficient to collect spectra systematically as function of fundamental wavelength.

Without a spectrum to confirm SHG from plasmonic nanorods, we must rely on input-output measurements to test for a quadratic power dependence. This measurement gives insight in the origin of the signal detected and delineates the input power range in which an interferometric autocorrelation measurement should be executed. Figure 5.11 plots for a range of nanorod lengths as a function of input power the nonlinear signal, filtered around the SHG wavelength, collected on the APD. We use slightly defocused excitation in order to collect signal from multiple antennas (on the order of 500). Compared to BBO, Au nanorods require a much higher input power before signal is collected. At incident power 300 μW, BBO emits on the order of 10^7 counts/s, while Au provides of order 250 counts/s. The 5 orders of magnitude difference is not very surprising, given the three orders of magnitude difference in dimensions (Au nanorods are just 40 nm in height versus 10 μm of BBO) and the difference in nonlinear conversion efficiency between the two materials.

In the range up to 500 μW input power, the maximum count rate for the

presented set of measurements is 300 counts/s, detected using nanorods of length 130 nm (Figure 5.11d). From Figure 5.10b (Au nanorod transmission plot) we take that this is the geometry which has its resonance wavelength at 800 nm, roughly coincident with the fundamental laser wavelength. The nonlinear conversion efficiency is highest when the particle plasmon resonance and the excitation coincide. For the highest input powers the signal of the L = 130 nm antenna design depends quadratically on input, with a slope taking a value of 2.03. At the lower power end, the curve flattens. For the other designs, a similar second order power dependence at the high input regime is present for the shorter lengths of 100, 110 and 120 nm, yet not for the rods on the red side of the resonance (140 and 150 nm).

All together, figure 5.11 clearly shows that in contrast to the case of BBO, the slope as a function of input power is generally not constant. This makes it difficult or even impossible to determine the appropriate power at which to perform an IAC trace, as IAC strictly requires a quadratic power dependence over the power. Figure 5.11 demonstrates that each antenna field requires a *different* minimum power at which to perform IAC, which for systematically collecting autocorrelations on a larger set of designs simultaneously is troublesome. Conversely, each sample also has a maximum admissable power, as we will show in the next section.

5.5.2 Signal stability and sample damage

The low signal levels would suggest to increase the pump power levels beyond those in Figure 5.11. Here we are disadvantaged by the relatively low repetition rate of our laser system of 1 MHz, as opposed to the 80 MHz that is typically used in modelocked lasers. We have found that intensities in the range of 60-1200 W/cm^2 (using excitation powers between 5 and 100 μW

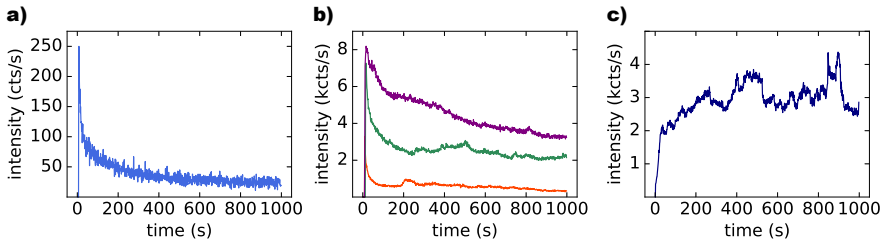

Figure 5.12: Time evolution traces for the SHG signal emitted by arrays of Au nanorods of various lengths. a) 100 nm, with a central resonance (see Fig. 5.10b) blue shifted with respect to the incoming laser at 790 nm. After initial fast decay the signal stabilizes. b) 110, 120 and 130 nm rods (orange, green and purple respectively). With increasing rod length, the decay takes longer. c) 140 nm rods, redshifted form the incident beam, show different behavior compared to a) and b): the signal increases over time.

and an approximately 3 μm diameter focussed excitation spot, corresponding to pulse peak intensities of order 0.6-12 GW/cm^2) may damage the sample, which we attribute to particle deformation [247]. Figure 5.12 shows example traces of the nonlinear signal emitted by plasmonic nanorods of different lengths over the course of 20 minutes, excited at 790 nm and a power between 5 and 100 μW. Antennas on the blue (100 nm) and red (140 nm) side of the laser wavelength clearly show different behavior, suggesting a thermally induced reshaping of the particles that removes asperities and by rounding may blueshift the resonance. Regardless of the exact mechanisms, the illustrated signal variation is highly impractical. For the IAC measurements presented below, we chose powers up to the maximum values permissable according to Fig. 5.11, and first exposed the sample for 10 minutes so that at least the initial rapid decay, seen in Fig 5.12a, could be prevented.

While the power dependence measurements presented in Fig 5.11 were performed using a slightly defocussed excitation illumination of order 500 nanorods while not exceeding 500 μW, Figure 5.13 cautions strongly against using higher power densities. Data in Figure 5.13 was obtained by tight focusing (compared to Fig. 5.11). Nanorods of all lengths, even if exhibiting second order dependence on input power at modest excitation density, can emit at any slope between 1.6 and as high as 4.1. A slope exceeding 2 indicates higher order processes. Also, thermal emission of Au may contribute in the selected spectral window that collects around the second harmonic frequency.

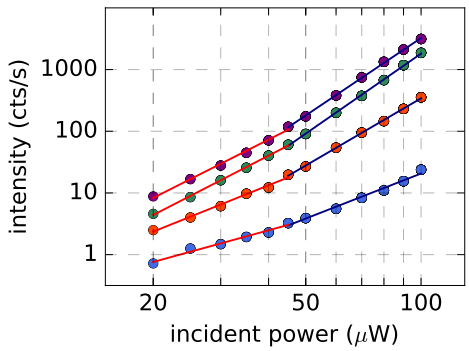

Figure 5.13: Power dependence measurements at higher incident powers compared to Fig. 5.11 by increasing the focus of the excitation spot. Note a log scale on both axes. Colors represent different nanorod lengths: blue, orange, green and purple for 100, 110, 120 and 130 nm respectively. For the smallest rod, the fitted slope at lower (20 - 45 μW) and higher powers (45 - 100 μW) are 1.71 and 2.42, while all other fitted slopes exceed 2.5, with 3.14 and 4.17 for the case of 130 nm rod length. These numbers are a clear indication of nonlinear processes of higher orders than 2.

5.5.3 IAC traces from Au nanorod emission

Having to carefully select an input power range between a non-quadratic power dependence at the low power end and particle damage and possible higher order processes at the higher end is not a very robust or repeatable procedure to execute an autocorrelation measurement. It may however still be illustrative to show some of the collected traces. We selected the geometry that shows the strongest nonlinear enhancement (L = 130 nm) and measure IAC traces using different incident intensity. The results are shown in Figure 5.14. Fig. 5.14a shows the trace collected using an incident power of 345 μW and defocused excitation, at which Figure 5.11 has shown a slope of 2, whereas Fig. 5.14b is measured using 400 μW and using only slightly defocused excitation such that the measurement exceeds the quadratic power dependency regime. Taking such traces takes of order one day due to the long integration time per point needed. The overall IAC shape of the two traces is similar to that obtained from BBO, with wings from 90 to 150 fs that point at chirp. The most remarkable features in these plots is that the background to peak ratios of 1:8 are not attained. The root cause of this deviation in IAC ratio is that the power dependence presented in Figure 5.11 is not strictly quadratic over a sufficient dynamic range. Figure 5.14b shows the extreme effects of *exceeding* this range. With the background normalized to 1, the IAC peak now reaches almost 16 at high power, due to the higher order nonlinear processes. Unfortunately, for both cases presented in Fig. 5.14 a fit procedure to extract parameters of these pulses, or its reshaping by the nanorod is pointless, as the 1:8 ratio is not an adjustable parameter.

An important warning is that IAC peak values may in an experiment even appear to *systematically* vary with detuning between pump laser wavelength and plasmonic resonance, as a consequence of the strong geometry depen-

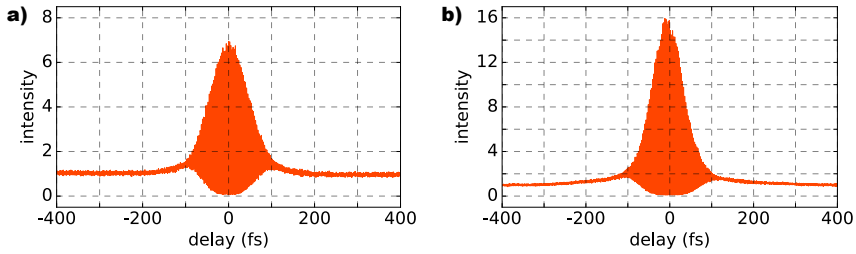

Figure 5.14: IAC traces measured on 130 nm length nanorod arrays, collected on the APD using a 100x oil objective. a) 345 μW excitation power used, 10 s acquisition time per datapoint. b) 400 μW excitation power and 5 s integration time. While a) is measured with defocused excitation to have second order power dependence on input power, b) is focused more and is therefore outside of this regime. As a result, in b) the background to peak ratio reaches 1:16.

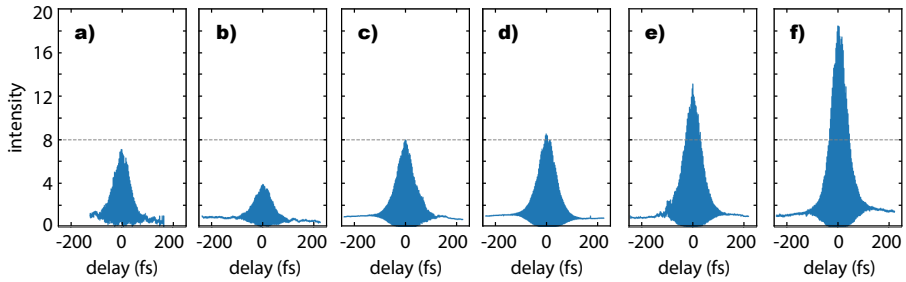

Figure 5.15: Interferometric autocorrelations from a test sample of Au nanorods embedded in SiO_x (symmetrical rods and 300×400 nm pitch, otherwise identical to the Au nanorod sample presented in Fig. 5.10) of length 110 to 160 nm in steps of 10 nm. We used a fundamental wavelength of 794 nm, 1.5 μW incident power, very tight focussing (1 μm spot diameter), integration times between 2 and 3 s, and a 100x oil objective to collect SHG on the camera. It shows that under constant excitation conditions any peak to background ratio can be obtained.

dence of these higher order emission phenomena. This is illustrated in Figure 5.15, which shows IAC traces collected from gold nanorods increasing in length from 110 to 160 nm. The geometry with its resonance closest to the fundamental (panel d) shows a 1:8 ratio, while the other designs show the wide range that one might encounter.

5.5.4 Discussion

To summarize, we attempted to use gold nanorods as nonlinear nanoprobes for the local field dynamics, and encountered several issues. Most importantly, the overall low count rate hinders measuring an emission spectrum and additionally requires very long integration times. As a result, acquiring reasonable IAC traces currently takes up to an entire day of continuous scanning, a time scale at which the variation in laser power starts to be problematic (it varies 20-40% over several hours). Even under these circumstances, it is unclear if the IACs are actually trustworthy, in the sense that the blue emission of the gold nanorods can not be uniquely attributed to SHG. Simply increasing pump power destabilizes the nonlinear signal, possibly due to nanoparticle reshaping. At intermediate excitation powers we do manage to measure the required second order dependence on input power, however only in a narrow power range before higher order processes kick in. These problems are fundamental to the weak SHG of Au antennas, although increasing the repetition rate of the experiment (currently 1 MHz) may help to some extent, as it allows at the same instantaneous power densities to gather up to 100x more signal intensity. Necessary conditions for the collection of IAC traces are thus to obtain a strong and stable signal that furthermore has to depend quadratically on input power.

5.6 TPEL assisted by resonant plasmonics and IAC

5.6.1 TPEL from CdSe dots

The theoretical analysis in section 5.2.5 has shown that TPEL should produce exactly the same IAC trace as SHG. Therefore, using TPEL instead of SHG may be a simple and effective strategy to probe nanoparticle near fields. As TPEL sources we use CdSe/CdS/ZnS (core/shell/shell) quantum dots, as quantum dots are known for high two photon absorption. We first spectrally verify TPEL emission from the bare quantum dots on glass, followed by a power dependence measurement. Then we present the main results of this chapter, i.e., quantum dot two-photon excited luminescence enhanced by the local fields of resonant metal nanoparticles.

Figure 5.16 plots the emission spectrum of two-photon excited luminescence of a monolayer of bare quantum dots on a glass slide (deposition details presented in the Methods section), for laser excitation wavelengths 790 to 910 nm. We focus the light on the sample using a lens and collect the transmission using the 20x objective (Plan Fluor, NA 0.5, Nikon). It is evident that TPEL does not depend on the excitation wavelength. The clipping at 650 nm is due to the two 650 nm shortpass filters that block the pump beam.

Figure 5.17 plots as a function of incidence power the TPEL signal collected on the camera, for various excitation wavelengths, and adjusting the integration time to scan a large incident power range. We detect three orders of magnitude more signal in comparison with SHG from Au antennas. At 500 μW incidence power we collect on the order of 10^5 counts per second. While in the case of gold the signal had to be collected with an APD, assisted by temporal gating, the TPEL signal is easily captured using the camera. Compared to the second harmonic signal measured using bulk BBO, we detect 3 orders of

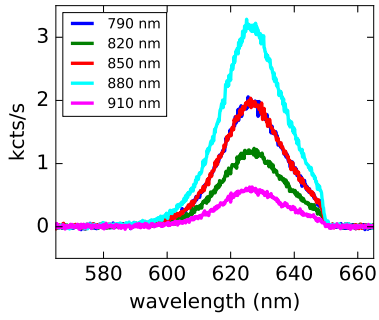

Figure 5.16: TPEL spectrum of bare quantum dots for a range of excitation wavelengths between 790 nm and 910 nm. Input power was 15 mW, corresponding to a power density of 3 kW/cm^2 (or 30 GW/cm^2 peak power density). Two shortpassfilters at 650 nm are used to block any residual from the laser.

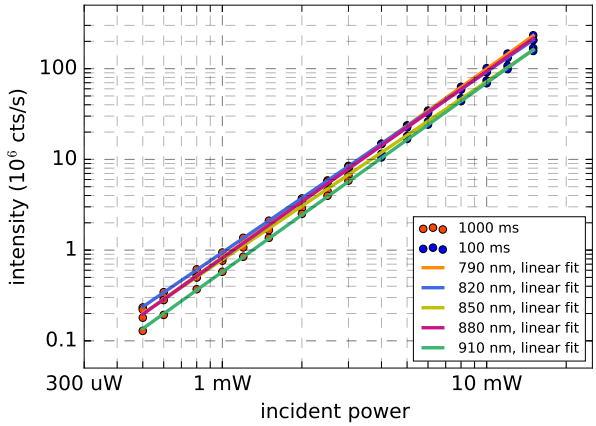

Figure 5.17: TPEL emission from a monolayer of quantum dots on glass as a function of incident power at various fundamental wavelengths, collected on the camera. Both axes show a log scale. Straight lines show a fit through the data for each fundamental, with retrieved slopes of 2.08, 1.99, 1.96, 2.06 and 2.08 in order of increasing fundamental, showing excellent quadratic dependence on input power for all excitation wavelengths.

magnitude less (10^5 versus 10^8 counts per second), at similar input power. We measured the thickness of our layer to be 17 nm (a monolayer). Comparing this to the three order of magnitude thicker BBO (10 μm), the efficiencies of BBO and the quantum dots are very similar. A linear fit to the input-output data in a log log plot yields slopes very close to the expected value of 2. The fact that we easily obtain a very stable and high signal which additionally depends exactly quadratically on input power, makes TPEL of these quantum dots very promising.

5.6.2 TPEL from Au nanorod systems

With quantum dots on glass generating substantial signal we continue to investigate whether their emission can be used as probe of the local field enhancement of a nanoantenna. As antennas we first used lithographic Au nanoparticles with a resonance in the range of the fundamental laser beam (L = 80 - 160 nm), also varying the array pitch from 350 to 400 nm. Fig. 5.18a shows a schematic side view of the TPEL system studied. The sample was excited at 790 nm and TPEL signal was collected in transmission. Fig. 5.18b plots the measured TPEL signal collected on the camera using an integration time of 1 s (strongly defocussed excitation to fill the field of view), displaying the response of the different array pitches and antenna lengths that were fabricated. Resonant effects both in particle length and array pitch are ap-

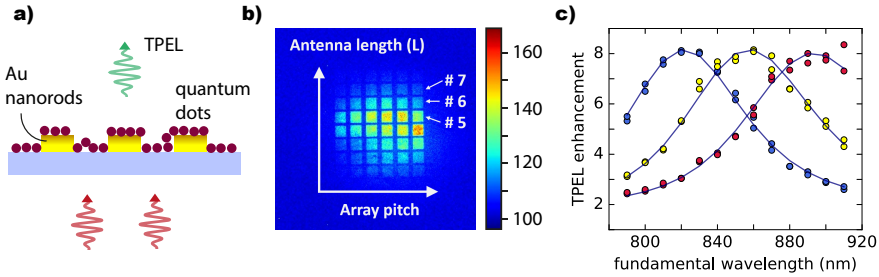

Figure 5.18: a) Sideview sketch of the nanoplasmonic TPEL system studied. The fabricated nanoparticles are covered in a monolayer of quantum dots (17 nm). b) TPEL image showing bright emission of plasmonic nanorod arrays of variable geometrical parameters (length varying from 80 to 180 nm and pitch varying from 350 to 400 nm), excited using a 790 nm wavelength pulsed laser. Numbers on the color scale correspond to counts per pixel on the CCD camera. c) Excitation spectra of three selected arrays. The points show experimental data, obtained by tuning the incident wavelength from 790 to 910 nm. The lines are a common theoretical fit.

parent. Fig. 5.18c shows for three selected fields the integrated signal over each field, normalized to the rectangular reference region immediately left of it (i.e. between the selected field and the neighboring field), as a function of the fundamental laser wavelength. The quantum dot TPEL is boosted by up to eightfold by the presence of the nanorods. Given that TPEL itself is not dependent on the fundamental frequency, the Lorentzian lineshape in each array directly shows the resonance of the antenna array itself. In order words, we can trace the Au antenna resonances by measuring quantum dot TPEL enhancement as a function of excitation wavelength.

Having evidenced bright TPEL from quantum dot emitters, enhanced by the pump field near field enhancement of plasmonic resonances, we present interferometric autocorrelation traces in Figure 5.19. The normalized TPEL as a function of scanned delay τ shows very elegant IAC traces: the background is flat and the envelope is highly symmetric. These observations apply to both the bare quantum dots (a) and the quantum dots covering nanoplasmonic Au particles (b). By eye, the two traces are barely distinguishable, meaning that the Au nanoantennnas in this example do not provide a strong pulse reshaping. We attribute this to the low Q of the antennas at hand (Q=15) according to Fig. 5.18c, which corresponds to a ring down time ten times faster than the pulse duration.

5.6.3 TPEL from higher Q Ag systems

To increase the TPEL enhancement contrast and obtain a higher Q, we adjusted the nanorod lattice design in two ways. Regarding material composition, we switched from Au to Ag as the latter has lower Ohmic losses. In

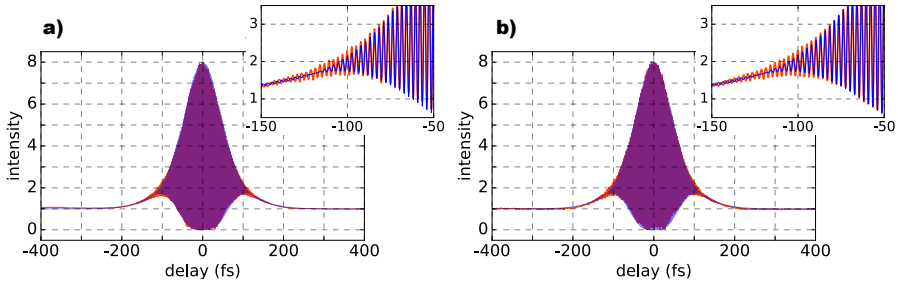

Figure 5.19: Interferometric autocorrelation traces of TPEL from a monolayer of quantum dots, a) on bare glass and b) on top of Au nanorods (array number 4 in Figure 5.18). Both panels show experimental data in orange and theoretically fitted curves in blue. The inset is a zoom on the left wing to show individual fringes.

addition we explored a plethora of lattice geometries, mainly focused at packing more antennas on the same surface to get more quantum dots excited by the near-field of antennas, while maintaining the periodicity that could support lattice resonances around the fundamental wavelength. As this chapter reports a work in progress, we have not systematically categorized the response of all fabricated lattices, and instead provide results on one lattice that illustrates (i) enhancement factors up to 70x and (ii) very clear effects on IAC traces. The results at hand were obtained on lattices where nanorods were placed in 4×4 groups with a 25 nm gap between all particle edges. These groups are placed in a square lattice with a pitch varying from 500 to 600 nm. An SEM image of this design in shown in Figure 5.20a. Figure 5.20b shows one of the other designs as an example (same parameters as a), yet in groups of 2×2. Figure 5.21 shows the TPEL enhancement induced by the Ag nanoparticles as a function of laser excitation wavelength for a set of geometries, with antenna length varying between 75 and 90 (rows) and pitches 520, 530 and 540 nm (columns). Compared to the isolated Au nanorods, the TPEL enhancement is increased always at least a factor 2, and up to 70-fold. The resonances arise from an interplay of diffractive resonances (narrow, Rayleigh anomaly for diffraction into glass expected at 830 to 840 nm wavelength) and the broad (hybridized) single particle resonances. The highest TPEL enhancement we have observed was over 175-fold, shown in Figure 5.21m, for a design with 2×2 instead of 4×4 antennas.

Finally, we used the TPEL emitted by quantum dots in the near field of these Ag nanorod systems to systematically collect interferometric autocorrelations traces. Since we collect signal by collecting at each time delay τ an image on the camera we can simultaneously collect data for up to 100 distinct plasmonic array designs. A set of 8000 camera images is collected for a fixed excitation wavelength, and we integrate the number of counts over a set of pixels within one field to plot the IAC as a function of τ. A spatially

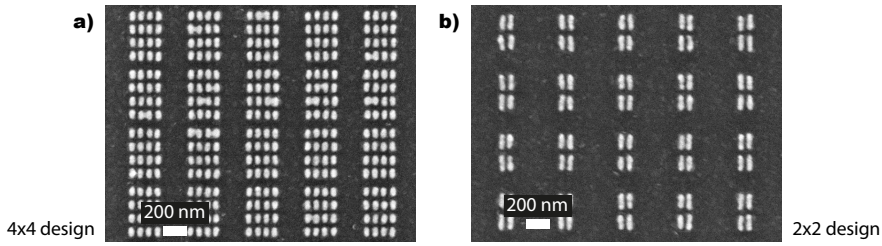

Figure 5.20: SEM images of the Ag nanorods on glass before quantum dot deposition. a) Rods are in positioned in a rectangular 4×4 lattice, in a larger square lattice. Shown here are 90 nm rod length and 500 nm array pitch. b) Rods in a 2×2 design, shown here are 150 nm length and 500 nm array pitch.

resolved reference scan is captured by collecting a second set of camera images after moving the illumination spot to a region with just quantum dots and no antennas, in order to compensate for illumination variations that depend on the exact position within the illumination spot. A set of 12 example IAC traces, taken from the 4×4 nanorods design, is shown in Figure 5.22 using excitation wavelength 850 nm, as a function of nanorod length (rows) and array pitch (columns). Each figure is accompanied by a zoom to make the differences in terms of wing height and onset of oscillations more explicit. To begin we notice the expected background to peak ratio of 1:8 in all cases. Also the familiar chirp signatures around ±100 fs are present for all geometries shown, which is expected given that our reference measurement already showed the pulse to be chirped when arriving at the sample.

Next we turn to the differences in this subset. Upon closer examination of the wings we first notice that in some instances the oscillations uninterruptedly span over a more than 400 fs range with a high amplitude in the wings, as for example in (b). Qualitatively, the total range over which these oscillations are visible is even wider than for the case of solely quantum dots (compare to Fig. 5.19a). This large span of oscillations is quite distinct from some other cases, where the onset of the oscillations that grow to the large envelope is only at ±150 fs or ±120 fs (j and l respectively) without visible fringes at larger (negative) delay. Furthermore, in some traces we also note that the oscillations disappear at select timepoints (most clearly seen in f, h and i). Finally the height of the wing 'shoulder' (the clearest sign of chirp) is rather high for rod length 75 nm, especially in (c), then lowers for lengths 80 and 85, and increases again for the longest rods (j-l).

While the differences are subtle, we argue that these differences in IAC wings arise from the plasmonic resonances in the system. In IAC each of the wings reveals interference between two pulse copies at 100 - 200 fs delay, which effectively means that it carries information on the overlap between the front and the back of the pulse. Qualitatively, one would expect the onset

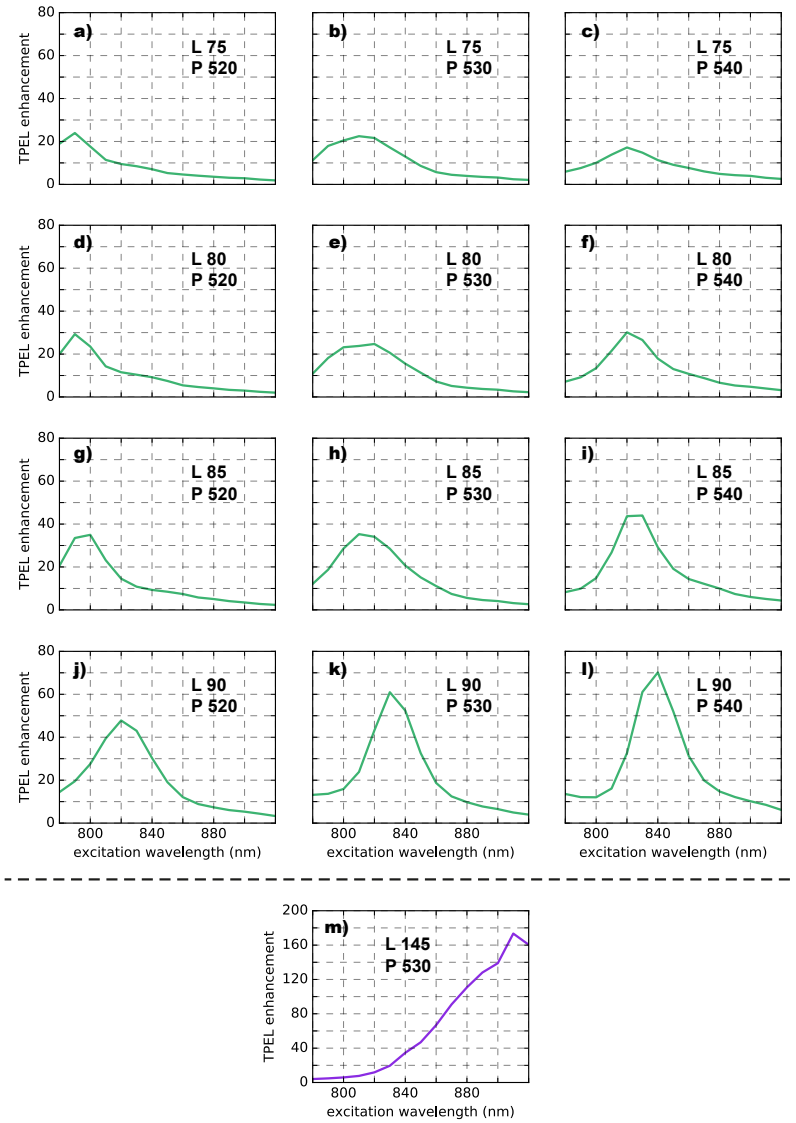

Figure 5.21: a-l) Example excitation spectra of TPEL enhancement from quantum dots on arrays of Ag nanorods (the 4×4 unit cell design), as a function of excitation wavelength and for various rod lengths and array pitches as indicated. The resonance peaks systematically redshift both upon increase in nanorod length and array pitch. Regarding pitch, the widest resonance (lowest Q) in this subset is at 530 nm pitch. However, the differences in this range of pitches is very minor, therefore the variation in Q does not consistently translate to the corresponding IAC traces (shown in Fig. 5.22). TPEL enhancement significantly increases with nanorod length, in this subset taking values up to 70. m) TPEL enhancement obtained from the 2×2 design (SEM image shown in Fig. 5.20b), reaching a factor 175.

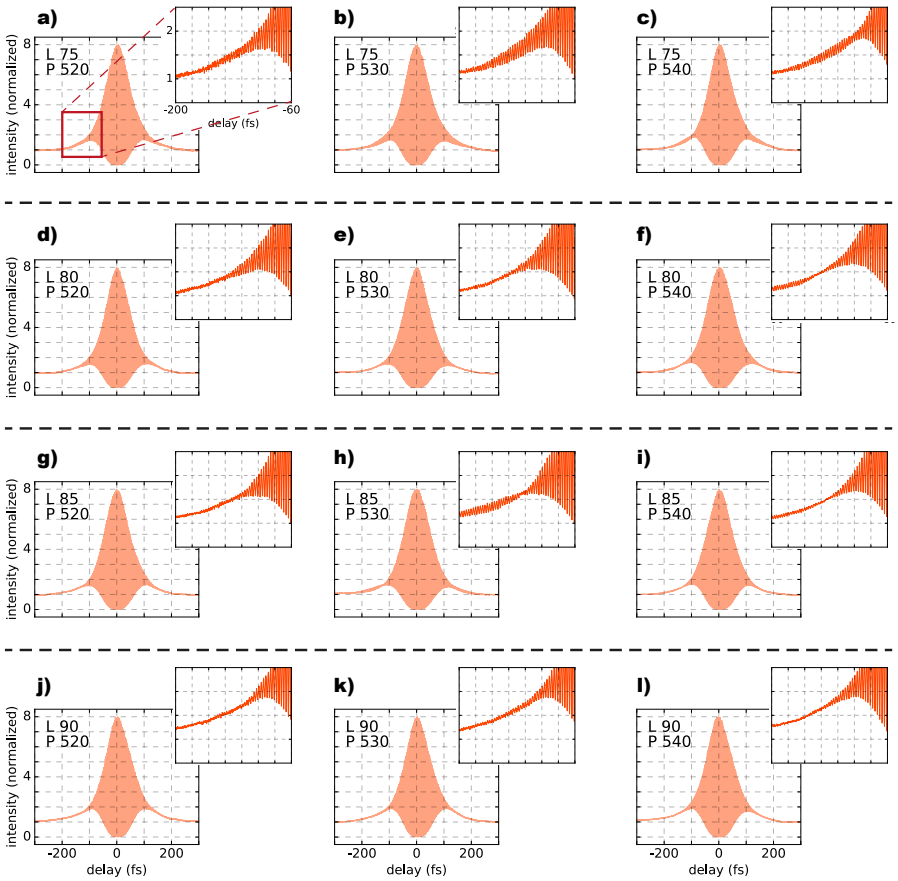

Figure 5.22: TPEL IAC traces from quantum dot emission enhanced by Ag nanoparticle near fields (4×4 design as in Fig. 5.20), corresponding to the excitation spectra shown in Fig. 5.16. Excitation wavelength 850 nm. Rows plot increasing rod length whereas columns plot increasing array pitch, as indicated. Each trace includes a zoom with axis labels as indicated in inset in a). While the full IAC traces all look quite similar, their widths do vary, and the enlarged plots visualize additional subtle differences in the height of the wings and the extend of the oscillations. Notice e.g. the clear difference between case b) and g) (extend of oscillations) and c) and g) (wing height).

of interference at larger $\pm\tau$) for higher-Q resonances, that take longer to ring down (compare Fig. 5.21b, lower Q, to for example j,l). Moreover, the resonant near-field induced in the antennas may have a reshaped spectrum compared to the incident laser pulse, affecting the fringe contrast, and possibly giving rise to the beating phenomena. However, quantitatively retrieving field characteristics from correlation measurements is a very difficult problem, as it is not possible by a straightforward deconvolution. To properly draw conclusions it is therefore necessary to fit the traces to theoretically calculated fields, using the pulse length and chirp of the original incoming field as a starting point, and a model response for the antenna system. While this procedure due to time constraint is outside the scope of this thesis, it remains ongoing work in our group.

Prospect of single nanoparticle use for TPEL for IAC

As mentioned in the beginning of this chapter, we designed the setup to ultimately collect IAC traces from even single nanoparticles. To demonstrate that this is possible at least from a signal strength point of view using TPEL, we prepared samples with a layer of the strongly fluorescent dye rhodamine 6G, covered with sparsely distributed colloidally fabricated Ag nanocubes (80 nm in size, supplied by coworkers, synthesized by seeded growth in solution) for local field enhancement. Such nanocube systems have gained prominence in the plasmonics community since the observation by the group of Mikkelsen that nanocube gap antennas provide exceptionally high Purcell factors and field enhancements [47]. Figure 5.23a shows a sketch of this sample. For IAC measurements the excitation wavelength was 790 nm and the emitted TPEL was collected using a 100x objective (0.9 numerical aperture) on the camera with 100 ms integration time. An example camera image is shown in Figure 5.23b and the measured IAC trace is shown in Figure 5.23c. A

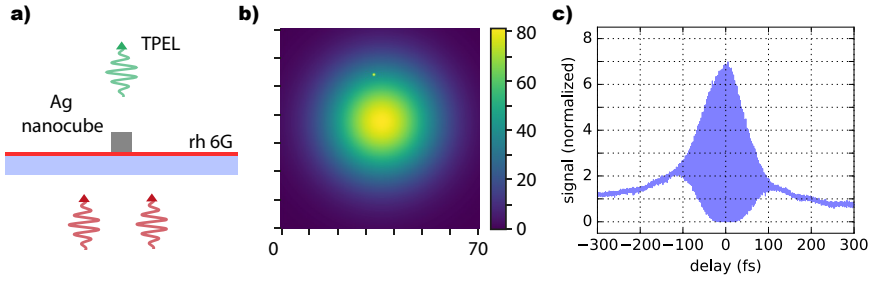

Figure 5.23: a) Sketch of a Ag nanocube on a layer of fluorescent rhodamine 6G. b) TPEL emission collected on the camera, the particle is visible above the focus spot. c) Interferometric autocorrelation trace of TPEL from rhodamine 6G, enhanced by the nanoparticle.

background to peak ratio of 1:8 is not achieved, yet it is promising that we are able to collect IAC traces from, very likely, a single nanoparticle.

5.7 Conclusion and outlook

In this chapter we demonstrated a common path nonlinear setup that collects SHG and TPEL from the focus of an objective and measures interferometric autocorrelation (IAC) traces as a function of time delay. The IAC on non-resonant material simply carries information on the incoming pulse duration and chirp. In addition, the interaction between ultrashort pulses and resonant plasmonic nanoscale objects will be imprinted on the plasmonic local field, which in the case of nonlinearly responding material can in turn be used as the nonlinear source for the interferometric autocorrelation. In that case the IAC also contains information on the local field, i.e. the incoming field convoluted with the time domain response function of the plasmonic resonance. In this chapter we demonstrated the experimental conditions that are required to perform autocorrelation measurements.

Using SHG in β-BBO, we characterized our fs pulses to be 110 fs in length and carry 4750 fs^2 chirp at the sample plane of our setup. Next we spectrally characterized SHG from Au nanoparticles and TPEL from quantum dots, and confirmed a second order dependence on input power, as is required for an interferometric autocorrelation. We initially attempted to employ Au nanorod arrays as a platform to investigate the local field dynamics through SHG-based IAC. Mainly due to low count rate, concomitant sample damage thresholds, and non-quadratic emission processes, retrieving IAC traces is subject to artefacts. We then decided to turn to two-photon excited luminescence (TPEL) from quantum dots, which is very bright, stable, and shows a quadratic power dependence. With quantum dots covering arrays of Au nanoparticles we reach TPEL enhancement of a factor 8, whereas using Ag nanoparticle arrays with a 4×4 unit cell boosts this enhancement above 70. We collected IAC traces for a range of pitches, nanorod lengths and unit cell designs, of which a subset is presented. We show that the variation in the plasmonic lattice (in rod length and pitch) underlying the quantum dot emitters is directly translated to the IAC, of which the quantitative analysis is an ongoing study.

As recommendation for future work, in order to measure interferometric autocorrelations of nanoscale samples in the focus of an objective it is indispensable that, apart from having a stable signal, one i) explicitly verifies the emission spectrum and its stability, ii) one assures that the signal depends quadratically on input power, and iii) one verifies the 1:8 background to peak ratio in IAC. All these criteria are of course more easily verified, the higher the signal. Implementing a multi-pass layout in the optics to effectively increase the repetition rate, or choosing a higher repetition rate laser could alleviate these issues, as can using TPEL instead of SHG. An important problem in our

work is that the 70 fs pulses from our laser are at the sample plane already elongated to 110 fs, and chirped, due to dispersion in the optics towards the sample. As the final plasmonic signature is a nonlinear function of the plasmon response function convoluted with the incident pulse, this pulse lengthening obscures the generally low-Q plasmonic response. A recommendation for setup improvement is to include a spatial light modulator-based pulse shaper to precompensate for pulse distortion. Here one would optimize the spectral phase imposed by the spatial light-modulator to obtain the shortest reference IAC, as e.g. in [104].

The imprint of plasmonic temporal dynamics on IAC traces is best questioned employing non-resonant emitters such as used in this work, and seems to be especially apparent for the case of narrower resonances. The ability to probe local field dynamics at femtosecond to picosecond timescales opens up interesting possibilities in 'high-Q plasmonics'. Here one should realize that for linear far field observables, i.e. far field differential scattering cross sections, transmission and reflection, there is in principle no benefit in using ultrafast techniques over simple continuous wave spectroscopy and interferometry. Indeed, linearity implies equivalence of results through Fourier transform. However, in studying dark modes, as well as in studying plasmon etalon resonances like those in chapters 2, 3 and 4 of this work a main interest is in understanding the near field characteristics. This requires a local reporter, such as local nonlinearity that transduces near field at the fundamental frequency to an observable far field at another frequency. Another domain where the techniques may be useful is in developing nonlinear plasmonic devices. Here one could envision ultrafast control over the properties of a plasmonic antenna or hybrid plasmonic-photonic resonance that are switched by a pump beam, and that change the response of a system during its interaction with a probe pulse.

References

[1] Z. Liu, L. D. Lavis, and E. Betzig, *Imaging live-cell dynamics and structure at the single-molecule level*, Mol. Cell **58**, 644 (2015).

[2] C. K. Kao, *Sand from centuries past: send future voices fast. Nobel lecture, december 2009*, URL `https://www.nobelprize.org/prizes/physics/2009/summary/`.

[3] W. Wang, J. Feng, Y. Ye, F. Lyu, Y. Liu, J. Guo, and Y. Yin, *Photocatalytic color switching of transition metal hexacyanometalate nanoparticles for high-performance light-printable rewritable paper*, Nano Lett. **17**, 755 (2017).

[4] A. Polman, M. Knight, E. Garnett, B. Ehrler, and W. C. Sinke, *Photovoltaic materials: Present efficiencies and future challenges*, Science **352** (2016).

[5] I. El-Sayed, X. Huang, and M. El-Sayed, *Surface plasmon resonance scattering and absorption of anti-EGFR antibody conjugated gold nanoparticles in cancer diagnostics: applications in oral cancer*, Nano Lett. **5**, 829 (2005).

[6] M. R. K. Ali, Y. Wu, Y. Tang, H. Xiao, K. Chen, T. Han, R. W. N. Fang and, and M. A. El-Sayed, *Targeting cancer cell integrins using gold nanorods in photothermal therapy inhibits migration through affecting cytoskeletal proteins*, PNAS **114**, 5655 (2017).

[7] D. W. Vernooy, V. S. Ilchenko, H. Mabuchi, E. W. Streed, and H. J. Kimble, *High-Q measurements of fused-silica microspheres in the near infrared*, Opt. Lett. **23**, 247 (1998).

[8] K. J. Vahala, *Optical microcavities*, Nature **424**, 839 (2003).

[9] M. Pelton, *Modified spontaneous emission in nanophotonic structures*, Nat. Photonics **9**, 427 (2015).

[10] E. Abbe, *Beiträge zur Theorie des Mikroskops und der mikroskopischen Wahrnehmung*, Archiv für Mikroskopische Anatomie **9**, 413 (1873).

[11] B. Lounis, and M. Orrit, *Single-photon sources*, Rep. Prog. Phys. **68**, 1129 (2005).

[12] H. Mabuchi, and A. Doherty, *Cavity quantum electrodynamics: Coherence in context*, Science **298**, 1372 (2002).

[13] H. Walther, B. T. H. Varcoe, B. Englert, and T. Becker, *Cavity quantum electrodynamics*, Rep. Prog. Phys. **69**, 1325 (2006).

[14] J. M. Raimond, M. Brune, and S. Haroche, *Colloquium: Manipulating quantum entanglement with atoms and photons in a cavity*, Rev. Mod. Phys. **73**, 565 (2001).

[15] A. Reiserer, and G. Rempe, *Cavity-based quantum networks with single atoms and optical photons*, Rev. Mod. Phys. **87**, 1379 (2015).

[16] M. D. Eisamana, J. Fan, A. Migdall, and S. V. Polyakov, *Invited review article: Single-photon sources and detectors*, Rev. Sci. Instrum. **82**, 071101 (2011).

[17] F. Marsili, V. B. Verma, J. A. Stern, S. Harrington, A. E. Lita, T. Gerrits, I. Vayshenker, B. Baek, M. D. Shaw, R. P. Mirin, and S. W. Nam, *Detecting single infrared photons with 93% system efficiency*, Nat. Photonics **7**, 210 (2013).

[18] R.-M. Ma, and R. F. Oulton, *Applications of nanolasers*, Nat. Nanotechnol. **14**, 12 (2019).

[19] K. Nakayama, K. Tanabe, and H. A. Atwater, *Plasmonic nanoparticle enhanced light absorption in gaas solar cells*, Appl. Phys. Lett **93**, 121904 (2008).

[20] V. C. Nikolis, A. Mischok, B. Siegmund, J. Kublitski, X. Jia, J. Benduhn, U. Hörmann, D. Neher, M. C. Gather, D. Spoltore, and K. Vandewal, *Strong light-matter coupling for reduced photon energy losses in organic photovoltaics*, Nat. Commun. **10**, 1 (2019).

[21] K. D. Heylman, N. Thakkar, E. H. Horak, S. C. Quillin, C. Cherqui, K. A. Knapper, D. J. Masiello, and R. H. Goldsmith, *Optical microresonators as single-particle absorption spectrometers*, Nat. Photonics **10**, 788 (2016).

[22] A. B. Taylor, and P. Zijlstra, *Single-molecule plasmon sensing: Current status and future prospects*, ACS Sens. **2**, 1103 (2017).

[23] P. Zijlstra, P. M. R. Paulo, and M. Orrit, *Optical detection of single non-absorbing molecules using the surface plasmon resonance of a gold nanorod*, Nat. Nanotechnol. **7**, 379 (2012).

[24] M. R. Shcherbakov, P. P. Vabishchevich, A. S. Shorokhov, K. E. Chong, D. Choi, I. Staude, A. E. Miroshnichenko, D. N. Neshev, A. A. Fedyanin, and Y. S. Kivshar, *Ultrafast all-optical switching with magnetic resonances in nonlinear dielectric nanostructures*, Nano Lett. **15**, 6985 (2015).

[25] M. Ono, M. Hata, M. Tsunekawa, K. Nozaki, H. Sumikura, H. Chiba, and M. Notomi, *Ultrafast and energy-efficient all-optical switching with graphene-loaded deep-subwavelength plasmonic waveguides*, Nat. Photonics **14**, 37 (2020).

[26] B. E. A. Saleh, and M. C. Teich, *Fundamentals of Photonics* (John Wiley & Sons, 1991).

[27] N. Ismail, C. C. Kores, D. Geskus, and M. Pollnau, *Fabry-Pérot resonator: spectral line shapes, generic and related airy distributions, linewidths, finesses, and performance at low or frequency dependent reflectivity*, Optics Express **24**, 16366 (2016).

[28] V. P. Debattista, and T. B. Williams, *Fabry-Pérot absorption-line spectroscopy of ngc 7079: Kinematics and bar pattern speed*, Astrophys. J. **605**, 714 (2004).

[29] E. M. Purcell, *Spontaneous emission probabilities at radio frequencies*, Phys. Rev. **69**, 681 (1946).

[30] J. Kimm, H. Oh, B. Kang, J. Hong, J.-J. Rha, and M. Lee, *Broadband visible and near-infrared absorbers implemented with planar nanolayered stacks*, ACS Appl. Nano Mater. **3**, 2978 (2020).

[31] T. Hamaguchia, M. Tanaka, J. Mitomo, H. Nakajima, M. Ito, M. Ohara, N. Kobayashi, K. Fujii, H. Watanabe, S. Satou, R. Koda, and H. Narui, *Lateral optical confinement of GaN-based VCSEL using an atomically smooth monolithic curved mirror*, Sci. Rep. **8**, 1 (2018).

[32] M. H. Bitarafan, and R. G. DeCorby, *On-chip high-finesse Fabry-Pérot microcavities for optical sensing and quantum information*, Sensors **17**, 1748 (2017).

[33] H. Cao, and J. Wiersig, *Dielectric microcavities: Model systems for wave chaos and non-hermitian physics*, Rev. Mod. Phys. **87**, 61 (2015).

[34] M. L. Gorodetsky, and V. S. Ilchenko, *Optical microsphere resonators: optimal coupling to high-Q whispering-gallery modes*, J. Opt. Soc. Am. B: Opt. Phys. **16**, 147 (1999).

[35] D. K. Armani, T. J. Kippenberg, S. M. Spillane, and K. J. Vahala, *Ultra-high-Q toroid microcavity on a chip*, Nature **421**, 925 (2003).

[36] S. Reitzenstein, and A. Forchel, *Quantum dot micropillars*, J. Phys. D: Appl. Phys. **43**, 033001 (2010).

[37] M. Pelton, C. Santori, J. Vučković, B. Y. Zhang, G. Solomon, J. Plant, and Y. Yamamoto, *Efficient source of single photons: A single quantum dot in a micropost microcavity*, Phys. Rev. Lett. **89**, 233602 (2002).

[38] Y. Gong, and J. Vučković, *Photonic crystal cavities in silicon dioxide*, Appl. Phys. Lett. **96**, 031107 (2010).

[39] R. Leijssen, and E. Verhagen, *Strong optomechanical interactions in a sliced photonic crystal nanobeam*, Sci. Rep. **5**, 1 (2015).

[40] Y. Akahane, T. Asano, B. Song, and S. Noda, *High-Q photonic nanocavity in a two-dimensional photonic crystal*, Nature **425**, 944 (2003).

[41] E. Yablonovitch, *Photonic band-gap structures*, J. Opt. Soc. Am. B: Opt. Phys. **10**, 283 (1993).

[42] W. L. Barnes, A. Dereux, and T. W. Ebbesen, *Surface plasmon subwavelength optics*, Nature **424**, 824 (2003).

[43] N. W. Ashcroft, and N. D. Mermin, *Solid State Physics* (Cengage Learning, 1976).

[44] K. L. Kelly, E. Coronado, L. L. Zhao, and G. C. Schatz, *The optical properties of metal nanoparticles: The influence of size, shape, and dielectric environment*, J. Phys. Chem. B **107**, 668 (2003).

[45] K. Lee, and M. A. El-Sayed, *Gold and silver nanoparticles in sensing and imaging: Sensitivity of plasmon response to size, shape, and metal composition*, J. Phys. Chem. B **110**, 19220 (2006).

[46] A. Kinkhabwala, Z. Yu, S. Fan, Y. Avlasevich, K. Müllen, and W. E. Moerner, *Large single-molecule fluorescence enhancements produced by a bowtie nanoantenna*, Nat. Photonics **3**, 654 (2009).

[47] G. M. Akselrod, C. Argyropoulos, T. B. H. C., Ciracì, C. Fang, J. Huang, D. R. Smith, and M. H. Mikkelsen, *Probing the mechanisms of large purcell enhancement in plasmonic nanoantenna*, Nat. Photonics **8**, 835 (2014).

[48] K. J. Russell, K. Y. M. Yeung, and E. Hu, *Measuring the mode volume of plasmonic nanocavities using coupled optical emitters*, Phys. Rev. B **85**, 245445 (2012).

[49] W. Zhu, and K. B. Crozier, *Quantum mechanical limit to plasmonic enhancement as observed by surface-enhanced raman scattering*, Nat. Commun. **5**, 1 (2014).

[50] F. Benz, M. K. Schmidt, A. Dreismann, R. Chikkaraddy, Y. Zhang, A. Demetriadou, C. Carnegie, H. Ohadi, B. de Nijs, R. Esteban, J. Aizpurua, and J. J. Baumberg, *Single-molecule optomechanics in picocavities*, Science **354**, 726 (2016).

[51] J. N. Anker, W. P. Hall, O. Lyandres, N. C. Shah, J. Zhao, and R. P. V. Duyne, *Biosensing with plasmonic nanosensors*, Nat. Mater. **7**, 442 (2008).

[52] B. D. Gates, Q. Xu, M. Stewart, D. Ryan, C. G. Willson, and G. M. Whitesides, *New approaches to nanofabrication: Molding, printing, and other techniques*, Chem. Rev. **105**, 1171 (2005).

[53] L. J. Guo, *Nanoimprint lithography: Methods and material requirements*, Adv. Mater. **19**, 495 (2007).

[54] A. Tao, S. Habas, and P. Yang, *Shape control of colloidal metal nanocrystals*, Small **4**, 310 (2008).

[55] C. Vieu, F. Carcenac, A. Pépin, Y. Chen, M. Mejias, A. Lebib, L. Manin-Ferlazzo, L. Couraud, and H. Launois, *Electron beam lithography: resolution limits and applications*, Appl. Surf. Sci. **164**, 111 (2000).

[56] L. Novotny, and B. Hecht, *Principles of Nano-Optics* (Cambridge University Press, 2006).

[57] C. F. Bohren, and D. R. Huffman, *Absorption and Scattering of Light by Small Particles* (Wiley, 1998).

[58] W. L. Barnes, *Particle plasmons: Why shape matters*, Am. J. Phys. **84**, 593 (2016).

[59] P. de Vries, D. V. van Coevorden, and A. Lagendijk, *Point scatterers for classical waves*, Rev. Mod. Phys. **70**, 447 (1998).

[60] L. Novotny, and N. van Hulst, *Antennas for light*, Nat. Photonics **5**, 83 (2011).

[61] F. J. García de Abajo, *Colloquium: Light scattering by particle and hole arrays*, Rev. Mod. Phys. **79**, 1267 (2007).

[62] P. Lunnemann, I. Sersic, and A. F. Koenderink, *Optical properties of two-dimensional magnetoelectric point scattering lattices*, Phys. Rev. B **88**, 245109 (2013).

[63] Y. Ra'di, C. R. Simovski, and S. A. Tretyakov, *Thin perfect absorbers for electromagnetic waves: Theory, design, and realizations*, Phys. Rev. Applied **3**, 037001 (2015).

[64] A. Kwadrin, C. I. Osorio, and A. F. Koenderink, *Backaction in metasurface etalons*, Phys. Rev. B **93**, 104301 (2016).

[65] I. Sersic, M. Frimmer, E. Verhagen, and A. F. Koenderink, *Electric and magnetic dipole coupling in near-infrared split-ring metamaterial arrays*, Phys. Rev. Lett. **103**, 213902 (2009).

[66] S. Zou, and G. C. Schatz, *Narrow plasmonic/photonic extinction and scattering line shapes for one and two dimensional silver nanoparticle arrays*, J. Chem. Phys. **121**, 12606 (2004).

[67] V. G. Kravets, A. V. Kabashin, W. L. Barnes, and A. N. Grigorenko, *Plasmonic surface lattice resonances: A review of properties and applications*, Chem. Rev. **118**, 5912 (2018).

[68] C. Cherqui, M. R. Bourgeois, D. Wang, and G. C. Schatz, *Plasmonic surface lattice resonances: Theory and computation*, Acc. Chem. Res. **52**, 2548 (2019).

[69] W. Wang, M. Ramezani, A. Väkeväinen, P. Törmä, J. Gómez Rivas, and T. Odom, *The rich photonic world of plasmonic nanoparticle arrays*, Mater. Today **21**, 303 (2017).

[70] A. Kabashin, S. Patskovsky, and A. Grigorenko, *Phase and amplitude sensitivities in surface plasmon resonance bio and chemical sensing*, Opt. Express **17**, 21191 (2009).

[71] W. Zhou, M. Dridi, J. Y. Suh, C. H. Kim, D. T. Co, M. R. Wasielewski, G. C. Schatz, and T. W. Odom, *Lasing action in strongly coupled plasmonic nanocavity arrays*, Nat. Nanotechnol. **8**, 506 (2013).

[72] A. H. Schokker, and A. F. Koenderink, *Lasing at the band edges of plasmonic lattices*, Phys. Rev. B **120**, 155452 (2014).

[73] S. R. K. Rodriguez, and J. Gómez Rivas, *Surface lattice resonances strongly coupled to rhodamine 6g excitons: tuning the plasmon-exciton-polariton mass and composition*, Opt. Express **21**, 27411 (2013).

[74] H. Chen, A. J. Taylor, and N. Yu, *A review of metasurfaces: Physics and applications*, Rep. Prog. Phys. **79**, 076401 (2016).

[75] X. Ni, N. K. Emani, A. V. Kildishev, A. Boltasseva, and V. M. Shalaev, *Broadband light bending with plasmonic nanoantenna*, Science **335**, 427 (2012).

[76] D. Neshev, and I. Aharonovich, *Optical metasurfaces: new generation building blocks for multi-functional optics*, Light Sci. Appl. **7**, 1 (2018).

[77] M. Khorasaninejad, W. T. Chen, R. C. Devlin, J. Oh, A. Y. Zhu, and F. Capasso, *Metalenses at visible wavelengths: Diffraction-limited focusing and subwavelength resolution imaging*, Science **352**, 1190 (2016).

[78] H. M. Doeleman, E. Verhagen, and A. F. Koenderink, *Antenna-cavity hybrids: Matching polar opposites for purcell enhancements at any linewidth*, ACS Photonics **3**, 1943 (2016).

[79] O. Benson, *Assembly of hybrid photonic architectures from nanophotonic constituents*, Nature **480**, 193 (2011).

[80] S. Zou, N. Janel, and G. C. Schatz, *Silver nanoparticle array structures that produce remarkably narrow plasmon lineshapes*, J. Chem. Phys. **120**, 10871 (2004).

[81] Q. Le-Van, E. Zoethout, E. Geluk, M. M. Ramezani, Berghuis, and J. Gómez Rivas, *Enhanced quality factors of surface lattice resonances in plasmonic arrays of nanoparticles*, Adv. Opt. Mater. **7**, 1801451 (2019).

[82] G. Vecchi, V. Giannini, and J. Gómez Rivas, *Shaping the fluorescent emission by lattice resonances in plasmonic crystals of nanoantennas*, Phys. Rev. Lett. **102**, 146807 (2009).

[83] G. Lozano, D. J. Louwers, S. R. K. Rodriguez, S. Murai, O. T. A. Jansen, M. A. Verschuuren, and J. Gómez Rivas, *Plasmonics for solid-state lighting: enhanced excitation and directional emission of highly efficient light sources*, Light Sci. Appl. **2**, e66 (2013).

[84] G. Lozano, S. R. K. Rodriguez, M. A. Verschuuren, and J. Gómez Rivas, *Metallic nanostructures for efficient LED lighting*, Light Sci. Appl. **5**, e16080 (2016).

[85] S. Murai, M. A. Verschuuren, G. Lozano, G. Pirruccio, S. R. K. Rodriguez, and J. Gómez Rivas, *Hybrid plasmonic-photonic modes in diffractive arrays of nanoparticles coupled to light-emitting optical waveguides*, Optics Express **21**, 4250 (2013).

[86] M. Barth, S. Schietinger, S. Fischer, J. Becker, N. Nüsse, T. Aichele, B. Löchel, C. Sönnichsen, and O. Benson, *Nanoassembled plasmonic-photonic hybrid cavity for tailored light-matter coupling*, Nano Lett. **10**, 891 (2010).

[87] K. G. Cognée, H. M. Doeleman, P. Lalanne, and A. F. Koenderink, *Cooperative interactions between nanoantennas in a high Q cavity for unidirectional light sources*, Light Sci. Appl. **8**, 115 (2019).

[88] F. Ruesink, H. M. Doeleman, E. Verhagen, and A. F. Koenderink, *Controlling Nanoantenna Polarizability through Backaction via a Single Cavity Mode*, Phys. Rev. Lett. **120**, 206101 (2018).

[89] M. D. Baaske, and F. Vollmer, *Optical observation of single atomic ions interacting with plasmonic nanorods in aqueous solution*, Nat. Photonics **10**, 733 (2016).

[90] N. Thakkar, M. T. Rea, K. C. Smith, K. D. Heylman, S. C. Quillin, K. A. Knapper, E. H. Horak, D. J. Masiello, and R. H. Goldsmith, *Sculpting Fano resonances to control photonic–plasmonic hybridization*, Nano Lett. **17**, 6927 (2017).

[91] F. Pan, K. C. Smith, H. L. Nguyen, K. A. Knapper, D. J. Masiello, and R. H. Goldsmith, *Elucidating energy pathways through simultaneous measurement of absorption and transmission in a coupled plasmonic–photonic cavity*, Nano Lett. **20**, 50 (2020).

[92] K. D. Heylman, N. Thakkar, E. H. Horak, S. C. Quillin, C. Cherqui, K. A. Knapper, D. J. Masiello, and R. H. Goldsmith, *Optical microresonators as single-particle absorption spectrometers*, Nat. Photonics **10**, 788 (2016).

[93] B. Gurlek, V. Sandoghdar, and D. Martín-Cano, *Manipulation of quenching in nanoantenna–emitter systems enabled by external detuned cavities: A path to enhance strong-coupling*, ACS Photonics **5**, 456 (2018).

[94] R. Ameling, L. Langguth, M. Hentschel, M. Mesch, P. Braun, and H. Giessen, *Cavity-enhanced localized plasmon resonance sensing*, Appl. Phys. Lett. **97**, 253116 (2010).

[95] R. Ameling, D. Dregely, and H. Giessen, *Strong coupling of localized and surface plasmons to microcavity modes*, Opt. Lett. **36**, 2218 (2011).

[96] R. Ameling, and H. Giessen, *Microcavity plasmonics: strong coupling of photonic cavities and plasmons*, Laser Photonics Rev. **7**, 141 (2013).

[97] R. Ameling, and H. Giessen, *Cavity plasmonics: Large normal mode splitting of electric and magnetic particle plasmons induced by a photonic microcavity*, Nano Lett. **10**, 4394 (2010).

[98] A. Bisht, J. Cuadra, M. Wersäll, A. Canales, T. J. Antosiewicz, and T. Shegai, *Collective strong light-matter coupling in hierarchical microcavity-plasmon-exciton systems*, Nano Lett. **19**, 189 (2019).

[99] D. G. Baranov, M. Wersall, J. Cuadra, T. J. Antosiewicz, and T. Shegai, *Novel nanostructures and materials for strong light-matter interactions*, ACS Photonics **5**, 24 (2018).

[100] M. Geisler, X. Cui, J. Wang, T. Rindzevicius, L. Gammelgaard, B. S. Jessen, P. A. D. Gonçalves, F. Todisco, A. B. P. Bøoggild, M. Wubs, N. A. Mortensen, S. Xiaon, , and N. Stenger, *Single-crystalline gold nanodisks on WS_2 mono- and multilayers for strong coupling at room temperature*, ACS Photonics **6**, 994 (2019).

[101] G. S. Agarwal, and S. S. Jha, *Theory of second harmonic generation at a metal surface with surface plasmon excitation*, Solid State Commun. **41**, 499 (1982).

[102] B. Lamprecht, A. Leitner, and F. R. Aussenegg, *SHG studies of plasmon dephasing in nanoparticles*, Applied Physics B **68**, 419 (1999).

[103] T. Zhao, J. Jarrett, J. Johnson, K. Park, R. Vaia, and J. J.L. Knappenberger, *Plasmon dephasing in gold nanorods studied using single- nanoparticle interferometric nonlinear optical microscopy*, J. Phys. Chem. C **120**, 4071 (2016).

[104] N. Accanto, J. B. Nieder, L. Piatkowski, M. Castro-Lopez, F. Pastorelli, D. Brinks, and N. F. van Hulst, *Phase control of femtosecond pulses on the nanoscale using second harmonic nanoparticles*, Light Sci. Appl. **3**, e143 (2014).

[105] M. Lippitz, M. van Dijk, and M. Orrit, *Third-harmonic generation from single gold nanoparticles*, Nano Lett. **5**, 799 (2005).

[106] J. Butet, J. Duboisset, G. Bachelier, I. Russier-Antoine, E. Benichou, C. Jonin, and P.-F. Brevet, *Optical second harmonic generation of single metallic nanoparticles embedded in a homogeneous medium*, Nano Lett. **10**, 1717 (2010).

[107] H. Wang, T. B. Huff, D. A. Zweifel, W. He, P. S. Low, A. Wei, and J.-X. Cheng, *In vitro and in vivo two-photon luminescence imaging of single gold nanorods*, PNAS **102**, 15752 (2005).

[108] P. Wnuk, L. L. Xuan, A. Slablab, C. Tard, S. Perruchas, T. Gacoin, J.-F. Roch, D. Chauvat, and C. Radzewicz, *Coherent nonlinear emission from a single KTP nanoparticle with broadband femtosecond pulses*, Opt. Express **17**, 4652 (2009).

[109] T. Hanke, G. Krauss, D. Traütlein, B. Wild, R. Bratschitsch, and A. Leitenstorfer, *Efficient nonlinear light emission of single gold optical antennas driven by few-cycle near-infrared pulses*, Phys. Rev. Lett. **103**, 257404 (2009).

[110] F. B. P. Niesler, N. Feth, S. Linden, and M. Wegener, *Second-harmonic optical spectroscopy on split-ring-resonator arrays*, Opt. Lett. **36**, 1533 (2011).

[111] D. C. Hooper, C. Kuppe, D. Wang, W. Wang, J. Guan, T. W. Odom, and V. K. Valev, *Second harmonic spectroscopy of surface lattice resonances*, Nano Lett. **19**, 165 (2019).

[112] N. Yu, and F. Capasso, *Flat optics with designer metasurfaces*, Nat. Mater. **13**, 139 (2014).

[113] P. Genevet, F. Capasso, F. Aieta, M. Khorasaninejad, and R. Devlin, *Recent advances in planar optics: from plasmonic to dielectric metasurfaces*, Optica **4**, 139 (2017).

[114] F. Ding, Y. Yang, R. A. Deshpande, and S. I. Bozhevolnyi, *A review of gap-surface plasmon metasurfaces: fundamentals and applications*, Nanophotonics **7**, 1129 (2018).

[115] P. Lalanne, S. Astilean, P. Chavel, E. Cambril, and H. Launois, *Blazed binary subwavelength gratings with efficiencies larger than those of conventional échelette gratings*, Opt. Lett. **23**, 1081 (1998).

[116] F. Aieta, P. Genevet, M. A. Kats, N. Yu, R. Blanchard, Z. Gaburro, and F. Capasso, *Aberration-free ultrathin flat lenses and axicons at telecom wavelengths based on plasmonic metasurfaces*, Nano Lett. **12**, 4932 (2012).

[117] A. Arbabi, Y. Horie, A. J. Ball, M. Bagheri, and A. Faraon, *Subwavelength-thick lenses with high numerical apertures and large efficiency based on high-contrast transmitarrays*, Nat. Commun. **6**, 7069 (2015).

[118] T.-Y. Huang, R. R. Grote, S. A. Mann, D. A. Hopper, A. L. Exarhos, G. G. Lopez, G. R. Kaighn, E. C. Garnett, and L. C. Bassett, *A monolithic immersion metalens for imaging solid-state quantum emitters*, Nat. Commun. **10**, 2392 (2019).

[119] N. Yu, F. Aieta, P. Genevet, M. A. Kats, Z. Gaburro, and F. Capasso, *A broadband, background-free quarter-wave plate based on plasmonic metasurfaces*, Nano Lett. **12**, 6328 (2012).

[120] A. Arbabi, Y. Horie, M. Bagheri, and A. Faraon, *Dielectric metasurfaces for complete control of phase and polarization with subwavelength spatial resolution and high transmission*, Nat. Nanotechnol. **10**, 937 (2015).

[121] M. Khorasaninejad, W. Zhu, and K. B. Crozier, *Efficient polarization beam splitter pixels based on a dielectric metasurface*, Optica **2**, 376 (2015).

[122] H. Kwon, E. Arbabi, S. M. Kamali, M. Faraji-Dana, and A. Faraon, *Computational complex optical field imaging using a designed metasurface diffuser*, Optica **5**, 924 (2018).

[123] A. Silva, F. Monticone, G. Castaldi, V. Galdi, A. Alù, and N. Engheta, *Performing mathematical operations with metamaterials*, Science **343**, 160 (2014).

[124] H. Kwon, D. Sounas, A. Cordaro, A. Polman, and A. Alù, *Nonlocal metasurfaces for optical signal processing*, Phys. Rev. Lett. **121**, 173004 (2018).

[125] A. Cordaro, H. Kwong, D. Sounas, A. F. Koenderink, A. Alù, and A. Polman, *High-index dielectric metasurfaces performing mathematical operations*, Nano Lett. **19**, 8418 (2019).

[126] B. Sima, K. Chen, X. Luo, J. Zhao, and Y. Feng, *Combining frequency-selective scattering and specular reflection through phase-dispersion tailoring of a metasurface*, Phys. Rev. Applied **10**, 064043 (2018).

[127] W. W. Salisbury, *Absorbent body for electromagnetic waves* (1952).

[128] R. L. Fante, and M. T. McCormack, *Reflection properties of the salisbury screen*, IEEE Trans. Antenn. Prop. **36**, 1443 (1988).

[129] A. Pors, and S. I. Bozhevolnyi, *Plasmonic metasurfaces for efficient phase control in reflection*, Opt. Express **21**, 27438 (2013).

[130] H.-T. Chen, *Interference theory of metamaterial perfect absorbers*, Optics Express **20**, 7165 (2012).

[131] R. Alaee, M. Farhat, C. Rockstuhl, and F. Lederer, *A perfect absorber made of a graphene micro-ribbon metamaterial*, Optics Express **20**, 28017 (2012).

[132] F. Huang, S. Drakeley, M. G. Millyard, A. Murphy, R. White, E. Spigone, J. Kivioja, and J. J. Baumberg, *Zero-reflectance metafilms for optimal plasmonic sensing*, Adv. Opt. Mater. **4**, 328 (2016).

[133] R. Alaee, M. Albooyeh, and C. Rockstuhl, *Theory of metasurface based perfect absorbers*, J. Phys. D: Appl. Phys. **50**, 503002 (2017).

[134] P. T. Bowen, A. Baron, and D. R. Smith, *Theory of patch-antenna metamaterial perfect absorbers*, Phys. Rev. A **93**, 063849 (2016).

[135] K. Aydin, V. E. Ferry, R. M. Briggs, and H. A. Atwater, *Broadband polarization-independent resonant light absorption using ultrathin plasmonic super absorbers*, Nat. Commun. **2**, 517 (2011).

[136] A. Berkhout, and A. F. Koenderink, *Perfect absorption and phase singularities in plasmon antenna array etalons*, ACS Photonics **6**, 2917 (2019).

[137] K. Kumar, H. Duan, R. S. Hegde, S. C. W. Koh, J. N. Wei, and J. K. W. Yang, *Printing colour at the optical diffraction limit*, Nat. Nanotechnol. **7**, 557 (2012).

[138] S. J. Tan, L. Zhang, D. Zhu, X. M. Goh, Y. M. Wang, K. Kumar, C.-W. Qiu, and J. K. W. Yang, *Plasmonic color palettes for photorealistic printing with aluminum nanostructures*, Nano Lett. **14**, 4023 (2014).

[139] Y. Gu, L. Zhang, J. K. W. Yang, S. P. Yeo, and C.-W. Qiu, *Color generation via subwavelength plasmonic nanostructures*, Nanoscale **7**, 6409 (2015).

[140] A. Kristensen, J. Yang, S. Bozhevolnyi, S. Link, P. Nordlander, N. Halas, and N. Mortensen, *Plasmonic colour generation*, Nat. Rev. Mater. **2**, 16088 (2016).

[141] M. Song, X. Li, M. Pu, Y. Guo, K. Liu, H. yu, X. Ma, and X. Luo, *Color display and encryption with a plasmonic polarizing metamirror*, Nanophotonics **7**, 323 (2017).

[142] M. Song, Z. A. Kudyshev, H. Yu, A. Boltasseva, V. M. Shalaev, and A. V. Kildishev, *Achieving full-color generation with polarization-tunable perfect light absorption*, Opt. Mater. Express **9**, 779 (2019).

[143] S. Alrasheed, and E. Di Fabrizio, *Effect of surface plasmon coupling to optical cavity modes on the field enhancement and spectral response of dimer-based sensors*, Sci. Rep. **7**, 10524 (2017).

[144] Y. Zhu, D. J. Gauthier, S. E. Morin, Q. Wu, H. J. Carmichael, and T. W. Mossberg, *Vacuum rabi splitting as a feature of linear-dispersion theory: Analysis and experimental observations*, Phys. Rev. Lett. **64**, 2499 (1990).

[145] D. G. Baranov, M. Wersäll, J. Cuadra, T. J. Antosiewicz, and T. Shegai, *Novel nanostructures and materials for strong light–matter interactions*, ACS Photonics **5**, 24 (2018).

[146] P. Törmä, and W. L. Barnes, *Strong coupling between surface plasmon polaritons and emitters: a review*, Rep. Prog. Phys. **78**, 013901 (2014).

[147] B. Munkhbat, D. G. Baranov, M. Stührenberg, M. Wersäll, A. Bisht, and T. Shegai, *Self-hybridized exciton-polaritons in multilayers of transition metal dichalcogenides for efficient light absorption*, ACS Photonics **6**, 139 (2019).

[148] S. R. K. Rodriguez, Y. T. Chen, T. P. Steinbusch, M. A. Verschuuren, A. F. Koenderink, and J. Gómez Rivas, *From weak to strong coupling of localized surface plasmons to guided modes in a luminescent slab*, Phys. Rev. B **90**, 235406 (2014).

[149] S. Wang, *Strong light-molecule coupling: routes to new hybrid materials*, Ph.D. thesis (2015).

[150] S. Wang, S. Li, T. Chervy, A. Shalabney, S. Azzini, E. Orgiu, J. A. Hutchison, C. Genet, P. Samorì, and T. W. Ebbesen, *Coherent coupling of WS_2 monolayers with metallic photonic nanostructures at room temperature*, Nano Lett. **16**, 4368 (2016).

[151] M. Ramezani, A. Halpin, A. I. Fernández-Domínguez, J. Feist, S. R. K. Rodriguez, F. J. Garcia-Vidal, and J. Gómez Rivas, *Plasmon-exciton-polariton lasing*, Optica **4**, 31 (2017).

[152] P. Yeh, A. Yariv, and C.-S. Hong, *Electromagnetic propagation in periodic stratified media. I. General theory*, J. Opt. Soc. Am. **67**, 423 (1977).

[153] A. Yariv, and P. Yeh, *Electromagnetic propagation in periodic stratified media. ii. birefringence, phase matching, and x-ray lasers*, J. Opt. Soc. Am. **67**, 438 (1977).

[154] C. Menzel, J. Sperrhake, and T. Pertsch, *Efficient treatment of stacked metasurfaces for optimizing and enhancing the range of accessible optical functionalities*, Phys. Rev. A **93**, 063832 (2016).

[155] J. Sperrhake, M. Decker, S. Falkner, M. Fasold, T. Kaiser, I. Staude, and T. Pertsch, *Analyzing the polarization response of a chiral metasurface stack by semi-analytic modeling*, Opt. Express **27**, 1236 (2019).

[156] D. Baranov, B. Munkhbat, N. Länk, R. Verre, M. Käll, and T. Shegai, *Circular dichroism mode splitting and bounds to its enhancement with cavity-plasmon-polaritons*, Nanophotonics **9**, 283 (2019).

[157] S. Thongrattanasiri, F. H. L. Koppens, and F. J. García de Abajo, *Complete optical absorption in periodically patterned graphene*, Phys. Rev. Lett. **108**, 047401 (2012).

[158] A. Krasnok, D. Baranov, H. Li, M.-A. Miri, F. Monticone, and A. Alù, *Anomalies in light scattering*, Adv. Opt. Photon. **11**, 892 (2019).

[159] H. J. Carmichael, R. J. Brecha, M. G. Raizen, H. J. Kimble, and P. R. Rice, *Subnatural linewidth averaging for coupled atomic and cavity-mode oscillators*, Phys. Rev. A **40**, 5516 (1989).

[160] J. M. Raimond, and S. Haroche, *Confined Electrons and Photons: New Physics and Applications* (NATO Science Series B, Springer, 1995), chap. Atoms in Cavities, pp. 383–426.

[161] C. Weisbuch, M. Nishioka, A. Ishikawa, and Y. Arakawa, *Observation of the coupled exciton-photon mode splitting in a semiconductor quantum microcavity*, Phys. Rev. Lett. **69**, 3314 (1992).

[162] D. G. Lidzey, D. C. Bradley, M. S. Skolnick, T. Virgili, S. Walker, and D. M. Whittaker, *Strong exciton–photon coupling in an organic semiconductor microcavity*, Nature **395**, 53 (1998).

[163] H.-S. Wei, C.-C. Jaing, Y.-T. Chen, C.-C. Lin, C.-W. Cheng, C.-H. Chan, C.-C. Lee, and J.-F. Chang, *Adjustable exciton-photon coupling with giant rabi-splitting using layer-by-layer j-aggregate thin films in all-metal mirror microcavities*, Optics Express **21**, 21365 (2013).

[164] M. R. Foreman, and F. Vollmer, *Theory of resonance shifts of whispering gallery modes by arbitrary plasmonic nanoparticles*, New J. Phys. **15**, 083006 (2013).

[165] J. Xavier, S. Vincent, F. Meder, and F. Vollmer, *Advances in optoplasmonic sensors – combining optical nano/microcavities and photonic crystals with plasmonic nanostructures and nanoparticles*, Nanophotonics **7**, 1 (2017).

[166] S. Rodriguez, *Classical and quantum distinctions between weak and strong coupling*, Eur. J. Phys. **37**, 025802 (2016).

[167] A. M. Jayich, B. M. Sankey, J.C.and Zwickl, C. Yang, J. D. Thompson, S. Girvin, A. A. Clerk, F. Marquardt, and J. G. E. Harris, *Dispersive optomechanics: a membrane inside a cavity*, New J. Phys. **10**, 095008 (2008).

[168] F. Bernal Arango, T. Coenen, and A. F. Koenderink, *Underpinning hybridization intuition for complex antennas by magnetoelectric quadrupolar polarizability retrieval*, ACS Photonics **1**, 444 (2014).

[169] S. Rodriguez, *Enhancing the speed and sensitivity of a nonlinear optical sensor with noise*, Phys. Rev. Appl. **13**, 024032 (2020).

[170] D. Ballarini, and S. D. Liberato, *Polaritonics: from microcavities to sub-wavelength confinement*, Nanophotonics **8**, 641 (2019).

[171] I. Sersic, C. Tuambilangana, T. Kampfrath, and A. F. Koenderink, *Magnetoelectric point scattering theory for metamaterial scatterers*, Phys. Rev. B **83**, 245102 (2011).

[172] Y. T. Chen, Y. Zhang, and A. F. Koenderink, *General point dipole theory for periodic metasurfaces: magnetoelectric scattering lattices coupled to planar photonic structures*, Optics Express **25**, 21358 (2017).

[173] C. M. Watts, X. Liu, and W. J. Padilla, *Metamaterial electromagnetic wave absorbers*, Adv. Mater. **24**, OP98 (2012).

[174] N. Liu, M. Mesch, T. Weiss, M. Hentschel, and H. Giessen, *Infrared perfect absorber and its application as plasmonic sensor*, Nano Lett. **10**, 2342 (2010).

[175] M. S. Jang, V. W. Brar, M. C. Sherrott, J. J. Lopez, L. Kim, S. Kim, M. Choi, and H. A. Atwater, *Tunable large resonant absorption in a midinfrared graphene salisbury screen*, Phys. Rev. B **90**, 165409 (2014).

[176] G. Pirruccio, L. Martín Moreno, G. Lozano, and J. J. Gómez Rivas, *Coherent and broadband enhanced optical absorption in graphene*, ACS Nano **7**, 4810 (2013).

[177] N. Kakenov, O. Balci, T. Takan, V. A. Ozkan, H. Altan, and C. Kocabas, *Observation of gate-tunable coherent perfect absorption of terahertz radiation in graphene*, ACS Photonics **3**, 1531 (2016).

[178] T. Henseleit, M. Sudzius, H. Fröb, and K. Leo, *Coherent perfect absorption in wedged organic thin films: a method to determine optical properties*, Opt. Lett. **43**, 4013 (2018).

[179] B. A. Munk, *Frequency Selective Surfaces: Theory and Design* (J. Wiley & Sons, New York, 2005).

[180] Y. D. Chong, L. Ge, H. Cao, and A. D. Stone, *Coherent perfect absorbers: Time-reversed lasers*, Phys. Rev. Lett. **105**, 053901 (2010).

[181] W. Wan, Y. Chong, L. Ge, H. Noh, A. D. Stone, and H. Cao, *Time-reversed lasing and interferometric control of absorption*, Science **331**, 889 (2011).

[182] M. G. Nielsen, A. Pors, O. Albrektsen, and S. I. Bozhevolnyi, *Efficient absorption of visible radiation by gap plasmon resonators*, Opt. Express **20**, 13311 (2012).

[183] A. Christ, T. Zentgraf, S. G. Tikhodeev, N. A. Gippius, J. Kuhl, and H. Giessen, *Controlling the interaction between localized and delocalized surface plasmon modes: Experiment and numerical calculations*, Phys. Rev. B **74**, 155435 (2006).

[184] Q. Wang, E. Plum, Q. Yang, X. Zhang, Q. Xu, Y. Xu, J. Han, and W. Zhang, *Reflective chiral meta-holography: multiplexing holograms for circularly polarized waves*, Light Sci. Appl. **7**, 25 (2018).

[185] M. Miyata, H. Hatada, and J. Takahara, *Full-color subwavelength printing with gap-plasmonic optical antennas*, Nano Lett. **16**, 3166 (2016).

[186] C. Qu, S. Ma, J. Hao, M. Qiu, X. Li, S. Xiao, Z. Miao, N. Dai, Q. He, S. Sun, and L. Zhou, *Tailor the functionalities of metasurfaces based on a complete phase diagram*, Phys. Rev. Lett. **115**, 235503 (2015).

[187] R. H. J. Kop, and R. Sprik, *Phase-sensitive interferometry with ultrashort optical pulses*, Rev. Sci. Instr. **66**, 5459 (1995).

[188] D. R. Solli, C. F. McCormick, R. Y. Chiao, S. Popescum, and J. M. Hickmann, *Fast light, slow light, and phase singularities: A connection to generalized weak values*, Phys. Rev. Lett. **92**, 043601 (2004).

[189] M. Asano, K. Y. Bliokh, Y. P. Bliokh, A. G. Kofman, R. Ikuta, T. Yamamoto, Y. S. Kivshar, L. Yang, N. Imoto, Ş. K. Özdemir, and F. Nori, *Anomalous time delays and quantum weak measurements in optical micro-resonators*, Nat. Commun. **7**, 13488 (2016).

[190] W. Wang, M. Ramezani, A. I. Vakevainen, P. Torma, J. Gómez Rivas, and T. W. Odom, *The rich photonic world of plasmonic nanoparticle arrays*, Mater. Today **21**, 303 (2018).

[191] M. Svedendahl, R. Verre, and M. Kall, *Refractometric biosensing based on optical phase flips in sparse and short-range-ordered nanoplasmonic layers*, Light Sci. Appl. **3**, e220 (2014).

[192] V. G. Kravets, F. Schedin, R. Jalil, L. Britnell, R. V. Gorbachev, D. Ansell, B. Thackray, K. S. Novoselov, A. K. Geim, A. V. Kabashin, and A. N. Grigorenko, *Singular phase nano-optics in plasmonic metamaterials for label-free single-molecule detection*, Nat. Mater **12**, 304 (2013).

[193] C. Yan, T. V. Raziman, and O. J. F. Martin, *Phase bifurcation and zero reflection in planar plasmonic metasurfaces*, ACS Photonics **4**, 852 (2017).

[194] K. V. Sreekanth, S. Sreejith, S. Han, A. Mishra, X. Chen, H. Sun, C. T. Lim, and R. Singh, *Biosensing with the singular phase of an ultrathin metal-dielectric nanophotonic cavity*, Nat. Commun. **9**, 369 (2018).

[195] M. A. van Dijk, M. Lippitz, D. Stolwijk, and M. Orrit, *A common-path interferometer for time-resolved and shot-noise-limited detection of single nanoparticles*, Opt. Express **15**, 2273 (2007).

[196] A. J. Leggett, S. Chakravarty, A. T. Dorsey, M. P. A. Fisher, A. Garg, and W. Zwerger, *Dynamics of the dissipative two-state system*, Rev. Mod. Phys. **59**, 1 (1987).

[197] L. Novotny, *Strong coupling, energy splitting, and level crossings: A classical perspective*, Am. J. Phys. **78**, 1199 (2010).

[198] M. F. Limonov, M. V. Rybin, A. N. Poddubny, and Y. S. Kivshar, *Fano resonances in photonics*, Nat. Photonics **11**, 543 (2017).

[199] M. Miri, and A. Alù, *Exceptional points in optics and photonics*, Science **363**, 6422 (2019).

[200] C. Wu, A. Khanikaev, R. Adato, N. Arju, A. Yanik, H. Altug, and G. Shvets, *Fano-resonant asymmetric metamaterials for ultrasensitive spectroscopy and identification of molecular monolayers*, Nat. Mater. **11**, 69 (2011).

[201] I. M. Palstra, H. M. Doeleman, and A. F. Koenderink, *Hybrid cavity-antenna systems for quantum optics outside the cryostat?*, Nanophotonics **8**, 1513 (2019).

[202] S. Wang, T. Chervy, J. George, J. A. Hutchison, C. Genet, and T. W. Ebbesen, *Quantum yield of polariton emission from hybrid light-matter states*, J. Phys. Chem. Lett **5**, 1433 (2014).

[203] K. S. Menghrajani, H. A. Fernandez, G. R. Nash, and W. L. Barnes, *Hybridization of multiple vibrational modes via strong coupling using confined light fields*, Adv. Opt. Mater. **7**, 1900403 (2019).

[204] K. Guo, A. Antoncecchi, X. Zheng, M. Sallam, E. A. Soliman, G. A. E. Vandenbosch, V. V. Moshchalkov, and A. F. Koenderink, *Dendritic optical antennas: scattering properties and fluorescence enhancement*, Sci. Rep. **7**, 1 (2017).

[205] A. Berkhout, and A. F. Koenderink, *A simple transfer-matrix model for metasurface multilayer systems*, Nanophotonics **9**, 3985 (2020).

[206] C. I. Osorio, A. Mohtashami, and A. F. Koenderink, *K-space polarimetry of bullseye plasmon antennas*, Sci. Rep. **5**, 9966 (2015).

[207] S. Richter, H.-G. Zirnstein, J. Zúñiga-Pérez, E. Krüger, C. Deparis, L. Trefflich, C. Sturm, B. Rosenow, M. Grundmann, and R. Schmidt-Grund, *Voigt exceptional points in an anisotropic ZnO-based planar microcavity: Square-root topology, polarization vortices, and circularity*, Phys. Rev. Lett. **123**, 227401 (2019).

[208] H. Yu, Y. Peng, Y. Yang, and Z. Li, *Plasmon-enhanced light–matter interactions and applications*, npj Comput. Mater. **5** (2019).

[209] Z. Tian, B. Ren, and D. Wu, *Surface-enhanced raman scattering: From noble to transition metals and from rough surfaces to ordered nanostructures*, J. Phys. Chem. B **106**, 9463 (2002).

[210] S. Gwo, C. Wang, H. Chen, M. Lin, L. Sun, X. Li, W. Chen, Y. Chang, and H. Ahn, *Plasmonic metasurfaces for nonlinear optics and quantitative SERS*, ACS Photonics **3**, 1371 (2016).

[211] T. Vo-Dinh, H. Wang, and J. P. Scaffidi, *Plasmonic nanoprobes for SERS biosensing and bioimaging*, J. Biophotonics **3**, 89 (2009).

[212] P. Alivisatos, *The use of nanocrystals in biological detection*, Nature Biotechnology **22**, 47 (2004).

[213] J. Schuller, E. S. Barnard, W. Cai, Y. Jun, J. White, and M. Brongersma, *Plasmonics for extreme light concentration and manipulation*, Nat. Mater. **9**, 193 (2010).

[214] J. Butet, P. Brevet, and O. Martin, *Optical second harmonic generation in plasmonic nanostructures: From fundamental principles to advanced application*, ACS Nano **9**, 10545 (2015).

[215] M. Kauranen, and A. Zayats, *Nonlinear plasmonics*, Nat. Photonics **6**, 737 (2012).

[216] J. M. Dalmau, C. Vilches, V. Sanz, I. de Miguel, V. Rodríguez-Fajardo, P. Berto, M. M. inez Lozano, O. Casanovas, T. Durduran, and R. Quidant, *Quantification of gold nanoparticle accumulation in tissue by two-photon luminescence microscopy*, Nanoscale **13**, 11331 (2019).

[217] H. Linnenbank, Y. Grynko, J. Förstner, and S. Linden, *Second harmonic generation spectroscopy on hybrid plasmonic/dielectric nanoantennas*, Light Sci. Appl. **5**, e16013 (2016).

[218] H. Aouani, M. Navarro-Cia, M. Rahmani, T. P. H. Sidiropoulos, M. Hong, R. F. Oulton, and S. A. Maier, *Multiresonant broadband optical antennas as efficient tunable nanosources of second harmonic light*, Nano Lett. **12**, 4997 (2012).

[219] G. F. Walsh, and L. D. Negro, *Enhanced second harmonic generation by photonic–plasmonic fano-type coupling in nanoplasmonic arrays*, Nano Lett. **13**, 3111 (2013).

[220] B. Lamprecht, J. R. Krenn, A. Leitner, and F. R. Aussenegg, *Resonant and off-resonant light-driven plasmons in metal nanoparticles studied by femtosecond-resolution third-harmonic generation*, Phys. Rev. Lett. **83**, 4421 (1999).

[221] T. Wang, D. Halaney, D. Ho, M. D. Feldman, and T. E. Milner, *Two-photon luminescence properties of gold nanorods*, Biomed. Opt. Express **4**, 584 (2013).

[222] P. J. Bennett, A. R. Bungay, A. Malinowski, S. V. Popov, I. R. Shatwell, and N. I. Zheludev, *Application of nonlinearities of metals in ultrashort pulse measurements*, in *Summaries of papers presented at the Conference on Lasers and Electro-Optics* (IEEE, 1996), p. 224.

[223] P. J. Bennett, A. Malinowski, B. D. Rainford, I. R. Shatwell, Y. P. Svirko, and N. I. Zheludev, *Femtosecond pulse duration measurements utilizing an ultrafast nonlinearity of nickel*, Opt. Commun. **147**, 148 (1998).

[224] B. Lamprecht, A. Leitner, and F. R. Aussenegg, *Femtosecond decay-time measurement of electron-plasma oscillation in nanolithographically designed silver particles*, Applied Physics B **64**, 269 (1997).

[225] J. Trull, S. Saltiel, V. Roppo, C. Cojocaru, D. Dumay, W. Krolikowski, D. Neshev, R. Vilaseca, K. Staliunas, and Y. Kivshar, *Characterization of femtosecond pulses via transverse second-harmonic generation in random nonlinear media*, Appl. Phys. B **95**, 609 (2009).

[226] F. B. Niesler, N. Feth, S. Linden, J. Niegemann, J. Gieseler, K. Busch, and M. Wegener, *Second-harmonic generation from split-ring resonators on a GaAs substrate*, Opt. Lett. **34**, 1997 (2009).

[227] M. J. Huttunen, P. Rasekh, R. W. Boyd, and K. Dolgaleva, *Using surface lattice resonances to engineer nonlinear optical processes in metal nanoparticle arrays*, Phys. Rev. A **97**, 053817 (2018).

[228] L. Michaeli, S. Keren-Zur, O. Avayu, H. Suchowski, and T. Ellenbogen, *Nonlinear surface lattice resonance in plasmonic nanoparticle arrays*, Phys. Rev. Lett. **118**, 243904 (2017).

[229] T. Nagy, M. Kretschmar, M. Vrakking, and A. Rouzée, *Generation of above-terawatt 1.5-cycle visible pulses at 1 kHz by post-compression in a hollow fiber*, Opt. Lett. **45**, 3313 (2020).

[230] M. Wollenhaupt, A. Assion, and T.Baumert, *Femtosecond Laser Pulses: Linear Properties, Manipulation, Generation and Measurement in Handbook of Lasers and Optics* (Springer-Verlag, New York, 2007).

[231] I. Walmsley, and C. Dorrer, *Characterization of ultrashort electromagnetic pulses*, Adv. Opt. Photonics **1**, 308 (2009).

[232] A. Monmayrant, S. Weber, and B. Chatel, *A newcomer's guide to ultrashort pulse shaping and characterization*, J. Phys. B: At. Mol. Opt. Phys. **43**, 103001 (2010).

[233] M. Göppert-Mayer, *Über Elementarakte mit zwei Quantensprüngen*, Ann. Phys. **401**, 273 (1931).

[234] P. Franken, A. Hill, C. Peters, and G. Weinreich, *Generation of optical harmonics*, Phys. Rev. Lett. **7**, 118 (1961).

[235] W. Kaiser, and C. G. B. Garrett, *Two-photon excitation in CaF_2: Eu^{2+}*, Phys. Rev. Lett. **7**, 229 (1961).

[236] E. Garmire, *Nonlinear optics in daily life*, Optics Express **21**, 30532 (2013).

[237] R. Klein, G. Kugel, A. Maillard, A. Sifi, and K. Polgár, *Absolute non-linear optical coefficients measurements of BBO single crystal and determination of angular acceptance by second harmonic generation*, Optical Materials **22**, 163 (2003).

[238] A. Salomon, M. Zielinski, R. Kolkowski, J. Zyss, and Y. Prior, *Size and shape resonances in second harmonic generation from silver nanocavities*, J. Phys. Chem. C **117**, 22377 (2013).

[239] R. Kolkowski, L. Petti, M. Rippa, C. Lafargue, and J. Zyss, *Size and shape resonances in second harmonic generation from silver nanocavities*, ACS Photonics **2**, 899 (2015).

[240] G. Steinmeyer, *A review of ultrafast optics and optoelectronics*, J. Opt. A: Pure Appl. Opt. **5**, R1 (2002).

[241] R. Trebino, *Frequency-Resolved Optical Gating: The Measurement of Ultrashort Laser Pulses* (Springer Science+Business Media, New York, 2000).

[242] C. Xu, and W. W. Webb, *Measurement of two-photon excitation cross sections of molecular fluorophores with data from 690 to 1050 nm*, J. Opt. Soc. Am. B **13**, 481 (1996).

[243] D. Brida, C. Manzoni, and G. Cerullo, *Phase-locked pulses for two-dimensional spectroscopy by a birefringent delay line*, Opt. Lett. **37**, 3027 (2012).

[244] M. van Dijk, M. Lippitz, D. Stolwijk, and M. Orrit, *A common-path interferometer for time-resolved and shot-noise-limited detection of single nanoparticles*, Optics Express **15**, 2273 (2007).

[245] J. Chandezon, J.-M. Rampnoux, S. Dilhaire, B. Audoin, and Y. Guillet, *In-line femtosecond common-path interferometer in reflection mode*, Optics Express **23**, 27011 (2015).

[246] O. A. Aktsipetrov, I. M. Baranova, E. D. Mishina, and A. V. Petukhov, *Lightning rod effect in surface-enhanced second-harmonic generation*, JETP Lett. **40**, 1012 (1984).

[247] M. Kaempfe, T. Rainer, K.-J. Berg, G. Seifert, and H. Graener, *Ultrashort laser pulse induced deformation of silver nanoparticles in glass*, Appl. Phys. Lett. **74**, 1200 (1999).

List of publications

Related to this thesis

1. A. Berkhout and A. F. Koenderink, *Perfect Absorption and Phase Singularities in Plasmon Antenna Array Etalons*, ACS Photonics **6**, 2917 (2019) (**Chapter 3**).

2. A. Berkhout and A. F. Koenderink, *A simple transfer-matrix model for metasurface multilayer systems*, Nanophotonics **9**, 3985 (2020) (**Chapter 2**).

3. A. Berkhout, T. A. W. Wolterink and A. F. Koenderink, *Strong coupling to generate complex birefringence - metasurface in the middle etalons*, ACS Photonics, in press, DOI: https://doi.org/10.1021/acsphotonics.0c01064 (2020) (**Chapter 4**). AB performed sample fabrication, experiments, analysis and calculations. TAW assisted in polarimetry calibration. All authors contributed to the writing.

4. R. Kolkowski, S. D. C. Roscam Abbing, A. Berkhout, C. D. Dieleman and A. F. Koenderink, *A comparison of TPEL and SHG for mapping the dynamics of local fields using interferometric autocorrelation*, in preparation (**Chapter 5**). AB designed the initial setup. AB and SDCRA built the setup and performed preliminary SHG measurements. RK significantly improved the setup detection schemes for SHG and proposed and tested TPEL. AB and RK designed the samples that AB fabricated. AFK supervised the project.

Other

1. B. Sciacca, A. Berkhout, B. J. M. Brenny, S. Z. Oener, M. A. van Huis, A. Polman and E. C. Garnett, *Monocrystalline Nanopatterns Made by Nanocube Assembly and Epitaxy*, Advanced Materials **29**, 1701064 (2017).

2. E. Marino, A. Sciortino, A. Berkhout, K. E. MacArthur, M. Heggen, T. Gregorkiewicz, T. E. Kodger, A. Capretti, C. B. Murray, A. F. Koenderink, F. Messina, and P. Schall, *Simultaneous Photonic and Excitonic Coupling in Spherical Quantum Dot Supercrystals*, ACS Nano, in press, DOI: https://doi.org/10.1021/acsnano.0c06188 (2020).

Patents

1. *Method for manufacturing a patterned monocrystalline film*, A. Berkhout, E. C. Garnett and B. Sciacca, patent number NL2016849.

Summary

Planar hybrid plasmonic-photonic resonators: an interferometric investigation

Light is a spectacular phenomenon that never ceases to amaze. Its most prominent aspect is the possibility to image the world onto our retina, whether we look at a single bacterium or a distant star. Light also plays a leading role as our indirect source for food, as it can be converted into the chemical compounds that fuel biochemical processes via the chlorofyl in green plants. While these key features have helped humanity survive over millions of years, over the last couple of centuries we have additionally come to implement light more and more as a technological tool. We store the sun's energy in batteries after photovoltaic conversion using solar cells, thus implementing light as an important sustainable source for our increasing electricity needs. Using advanced imaging and spectroscopy methods we have come to understand a major part of the world around us.

With the scientific advances of nanolithography fabrication techniques and electron beam microscopy the realization of ever smaller architectures, far beyond that visible by eye, came within reach, opening the field of nanotechnology. This evidently opened a whole new world of exciting possibilities to discover for light as well, giving birth to the field of nanophotonics. Crucial to nanophotonics is that the nanoscale is commensurate with the wavelength of light, meaning that geometrical optics no longer applies. An important topic of study in this field is to enhance the coupling strength between light and single emitters such as atoms or molecules. A particularly relevant goal in this field is to be able to catch, store, and release light at will, at precisely defined positions in space and moments in time. As an ultimate achievement, one could envision steering optical signals across a chip via opto-optical modulations, with a few or even single photons, allowing all-optical information and communication technology.

An important concept in nanophotonics that underlies the undertaking of mentioned endeavors is the principle of confinement applied to light. As we review in chapter 1, this is generally achieved using dielectric optical cavities, plasmonic metal nanoparticles or hybrid combinations thereof. Optical cavities are micron sized objects that capture light on the basis of refractive index differences and interference effects, whereas nano scale plasmonic scatterers take an entirely different approach which is to squeeze light in sub wavelength volumes via collective oscillations of free electrons in the metal, excited by light. While plasmonics offers especially high local field confinement, yet suffers from radiative losses, the opposite holds for optical cavities which reach poor local confinement but excel in the quality factors they offer. The combination of these two, so-called hybrid plasmonic-photonic systems, can

be particularly suited to overcome the mutual drawbacks and increase the interaction between light and matter.

In this thesis we investigate planar hybrid plasmonic-photonic cavities. The basic design essentially is that of a Fabry-Pérot or multilayer cavity that confines light between tflective surfaces, integrated with plasmonic layers of scattering metal nanoparticles. This is an ideal model system to understand the basis physics of hybrid plasmonic-photonic resonator: On the one hand this family of systems is easy to model, giving acces to both far-field input-output relations and prospective near-field enhancements. On the other hand the fabrication of such multi layer system is straightforward, and far-field measurements to probe complex reflection and transmission spectra are readily obtained. These cavities can be extended by integrating more layers including excitonic materials in theory as well as in practice.

In chapter 2 we first introduce a transfer-matrix based model that applies to stacks of dielectric and metallic layers combined with sheets of resonant plasmonic scatterers, arranged in arbitrary order. This model takes just properties of bare constituent layers as input, and returns complex reflection, and transmission coefficients, as well as locally induced plasmon antenna dipole moments. We treat three specific cases in detail, two of which are also experimentally studied in this thesis. The first is a Fabry-Pérot etalon in which one of the mirrors is replaced by a resonant layer of scatterers, similar to Salisbury screens in which a thin layer at a quarter wavelength from a mirror shows perfect absorption. We retrieve the expected points of zero reflection, and additionally illustrate how our model yields unexpected features in phase and polarization of such systems. The second case is a traditional Fabry-Pérot etalon, this time *filled* with a layer of scatterers. We find the expected signatures of strong coupling and make a comparison between these, and the signatures obtained for etalon which, in stead of with a scattering sheet, is completely filled with a dispersive dielectric material. Finally we address plasmonic-etalon designs that are hybridized with excitonic material.

The third chapter presents an experimental realization of the first case studied theoretically in chapter 2, the design of a plasmonic scattering sheet facing a metal mirror. We fabricated Au plasmonic nanorods of several pitches to vary scattering strength, which were covered in glass layer of increasing thickness in order to control etalon thickness, and finished with a Au mirror. To fully capture the metasurface etalon reponse we collected reflection spectra both in amplitude and phase. To this end we build a common path interferometry setup based on pulse laser illumination. By implementing a reference arm using birefringent crystals, we convert the initial laser pulse into a sample and reference pulse that are, after interaction with the sample, correlated in a Michelson interferometer to extract referenced reflection spectra. At certain combinations of frequency and etalon thickness we find that reflection vanishes in amplitude, a notion that is supported by phase maps that show singular points at precisely these locations. We elaborate on the origin of these

topologically remarkable points, and furthermore discuss the origin of some experimental deviations from the calculated predictions. A possible application of the investigated Salisbury plasmonic screen lies in reflective metasurface pixels, as between each pair of singular points in frequency-cavity-opening space the full 2π phase response is covered, accompanied by nonzero reflection.

Chapter 4 continues with an experimental extension to the study treated in chapter 3 by adding to the previous structure a thickness of glass equivalent to the first layer, accompanied by a closing mirror. This effectively yields a variable size Fabry-Pérot etalon with an antenna layer of various scattering strength placed exactly in the middle. The strong coupling features predicted in earlier works and calculated in chapter 2 of this thesis were retrieved using broad band transmission spectra in a simple white light transmision setup equipped with polarimetry, but not interferometry as in chapter 2. We extract the magnitude of the anti crossing and find a surprising scaling of the anti crossing strength with antenna polarizability. In addition we fully map the polarization state of the transmitted light, which reveals strong polarization conversion effects at strong coupling conditions. Because our experimental system is based on anisotropic plasmonic nanorods, the strong coupling physics results in very strong linear birefringence and linear dichroism.

To study coupling between light and matter we implemented in the first chapters planar cavities and sub wavelength plasmonic scatterers for light confinement. The local enhancement as a function of position in these, and plasmonic designs can not be probed using far field methods. In the final chapter we illustrate a setup that allows to measure nonlinear interferometric autocorrelation traces from nano scale nonlinear emitters in the focus of an objective. We first review the mathematics that is at the basis of the retrieval of temporal dynamics from such measurements, and subsequently illustrate experimental hurdles that are important to keep in mind. To conclude we show preliminary results on two-photon excited luminescence collected from quantum dots in the hotspots of silver nanoparticles. The presented work serves as a starting point for the investigation of more complex nano systems.

Samenvatting

Platte hybride plasmonische-fotonische resonatoren: een interferometrisch onderzoek

Licht is een spectaculair verschijnsel dat ons altijd zal blijven verbazen. Één van de meest aansprekende kenmerken van licht is dat het de wereld om ons heen kan afbeelden op ons netvlies, of we nu naar een enkele bacterie kijken of naar een ster diep verstopt in het heelal. Licht speelt tevens een belangrijke rol als indirecte bron voor ons voedsel, aangezien het via fotosynthese wordt omgezet in suiker — en daarmee de brandstof tot leven — in de bladgroenkorrels in planten. Op deze manier kan de mensheid al miljoenen jaren overleven. De laatste eeuwen is licht bovendien een steeds grotere rol gaan spelen in allerei technologische ontwikkelingen. Zo kunnen we de energie van de zon met behulp van zonnecellen opslaan in batterijen, als duurzame bron voor onze toenemende energiebehoefte. Met behulp van geavanceerde microscopen en spectroscopie methoden verkrijgen we steeds dieper inzicht in de wereld om ons heen.

Met wetenschappelijke ontwikkelingen zoals nanolithografie en elektronenmicroscopie werd het mogelijk om steeds kleinere structuren te maken, die met het blote oog zelfs niet meer zichtbaar zijn: de nanotechnologie was geboren. Deze nieuwe onderzoeksrichting bracht fascinerende perspectieven voor licht met zich mee. Nanofotonica bestudeert immers processen op lengteschalen die overeenkomen met de golflengte van licht, een schaal waarop wetten uit de geometrische optica niet langer gelden. Een belangrijk onderzoeksveld binnen de nanofotonica betreft de koppeling tussen licht en materie, en hoe die versterkt kan worden. Specifieker streven onderzoekers ernaar om licht in een enkel atoom of molecuul op te kunnen slaan. Het doel daarbij is om licht te kunnen vangen, op te slaan en weer los te laten met volledige controle over zowel de opslaglocatie als de tijdsduur. De ultieme droom is om optische signalen volledig licht gestuurd door alle schakelingen in een optische chip te kunnen sturen. Daar zijn nu nog elektronische signalen voor nodig. Als dit met heel weinig licht of met zelfs maar enkele fotonen lukt komen volledig optische informatie en communicatie technologie binnen bereik.

Een belangrijk concept voor de uitvoer van bovenstaande toepassingen is het principe om licht te kunnen vangen. Zoals in hoofdstuk 1 aan bod komt gebruikt men voor het opsluiten van licht in het algemeen diëlektrische optische trilholtes, plasmonische metalen nanodeeltjes of een hybride combinatie daarvan. Optische trilholtes zijn micrometers in grootte en vangen licht op basis van brekingsindex verschillen tussen materialen en interferentie effecten. Nanoschaal plasmonische verstrooiers werken daarentegen heel anders: zij concentreren licht in sub nanometer volumes via collectieve oscillaties van elektronen in het metaal, aangeslagen door licht. Waar plasmonische

nanodeeltjes zorgen voor hoge lokale veldversterking, echter gehinderd door stralingsverliezen, geldt het tegenovergestelde voor optische trilholtes, die licht niet sterk lokaal concentreren maar wel enorme 'kwaliteitsfactor' hebben — een maat voor het aantal weerkaatsingen van licht in een trilholte. De combinatie van deze twee structuren, zogeheten hybride plasmonische-fotonische systemen, zijn erg geschikt om de nadelen van beide componenten tegen te gaan en de interactie tussen licht en materie te versterken.

In dit proefschrift onderzoeken we dunne hybride plasmonische-fotonische trilholtes. Het basis ontwerp is een Fabry-Pérot of multilaags trilholte waarin licht rondzingt tussen reflecterende oppervlakken, met plasmonische lagen van verstrooiende metalen nanodeeltjes daarin geïntegreerd. Dit is een ideaal model systeem om de eenvoudige natuurkunde van hybride plasmonische-fotonische systemen te begrijpen. Aan de ene kant zijn deze systemen simpel te modelleren, zodat verre-veld input en output verbanden gelegd kunnen worden en men ook de voorziene nabije veld versterking kan peilen. Aan de andere kant is de fabricage van dit soort meerlaags systemen ongecompliceerd, en de verre-veld complexe reflectie en transmissie is makkelijk te meten. Een bijkomend voordeel is dat dit soort trilholtes zowel in theorie als in de praktijk uitgebreid kunnen worden door extra lagen toe te voegen, zoals bijvoorbeeld excitonische materialen.

In hoofdstuk 2 introduceren we eerst een transfer-matrix gebaseerd model dat een stapel diëlektrische en metalen lagen beschrijft, gecombineerd met lagen resonante plasmonische verstrooiers. De optische eigenschappen van de losse onderdelen vormen de input voor dit model, en de output bestaat uit complexe transmissie en reflectie coëfficiënten en lokaal geïnduceerde dipoolmomenten in de plasmonische antennes. We behandelen drie specifieke gevallen in meer detail, waarvan we twee ook experimenteel onderzoeken in dit proefschrift. Het eerste geval is een Fabry-Pérot etalon waarin we één van de spiegels vervangen door een laag resonante verstrooiers, vergelijkbaar met Salisbury schermen waarin in een dunne laag, op een kwart golflengte afstand van een spiegel, perfecte absorptie behaald kan worden. We vinden de verwachte nul-reflectie-punten en illustreren daarnaast hoe ons model onverwachte fase en polarizatie eigenschappen in dit soort systemen laat zien. Het tweede geval is een traditionele Fabry-Pérot etalon met *daarin* een laag resonante verstrooiers. We berekenen de verwachte tekenen van sterke koppeling en vergelijken dit geval met een etalon ontwerp dat, in plaats van gevuld met een dunne verstrooiende laag, compleet gevuld is met dispersief materiaal. Tot slot behandelen we plasmonische etalon ontwerpen gehybridiseerd met excitonisch materiaal.

In het derde hoofdstuk beschrijven we experimenteel het eerste theoretische geval uit hoofdstuk 2, te weten de laag resonante verstrooiers vóór een spiegel. Om verstrooiingssterkte te varieren fabriceerden we gouden plasmonische nanorods in een roosterstructuur, waarbij we de roosterconstante varieerden. Deze antennes bedekten we met een dunne laag glas van toene-

mende dikte om de etalon grootte te variëren. Als laatste laag voegen we een gouden spiegel toe. Om het gedrag van dit metaoppervlak etalon volledig te beschrijven maten we reflectie spectra in zowel amplitude als fase. Voor deze metingen hebben we een 'common path' interferometrische opstelling gebouwd — waarin alle bundels via precies dezelfde optische elementen de opstelling doorlopen — gebaseerd op gepulste laser beliching. Door een referentie arm in te bouwen met behulp van dubbelbrekende kristallen kunnen we de oorspronkelijke laser puls omzetten in een sample en referentie puls die, na interactie met het sample, in een Michelson interferometer met elkaar gecorreleerd worden om geijkte referentiespectra te achterhalen. Bij bepaalde combinaties van licht frequentie en etalon dikte verdwijnt de reflectie volledig in amplitude, bevestigd door fase plots die op exact dezelfde punten singuliere punten laten zien, waarin de fase niet gedefinieerd is. We behandelen de oorsprong van deze topologisch opmerkelijke punten, en bespreken daarnaast enkele experimentele afwijkingen van de berekende voorspellingen. Mogelijke toepassingen voor deze Salisbury plasmonische schermen zijn reflecterende metaoppervlak pixels, omdat tussen elk paar singuliere punten in frequentie-etalondikte-ruimte de volledige 2π fase respons te vinden is, met daarbij een reflectie amplitude ongelijk aan nul.

Hoofdstuk 4 bouwt voort op het vorige hoofdstuk met een experimentele uitbreiding: aan het vorige ontwerp voegden we een extra laag glas van dezelfde dikte toe, alsmede een tweede gouden spiegel, zodat we een Fabry-Pérot etalon van variabele dikte verkrijgen met exact in het midden een laag antennes die varieert in verstrooiingssterkte. De tekenen van sterke koppeling die eerder werk en onze berekeningen in hoofdstuk 2 voorspelden, zien we terug in breedbandige transmissiespectra in een simpele wit licht transmissie opstelling. Deze opstelling meet ook polarimetrische responsen, maar geen interferometrie zoals in hoofdstuk 2. We bepalen de grootte van de afbuigende resonantielijnen en vinden een verrassend verband tussen deze zogeheten anti-kruising en de antenne polarizeerbaarheid. Bovendien brengen we de volledige polarizatie toestand van het doorgelaten licht in kaart, dat bij condities van sterke koppeling een grote polarizatie conversie laat zien. Omdat ons experiment gebaseerd is op de implementatie van niet-isotrope plasmonische nanoantennes vertoont deze natuurkunde tekenen van zeer sterke dubbelbrekendheid en linear dichroisme.

Om de koppeling tussen licht en materie te bestuderen implementeerden we in de eerste hoofdstukken dunne, platte trilholtes en sub golflengte plasmonische verstrooiers om licht op te sluiten. De lokale veldversterking als functie van positie in deze ontwerpen kan niet getoetst worden met verre-veld technieken. In het laatste hoofdstuk schetsen we daarom een opstelling waarmee niet lineaire interferometrische autocorrelaties gemeten kunnen worden, van nano schaal emitters in het focus van een objectief. We beschrijven eerst de wiskunde die ten grondslag ligt aan het achterhalen van tijdsafhankelijke dynamica uit zulke metingen, en laten daarna de experimentele obstakels zien

waar men rekening mee dient te houden. Tot slot laten we eerste resultaten zien van twee-foton luminescentie van quantum dots dicht bij zilveren nanodeeltjes waar het lokale veld zeer hoog is. Deze resultaten vormen een begin voor het onderzoeken van complexere nano systemen.

Acknowledgements

Having arrived at writing this page I realize that what people always write is absolutely true: this thesis would not be in your hands if it were not for all the people that have supported me along the way. Be it with challenges in the lab, finetuning cleanroom recipes or welcome distractions in the form of coffee, after work dinners, drinks and parties; it really is the people, *you*, that have made the last five years of my life so enjoyable.

Everybody contributed to this journey in a different way. Femius, I am very happy for the adventure we have been on together. In the beginning I was intrigued by your occasional invite to a staring contest – or so it seemed – and I was a bit puzzled as to how to interpret your facial expressions. Luckily during one of our group meetings you clarified that there is no hidden meaning, it's just facial gymnastics. I have really come to like your style and sense of humor, and will definitely miss it. Your knowledge of physics and mathematics is very impressive, and I am grateful to have learned so much from you. I admire the sincere approach you take not only on research, but also on life. Also the commitment that you have for your group I find amazing. I know you got significantly busier over the last years, but somehow you always made time to talk to me. Whenever I came into your office, other activities would be parked until we sorted out this one mathematical hurdle or some other problem. With many group members close to finishing, I am very curious to see where the group will be in another five years. We should definitely have an occasional cake or beer, to keep me updated!

Said, thank you for being my co promotor, your assistance in preparing this manuscript, and your eternal drive for physics. Our shared group meetings were very enjoyable.

To an outsider it may look like a researcher at AMOLF spends some time behind the desk to model a physical principle, then fabricates a sample, carries out an experiment and publishes an article. What is actually in between all these steps is an enormous deal of support. It is always mentioned, and is indeed truly exceptional. It already starts by arriving in a nicely clean and fragranced office every day. Tineke en team, bedankt! Ik kan elke ochtend het gebouw instappen en fris aan een nieuwe dag beginnen. A big part of this thesis involved the fabrication of many millions of 'nano antennas', which would never have turned out so well without the cleanroom assistance. On top of the great advice you guys have always supplied me with, you do this with a lot of patience and jokes. Working in the cleanroom has always (ok, provided that things worked out) been relaxed and fun. Dimitry, at some point I must have called you at least three times a day, and I never got the feeling that this was too much. Bob, thanks for our talks about food and the new recipes that you have been trying. Hans, thank you for your cheerfulness, your nice greetings on the stairways in the building, and for your stories on

photons in the bathroom at night. I am also happy with the support of all the other departments, from reception and canteen to facilities, the workshop, ICT, the library and of course Ilja and the safety department!

The major part of the play that is my PhD was staged at office 1.09. My dearest office mates, at times when the fabrication, experiments and the PhD in general have been troublesome and annoying (they have), returning to you in our office decorated with paper pineapples, birthday flags and other random stuff was all I needed. At such occasions we often ended up with a lot of paper balls (and other objects) flying through the room, and I could relax and put everything in perspective. Ruslan, thank you for your support while walking through our PhDs together, for being an infinite source of technology news, and for our runnning sessions in the Vondelpark (with you running twice slower than usual such that I could keep up). I know I can always count on you. Christiaan, thanks for the many many supportive notes that you wrote to me and the nice times we spend together. I was very sad to see you leave, and have really missed you in the office. The silence you left must have made me more productive, but it was definitely less fun. You will understand that, being the only contestant left, Ruslan has now won the best office mate competition (his prize: dinner with the three of us!).

Kévin, I love your French style: your humor as well as the occasional stubbornness. Going to New York this month is perhaps a weird start of your postdoc, but I am sure it's going to be a nice experience! Isabelle, thanks for your energy and enthusiasm, and for increasing my knowledge of out of fashion (perhaps even useless), but fantastic English words intertwined in all your stories. Hugo, I was always impressed by your ability to be great at almost everything, and on top of that be the most stylish guy in the building. Marko, I probably learned most of my optical table skills from you, thanks for helping me in the lab so much in the beginning. The only thing I regret is that I have still not seen you play in your band. Radek, thank you for being a tremendous help in the lab, carrying out many experiments and teaching me all about nonlinearities. Discussions on physics with you were so nice. Good luck with the next step in your life, and I hope that, next to being challenging enough, it will also be a place that is a bit relaxed! Sylvianne, thanks for laying the foundation for our nonlinear setup. I guess second order nonlinear was too easy for you, since you moved on to higher harmonics next door. Tom, when will we have cake again? I am very grateful for all the seemingly straightforward but super tricky polarimetry tricks you taught me. Please continue to eat exactly two apples each day. Deba, we only spend a few months in an office together, but we have had deep conversations on big life choices already. Thanks for that, and I hope you will enjoy your time in the group! Beniamino, I much enjoyed our Dutch conversations during drinks. Also the music gigs you did with Charlie were really cool. I love your view on life, and am really curious to see what the future brings for you! Tomas, having coffee with you was always very gezellig. I also have great memories

on our 24 hour sailing match, shall we do that again next year? Ilan, thanks for our nice chats, and cake and coffee breaks!

Luckily AMOLF is small enough to interact with basically everyone in between all the work. Lukas, I am so excited that we are each others paranimph, and we get to experience the finishing of the thesis in this weird time together. Thanks for all the adventures we have been on. I cannot wait to properly celebrate our PhD, and life in general again, with you. Moritz, thanks for the delicious Korean dinner, and for being great company on our trips together with Lukas. Giulia, my not-so-Dutchie. We started our masters and then PhDs together, and will both make it to the finish this autumn, with the help of many pizzas and aperitivos along the way. Let's continue to do that for a looong time, and hopefully I even get to see your valley once! Floortje, being in the PV was really nice, and a big part of that is since you were in it. Let's meet up with Giulz quickly! Verena, thank you for all the nice talks we had, we should find a way to do this more. Sophie, thank you for the pizza dinners, and the dancing afterwards. Nick, we do not even meet that often, but when we do we connect really well. Benjamin B., you have always been so kind and involved. Conversations with you are always fun, and seeing you dance is just fantastic. Giada, thank you for the openness you radiate, and for introducing me to your magnificent friends. Marloes, thanks for joining me on our walking to the beach adventure. Harshal, I want to thank you for having simply the best laugh in AMOLF. And for your one nanocube that ended up in the last chapter. Let's discuss future plans over a dinner soon. And... so many other memories pop up in my head. Thanks for being a great dj (Cesare), for relationship advice (Sven), for quantum dots (Christian), for showing me how to climb the library (Jente), for being a great silent disco dancer (Mathijs), for sharing an office all the way in the beginning (Parisa), and Leonie, Jenny, Giorgio, Hans, Niels, Andrea, Tom, Benjamin D., Nasim, Teresa, Robin, Roel, Rene, Jesse, thanks for even more coffee, discussions and jokes.

Towards the end of my PhD I took an expedition to the world outside academia and participated in a Thinktank for a few months. DenkTank de musical gespeeld, slide decks met action titles gebouwd en alles in impact-effort matrices geprobeerd te proppen, dat laatste met gematigd succes. DenkTankers, bedankt voor al jullie fantastische quotes, dure-consultant-taalgebruik, Engelse woorden op niks af, en voor alle feestjes, weekenden weg en vakantie naar Zwitserland. Vera, ik weet nog exact hoe wij elkaar voor het eerst ontmoetten, en hoe gezellig dat was. Ookal heb je daarna alleen maar over ongelijke machtsverhoudingen gepraat, we zijn uiteindelijk toch vrienden geworden. Martijn, niemand krijgt mij zo in de slappe lach als jij. Ik hoop stiekem dat je helemaal niet naar Zwitserland verhuist. Plym, als er even geen hout in de buurt was en je dus geen kast aan het bouwen was gingen wij op pad. Zo fijn dat ik tegen je aan mocht praten tijdens het hardlopen (want dan kon je zelf even niet praten), wielrennen en zonnen op jouw balkon. Bruno, een verfrissing om ook jou te hebben leren kennen. Laten we heel snel weer

op stap gaan. Falko, ik dacht dat jij keurig was, maar dat is gelukkig niet zo. Fuuk, ik geniet van jouw algehele expressie, en, aandacht voor interpunctie. Sem, één woord: soepel. Féline, bedankt voor het samen de berggeit uithangen. Wouter, wat zijn wij verschillend, en vormen we daarom een goed team! Lofty, van jouw hang naar structuur zou ik nog een hoop kunnen leren. Maar laten we eerst (als het weer mag), ons verkleden en weer naar de disco gaan. Mees, ik hoor je nóg mijn naam door de gang schreeuwen, elke keer als ik langs liep. Ottalie, schandalig hoe dicht wij bij elkaar wonen, en hoe weinig wij elkaar zien!

Lieve Lotte, wat hebben wij al een hoop beleefd en gelachen samen. Super vertrouwd, ik kan alleen maar hopen dat we dat de rest van ons leven zullen blijven doen! Charlotte, so nice to know you too. We should definitely bake those croissants from scratch soon. Marjon en Annemarie laten we alstjeblieft snel nóg meer van het leven genieten, inclusief fristi, poffertjes, aperol spitz, yoga en wielrennen (in willekeurige volgorde). Bedankt voor de eerlijke gesprekken over zo ongeveer alles in het leven, jullie goede vragen en ideeën en gezellige vakanties (als het tenminste niet zo waait) ook met Lotte. Joost, bedankt voor al jouw goede en slechte grappen, je illustratie en de geniale filmavonden bij jou en Marjon thuis. Anneloes, zo leuk dat wij elkaar steeds meer zijn gaan zien over de jaren. Je bent zo lief en open en zonder voordelen, ik ben heel blij dat wij vriendinnen zijn. Daan, wat een genot om na al dat wetenschappelijke gedraaf gewoon even simpel bier met jou te drinken, oude hits op lp's te luisteren en veel pizza te eten. Laura, bij jou in Den Haag voelt het altijd alsof ik op vakantie ben. Ik hoop op nog oneindig veel logeerpartijtjes met jou en Deru, zwemmen in de zee, dansen op het strand, Roald Dahl voorgelezen krijgen in bed, en natuurlijk op meer friet. En Deru wat ben ik blij met jouw verfrissende kijk op de wereld, en hoe we - infrequent maar toch steeds weer opnieuw - samen door de bossen stappen en zo even alles kunnen relativeren.

Tot slot ben ik heel gelukkig met alle ondersteuning van mijn familie. Mama, papa, en broers, bedankt voor jullie betrokkenheid, liefde, en het vertrouwen in mij als ik het misschien even niet meer zo goed wist. Jullie nuchterheid en relativeringsvermogen kon ik goed gebruiken, en ik ben er trots op dat we zo'n hecht team zijn.

About the author

Annemarie attended the Murmellius Gymnasium in Alkmaar. After briefly exploring the fields of chemistry, medicine, and economics, she obtained her bachelor degree Bèta-gamma, an interdisciplinary study with a major in Physics, in 2012. This was the time she first set foot into AMOLF, where she performed her graduation research in the biochemical networks group under the supervision of prof. dr. Pieter Rein ten Wolde. She subsequently took a one year break from studying, in which she enjoyed several jobs, and lived in France for a while to learn the language, eat cheese and three course lunches every day, and talk about food. Refreshed and looking forward to studying again, she continued with a master in Phyics at the UvA, during which she researched silver nanocubes patterning in the nanoscale solar cells group, supervised by prof. dr. Erik Garnett. Annemarie graduated *cum laude* in 2015 and received the biennial Pieter Zeeman prize for her thesis. Since she was grasped by light during a master course in nanophotonics, she started her PhD in the resonant nanophotonics group of prof. dr. Femius Koenderink in 2016. Close to the end of her PhD she took a detour from physics for four months and participated in the Dutch National ThinkTank, the topic of that year being digitalization. Currently, Annemarie spends one day a week on the foundation that she founded with two other participants. When not behind a desk, in a lab or in the kitchen, Annemarie likes to do yoga, go running, or eat, drink and dance with her family and friends.